CRITICAL DESIGN PARAMETERS FOR PYLON-AIDED GASEUOUS FUEL INJECTION UPSTREAM OF A FLAMEHOLDING CAVITY

THESIS

Mitchell R. Pohlman, Captain, USAF

AFIT/GAE/ENY/09-M15

DEPARTMENT OF THE AIR FORCE
AIR UNIVERSITY
AIR FORCE INSTITUTE OF TECHNOLOGY

Wright-Patterson Air Force Base, Ohio

The views expressed in this Graduate Research Project are those of the author and do not reflect the official policy or position of the United States Air Force, Department of Defense, or the U.S. Government.

AFIT/GAE/ENY/09-M15

CRITICAL DESIGN PARAMETERS FOR PYLON-AIDED GASEUOUS FUEL INJECTION UPSTREAM OF A FLAMEHOLDING CAVITY

THESIS

Presented to the Faculty

Department of Aeronautical Engineering

Graduate School of Engineering and Management

Air Force Institute of Technology

Air University

Air Education and Training Command

In Partial Fulfillment of the Requirements for the

Degree of Master of Science in Aeronautical Engineering

Mitchell R. Pohlman

Captain, USAF

March 2009

AFIT/GAE/ENY/09-M15

CRITICAL DESIGN PARAMETERS FOR PYLON-AIDED GASEUOUS FUEL INJECTION UPSTREAM OF A FLAMEHOLDING CAVITY

Mitchell R. Pohlman
Captain, USAF

Approved:

Greendyke, Robert B., Civ AFIT/ENY (Chairman) — Date: 17 Mar 09

King, Paul I., Civ AFIT/ENY (Member) — Date: 17 Mar 09

Huffman, Richard E., Maj AFIT/ENY, USAF (Member) — Date: 17 MAR 09

Abstract

The Air Force Institute of Technology and the Air Force Research Lab are investigating means to increase the efficiency of fuel-air mixing into supersonic flow. Previous work has shown much promise in increasing the penetration and mixing of a fuel-air mixture into the freestream by injecting fuel behind small triangular pylons. Pylon-aided fuel injection has also shown to lift the entire fuel plume off the combustor floor; this floor-gap prevents the ignition of fuel seeded in the boundary layer. In this paper twenty-one pylons of varying widths, heights, and lengths were examined in four specific test matrices within a CFD environment. Pylons in test matrix 1 maintained a constant height and length while varying the pylon width. Test matrix 2 and 3 varied the absolute height of two different pylons from test matrix 1; scaling the pylons absolute height and maintaining a constant leading edge wedge angle and width to height ratio. The final test matrix varied the length of pylons while keeping the height and width fixed. Pylons with a width less than 3-diameters featured a fuel plume flow structure dominated by two sets of counter-rotating vortices. These pylons displayed large amounts of penetration and floor gap with minimal impact on flammable fuel plume area (A_f). The 4,5, and 6-diameter wide pylons resulted in flow structures dominated by one large set of vortices with minimal penetration and large A_f values. Test matrices 2 and 3 depicted increased penetration and A_f as pylon height is increased. Variations in pylon length had no discernable impact on the fuel -air mixing metrics. Aerodynamic loses were minimal for all pylon configurations and did not correlate to the absolute size of the pylons tested.

Acknowledgements

I would like to express my sincere gratitude to my sponsor Dr. Dean Eckland from the Air Force Research Laboratory, Propulsion Directorate as well as to Dr. C.-J. John Tam, Dr. Mark Gruber, and Dr. Mark Hsu, also from AFRL/RZAS, for their help and guidance though this process. I am indebted to Dr. Robert A. Baurle of the Hypersonic Air Breathing Propulsion Branch at NASA for his help with the VULCAN code. The comradery and support of my fellow students in the Linux Lab including Matt Bagg, Brook Bentley, Katie Sullivan, Spencer Bowen and Neil Rogers was critical to not only the successful completion of this research but my sanity as well. The care, support, and motivation provided to me by Dr. Robert Greendyke brought out the best in me, and hopefully was translated into my research and this document. Without the support from all of these individuals this work would not have been possible.

Mitch R. Pohlman

Table of Contents

List of Figures

Page

Page

Page

Page

Page

Page

Page

List of Tables

Page

List of Symbols

Symbol	
A_f	flammable fuel plume area (in^2)
A_i	fuel injector port area (in^2)
A_p	total fuel plume area (in^2)
d	fuel injector port diameter (in^2)
D	flame-holding cavity depth (in)
FPP	flammable plume percentage
h	pylon height (in)
h_c	penetration of plume core (in)
h_p	total fuel plume penetration (in)
l	pylon length (in)
L	flame-holding cavity length (in)
M	Mach number
P_t	total pressure (kPa)
$\bar{q}$	jet-to-freestream momentum flux ratio
u	freestream velocity (m/s)
w	pylon width (in)
x_{fmd}	flammable mixture distance (in)
X_P	injection proximity (in)
Φ	equivalence ratio
Φ_l	lower flammability limit
Φ_{max}	maximum equivalence ratio

Φ_u	upper flammability limit
ρ	density (kg/m^3)
ω	total pressure loss coefficient

CRITICAL DESIGN PARAMETERS FOR PYLON-AIDED GASEOU FUEL INJECTION UPSTREAM OF A FLAMEHOLDING CAVITY

1. Introduction

1.1 Motivation

There has been much recent interest by the Department of Defense to develop the ability to rapidly engage high-value, time-sensitive targets anywhere in the world. The ability to prosecute these targets without the need for a large forward military presence in a matter of hours instead of days is was a key finding of the 2006 Quadrennial Defense Review. Several of the alternatives being considered in the Prompt Global Strike (PGS) program include; conventionally armed ballistic missiles, a maneuverable reentry vehicle carrying a variety of payloads launched from the Continental United States, and hypersonic bombers and cruise missiles. Though the conventionally armed ballistic missile may be the least technically challenging alternative for the Prompt Global Strike Program, political and operational challenges have limited the attractiveness of this option. The development of a hypersonic bomber is very complex, costly and time consuming undertaking that eliminates this option as a near term solution to Prompt Global Strike. The hypersonic cruise missile presents a relatively inexpensive alternative that while complex is much more feasible to achieve in the near term. The hypersonic bomber and hypersonic cruise missiles alternatives for the PGS program provide the driving force for continued research into the development of propulsions systems for these high speed systems.

The supersonic combustion ramjet (scramjet) engine is an attractive propulsion system for air vehicles in flight regimes above Mach 6. Unlike a conventional ramjet engine where the incoming supersonic air is slowed to subsonic speeds for combustion, the scramjet engine operates supersonically throughout. Though aerodynamically complex the scramjet engine is relatively simple, consisting of an inlet, isolator, combustion chamber, and nozzle with few moving parts.

Critical to the design and development of hypersonic air-breathing propulsion systems, such as scramjet engines, is efficient fuel injection and mixing. The supersonic velocities found within scramjet engines mean there is minimal time available to properly inject the fuel with the free-stream and then to bring the fuel-air mixture to the proper concentration to support combustion. Increased efficiency in fuel-air mixing may lead to reductions in the size of the combustion chamber leading to reductions in size and weight of the engine as well as reducing the amount of structure that needs to be cooled, a major issue at hypersonic speeds. Though many different strategies have been developed over the years to effectively mix the fuel with the freestream, the aim and metrics of these various techniques are the same. Key metrics for such a mixing strategy include maximizing the penetration of the fuel plume into the freestream, reaching the minimal requirements for combustion as quickly as possible, minimizing aerodynamic losses, and lifting the fuel-air mixture away from the wall and thus preventing the ignition of fuel seeded in boundary layer, a phenomena known as flashback.

1.2 Research Focus and Goals

Countries around the world currently have active research efforts underway, seeking ways to overcome the major technical hurdles associated with creating an operational scramjet powered hypersonic aircraft. One current research thrust at the Air Force Research Laboratory Propulsion Directorate (AFRL/RZ), in conjunction with the Air Force Institute of Technology, seeks to improve supersonic combustion through the use of small triangular pylons placed upstream of normal fuel injection ports. The wake behind the pylons creates a low momentum region and flow structure that increases both the penetration and mixing of the fuel-air mixture with the freestream with minimal aerodynamic losses. Larger more intrusive fuel-air mixing strategies are limited, to an extent, by the losses and thermal loading associated by their increased surface area.

Experimental work done by Haubelt et al.[1] investigated the performance of three different sized triangular shaped pylons within the Supersonic Combustion Facility of AFRL/RZ. The size and shape of the three pylons tested in his work were guided by the results of numerical simulations[2] on the relative effectiveness of different pylon geometries to pre-mix fuel within the inlet, prior to combustion, in a scramjet engine. These numerical simulations focused not only on the basic geometry of the triangular pylons but the proximity of these pylons to the fuel injector port as well. The numerical studies[2] and experimental work[1, 3, 4, 5] into pylon-aided fuel injection have investigated only a limited number of variations in the pylon's width and height with no variation in the pylon's length or leading edge wedge angle.

The goal of this work is to perform a parametric study on the physical geometry of the pylons used in pylon-aided normal fuel injection in the hopes of identifying trends in the fuel-air mixing metrics associated with varying individual aspects of the pylon's geometry. This work presents numerical simulations of pylon-aided ethylene fuel injection behind small triangular shaped pylons of varying geometries. The focus of this study is purely on the geometry of the pylon, keeping the fuel injection properties and pylon to injector-port proximity constant throughout all simulations. The large number and wide range of geometries tested in this study will aid in correlating specific fuel plume structures and thus mixing performance to specific pylon geometries. With a large database of pylon geometries, this work can provide an initial 'tool-box' to aid designers in choosing various pylon geometries to optimize various fuel-air mixing metrics, whether it be minimizing pressure loss, maximizing flammable fuel plume area or maximizing penetration into the freestream.

2. Literature Review

2.1 Fundamentals of Scramjet Engines

In the ongoing pursuit of hypersonic flight one of the fundamental hurdles is the design and development of adequate propulsions systems. Structural limits in the turbine section in addition to propulsive efficiencies limit the maximum performance of typical turbojet engines to flight speeds around Mach 3.5. Ramjet engines seek to bypass this limitation by operating without the rotating turbo-machinery associated with turbojets and are thus not limited by the failure point of turbine blades. A ramjet harnesses the ram pressure associated with slowing down the incoming air to provide compressed air for combustion. The flow is slowed and compressed by a series of oblique shock waves in the converging duct of the ramjet inlet until subsonic flow is reached downstream of a normal shock wave. Fuel is then injected to the subsonic airflow and combusted. This hot, high pressure flow is then accelerated to supersonic speeds and exhausted through a convergent-divergent nozzle. Figure 1 illustrates the basic concept of a ramjet engine[6].

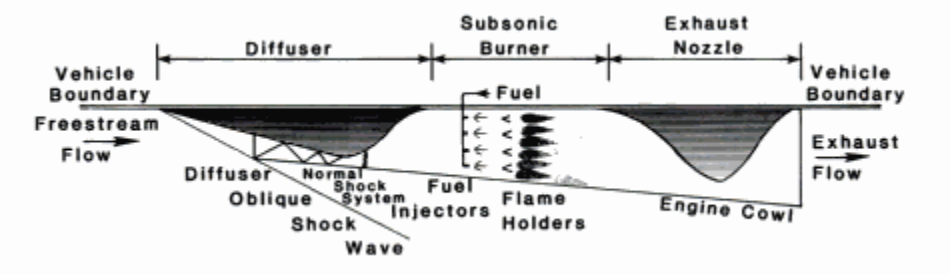

Figure 1. Schematic diagram of a ramjet engine[6].

One critical drawback to this form of propulsion is the inability to create static thrust. Ramjet engines must be boosted to their minimum operating speed by some other propulsive force, often rockets, before they can create thrust. As the flight speed is increased towards Mach 6 the pressure and temperature rise associated with bringing the incoming air to subsonic speeds approaches several critical limits; the increased pressure may overstress the structure, the breaching of wall temperature limits, and combustion conditions that lose a large amount of chemical energy to dissociation[6]. Additionally, the pressure losses due to the normal shock wave system become excessive. To push past the Mach 6 limit with an air-breathing engine a supersonic combustion ramjet engines is necessary. In scramjet engines the high temperature and pressure rise associated with decelerating the flow to subsonic speed is avoided by only partially decelerating and compressing the flow through a series of oblique shock waves allowing the air to enter the combustion chamber at supersonic speeds. As the fuel is injected and combusted the high temperature air expands and accelerates as it proceeds through the divergent nozzle.

Typical hypersonic scramjet powered aircraft feature a highly integrated engine-vehicle design where in the airframe plays a critical component in the performance of the scramjet engine. Figure 2 depicts the components of a propulsion-airframe integrated scramjet engine[7]. The fore-body of a hypersonic aircraft starts the propulsive process by creating a set of oblique shock waves that begin to decelerate and compress the airflow before it enters the engine inlet. Once air is captured by the inlet it enters the isolator where a series of oblique shock waves continue to decelerate and compress the air. The aircraft fore-body, inlet, and isolator form the compression system of the scramjet engine.

A properly designed isolator is capable of handling a wide range of flight Mach numbers and high back pressure, allowing the engine to operate in a 'started' mode[8]. The term 'started' infers that the flow within in the isolator does not alter the capture characteristics of the inlet. An engine 'unstart' can occur when the pressure rise due to combustion downstream of the isolator increases beyond the point that can be sustained by the isolator causing major disruptions in the capture and compression of the incoming air[9].

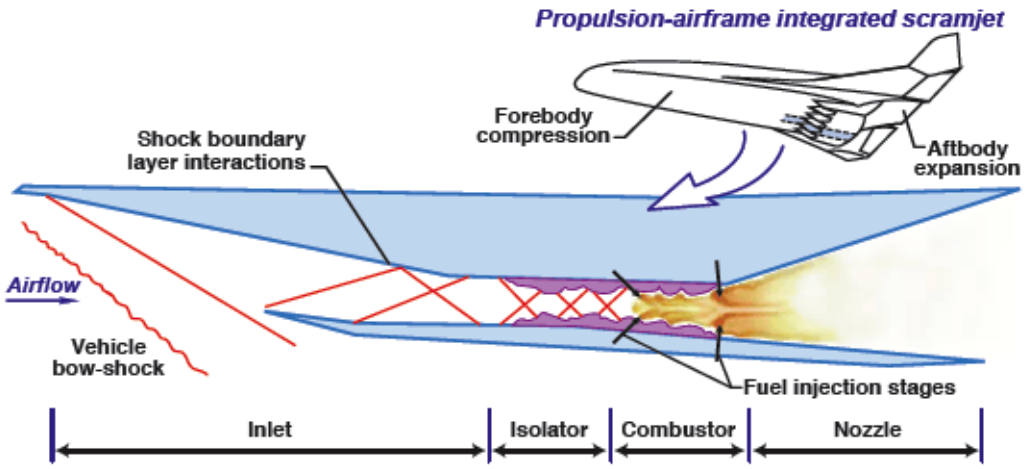

Figure 2. Components of an integrated hypersonic aircraft and scramjet engine[7].

Two of the most critical challenges associated with scramjet propulsion, proper fuel injection and stable combustion, occur with the combustor. The supersonic velocities within the scramjet engine provide an extremely short residence time: fuel must be injected, mixed and burned in on the order of 1 ms or less[9]. In order to increase the residence time recirculation zones can be used to ensure sufficient time for fuel ignition and combustion. A recessed cavity, as seen in Figure 3, creates a subsonic recirculation region that functions as a flame-holding cavity. Slant wall cavities, as seen below, have been shown to reduce the drag penalty associated with the use of flame-holding cavities.

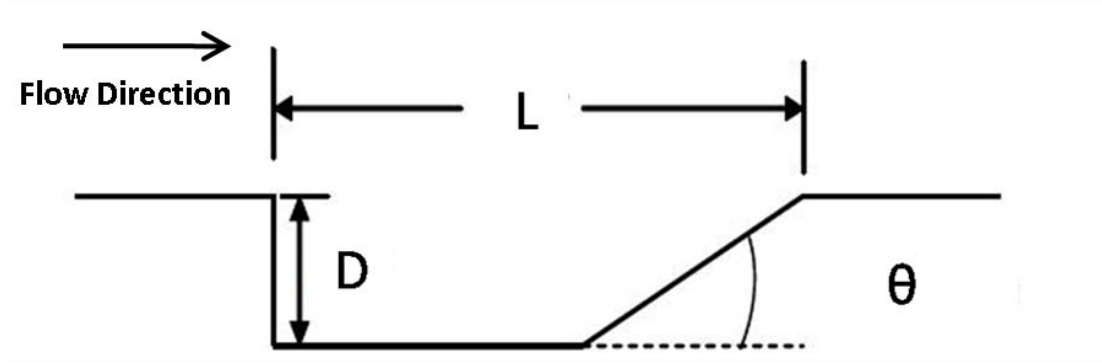

Figure 3. Slant wall cavity design.

Research performed by Quick et al.[10] at the Propulsion Sciences Branch of the Air Force Research Laboratory Propulsion Directorate has identified the ranges of length to depth ratio (L/D) and wall ramp angle (θ) for flame-holding cavities with acceptable performance.

The expansion system of a scramjet engine is composed of the internal nozzle and aft-body of the aircraft. The high temperature and pressure gas mixture resulting from the combustion process expands and accelerates through a divergent nozzle translating the potential energy from the combustion process to kinetic energy and thus creating positive thrust. The expansion and acceleration of the hot exhaust plume continues beyond the scramjet nozzle utilizing the aircraft aft-body as a free expansion surface[6].

2.2 Fuel Injection Strategies

The minimal fuel residence times within a scramjet engine place a premium on effective injection and mixing of the fuel with the freestream air. In choosing a fuel injection strategy designers must often trade off between mixing efficiency, thermal protection required for the injection process, penetration, and pressure losses. Studies by

Schetz[11] have illustrated that the degree of fuel plume penetration into the core flow is critical to the overall performance of a combustor. The minimal residence time requires a very short mixing length to achieve a fuel plume within combustion limits as quickly as possible. Without effective thermal management systems the extreme environment and temperatures found in the combustor would exceed the melting point of metallic structural materials[12]. The high energy release and short ignition time associated with hydrogen[8] makes it an attractive choice of fuel for scramjet engines. However hydrogen's low density and high volatility creates operational difficulties that have led engine designers to the use of hydrocarbon fuels instead of hydrogen. The higher ignition times associated with hydrocarbon fuels further compound the difficulty in supersonic fuel injection. The ultimate goal of a fuel mixing strategy is to create a fuel plume that has reached the minimal requirements for combustion as quickly as possible while minimizing the pressure losses and possible cooling requirements associated with that particular strategy.

Several mechanisms have been identified that aid in fuel mixing: increasing the streamwise vorticity, inducing of swirl to the injected fuel, interaction between fuel plume and shockwaves, and forced excitation of fuel plume on large scales. The forced excitation of fuel plumes includes active mixing mechanisms such as pulsed jets, splitter wires, wavy walls, and piezoelectric actuators[34]. Both active and passive strategies have been developed that utilize one or more of the mechanisms to enhance mixing. Due to their relative mechanical simplicity, passive mixing devices have been used extensively in scramjet development.

The use of normal fuel injectors is the most basic form of passive fuel injection. In transverse fuel injection flush fuel ports inject fuel at a 90-deg angle through the boundary layer into the freestream. The column of fuel then acts as solid rod, displacing the freestream flow around it. The displacement of the flow creates a bow shock wave that forms upstream of the injector, causing the boundary layer in front of the fuel injector port to separate creating a recirculation region[6, 13]. The flow phenomena created by normal fuel injection can be seen below in Figure 4.

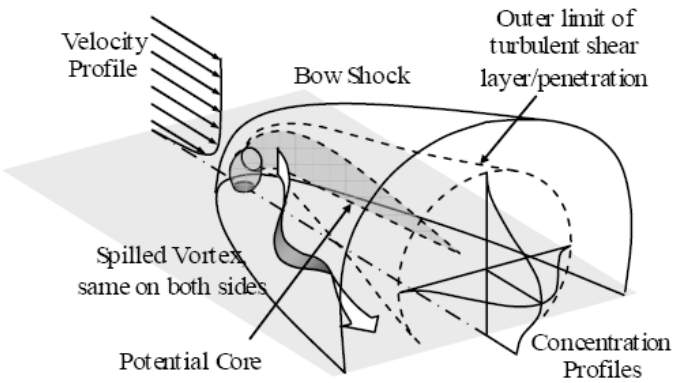

Figure 4. Normal Fuel Injection[13]

As the fuel plume begins to align with the freestream, the flow structure within the plume forms two streamwise orientated counter-rotating vortices[14]. These streamwise vortices entrain clean air from the freestream into the fuel plume, aiding in proper fuel-air mixing. Without an intrusive presence into the core flow, the use of normal fuel injection has relatively minimal cooling requirements. The complex downstream flow pattern produces relatively high levels of fuel air mixing[14] yet the pressure losses and total penetration of the fuel plume into the freestream air are highly dependent on the jet-to-freestream momentum flux ratio[15].

Parallel injection schemes have been well researched and have taken several different forms. Walker et al.[16] studied the fuel injection through a slot in downstream facing step and found that though penetration into the freestream and fuel air mixture was negligible, this fuel injection strategy suffered minimal pressure losses. Yu[17] showed that at flight Mach numbers above 10, the use of parallel and angled injectors can significantly add to net thrust. Parallel injection from the downstream face of a strut allows for desired penetration to be achieved based on the height of the strut; however, fuel mixing lengths can be 2-3 times larger when compared to normal fuel injection[18]. Experimental work by Naughton[19] added swirl to their parallel strut mounted fuel injector and found a 33% increase in mixing as compared to a baseline case with no induced swirl. The swirl-strut fuel injection scheme in Naughton's research can be seen in Figure 5. The large intrusive presence of the struts suffers high pressure losses and increased complexity due to internal plumbing and cooling requirements.

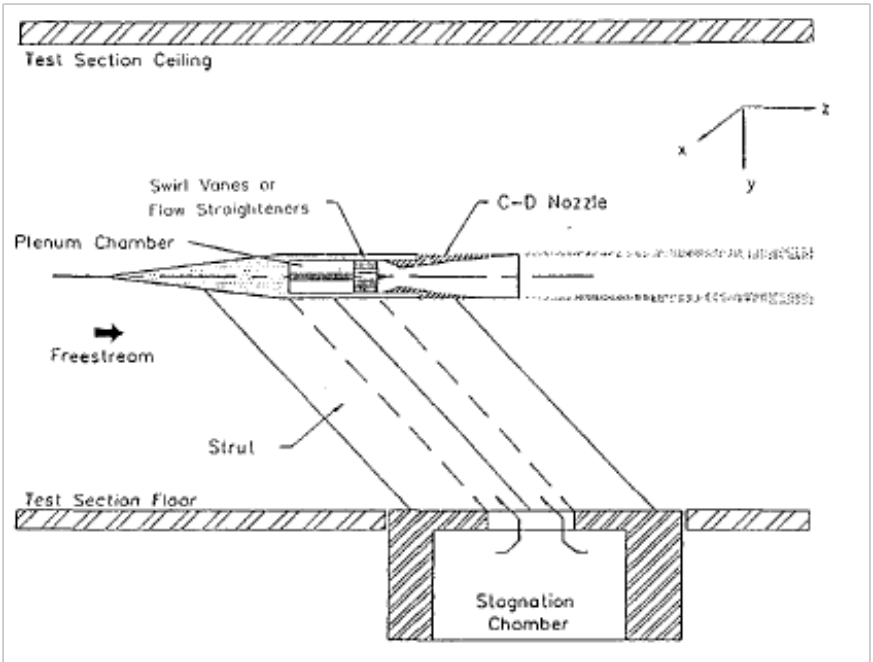

Figure 5. Parallel swirl fuel injector[19].

Ramp injectors represent an intrusive injection scheme that aims to convert a fraction of the freestream flow energy into tangential kinetic energy to create streamwise vortices[6] to aid in mixing. There are two basic forms of ramp injectors, compression and expansion. Compression ramps intrude into the freestream from a flat wall where the fuel is injected parallel to the compression surface. In an expansion ramp the wall turns away from the flow while the top surface of the ramp remains in the plane of the upstream wall. With the fuel injection nozzle exposed, the wall then turns back to be parallel with the upstream wall. The compression and expansion shocks from these ramps interact with the fuel plume to create baroclinic torque, which is essentially a misalignment of pressure and density gradients that can considerably increase mixing[20]. Swept ramps have slightly converging side walls, whereas unswept ramps have parallel side walls. Figure 6 illustrates a swept compression ramp and an unswept expansion ramp.

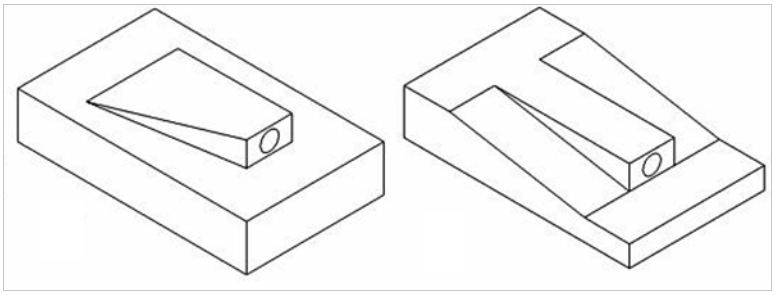

Figure 6. Illustration of a swept compression ramp and unswept expansion ramp[21].

The major disadvantage to using ramp injectors is the physically intrusive nature of the ramp and the creation of thermal "hot spots"[20]. A derivative of the ramp injector is the "aero-ramp" first offered by Cox et al.[22] The aero-ramp replaces the physically intrusive ramp with an array of closely spaced, flush mounted jets arranged to generate fuel vortex interactions. The aero-ramp presented better penetration and near field mixing as compared to the physical ramp with less pressure losses[20].

A less intrusive method for increasing fuel penetration is the use of pylon-aided normal fuel injection. In this technique fuel is injected into the low pressure region immediately behind thin triangular shaped pylon. Sometimes referred to as 'micro' pylons, the size of the pylons used in this fuel injection strategy are generally much smaller than typical ramp injectors with pylon widths on the order of 1-2 jet injector diameters wide and heights of less than ½ inch. Pylon-aided normal fuel injection has shown to lift the entire fuel plume away from the floor, limiting the possibility of flashback as well as providing significant improvement in penetration over baseline normal injection even at low jet-to-freestream momentum flux ratios[3]. Experimental results note that the presence of the pylons do not introduce significant pressure losses or

distortion of the airflow[18]. Figure 7 illustrates the geometry used in Gouskov's[2] pioneering work on pylon-aided normal fuel injection.

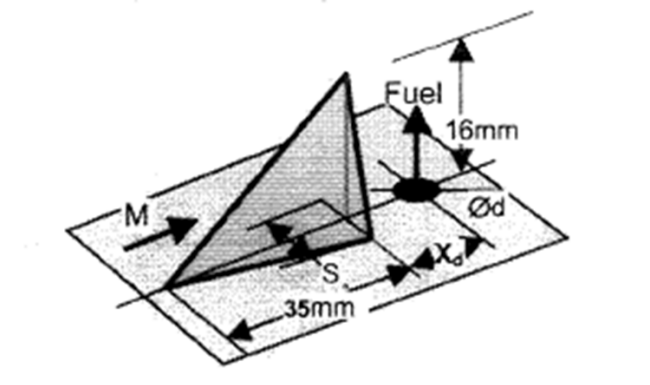

Figure 7. Basic geometry of pylon-aided normal fuel injection[2].

3. Methodology

3.1 Experimental Test Section

This numerical study is a direct follow-on to the experimental work performed by Haubelt[1]. In his work Haubelt investigated the suitability of three different pylon geometries for use in pylon-aided normal fuel injection. His work was conducted at the Supersonic Combustion Facility at the Air Force Research Laboratory, Propulsion Directorate. The test section included a 7 inch long by 6 inch wide by 2 inch tall constant area isolator placed immediately downstream of a Mach 2 nozzle. The test section containing the pylon/fuel-injector/flame-holding cavity is located on the floor of a 2.5° divergent ramp[1]. The computational domain axis system mirrors the wind tunnel axis system: the positive x coordinate is aligned with the direction of air flow as the streamwise direction, the positive y direction is in the vertical or transverse direction, and the spanwise z direction is perpendicular to both the airflow and transverse direction in accordance to the right hand rule. In this numerical study the computational domain includes both the test section and constant area isolator. Figure 8 illustrates the computational domain used in this parametric study.

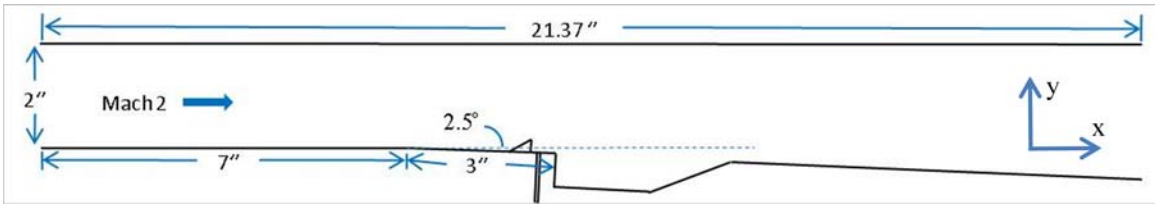

Figure 8. AFRL designed cavity with pylon installed upstream.

The AFRL designed flame-holding cavity used consists of a 90° backward facing step 0.65 inches deep followed by a 22.5° degree trailing edge ramp, producing a L/D ratio of 4.0. The 0.062 inch diameter (d) fuel injector port is located on the centerline of the test section 0.35 inches in front of the front face of the flame-holding cavity. The fuel injector is located at a fixed distance (X_p), 0.183 inches, behind the base of the pylon. Figure 9 illustrates the cavity-pylon-injector arrangement.

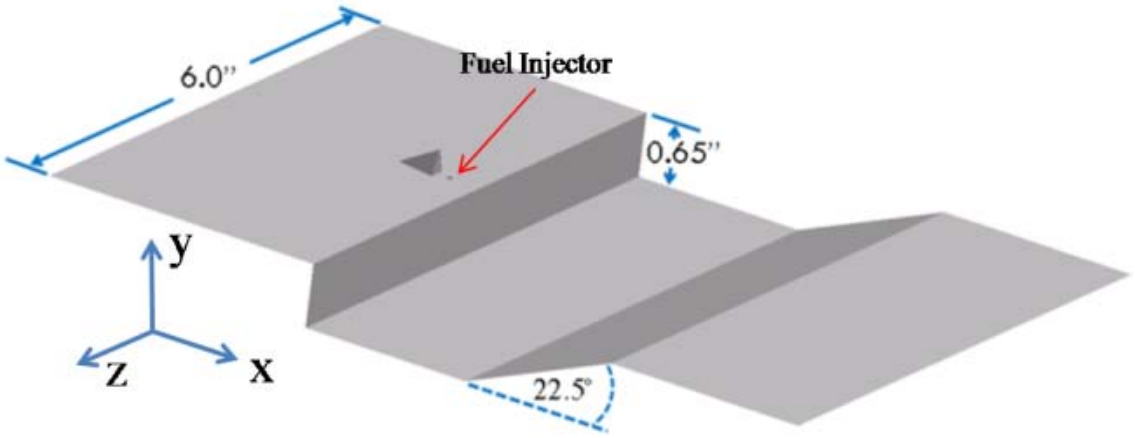

Figure 9. Pylon and flame-holding cavity geometry.

3.2 Pylon Geometry

Twenty different pylon geometries are investigated in this work in addition to a baseline case that represented pure normal fuel injection without the presence of a pylon. The first test matrix composed of seven different pylons representing a wide variation in pylon width (w), while maintaining a fixed height (h) and length (l) of the pylon. After investigation of the fuel plumes generated by this first initial test matrix, two pylons were chosen for the second and third test matrices. In these tests the absolute pylon height would be increased while maintaining a constant leading edge wedge angle (α) and pylon

width to height (w/h) ratio. The last test matrix is composed of 6 different variations in leading edge wedge angle while maintaining a fixed height and width. The general arrangement of the pylon geometries can be seen below in Figure 9.

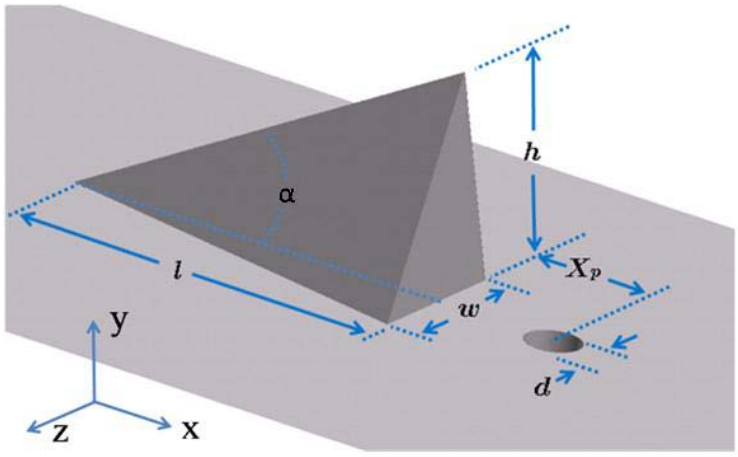

Figure 10. Pylon and fuel injection port diagram.

The rule of thumb in pylon-aided normal fuel injection has been to limit the pylon width to approximately 1-2 fuel injector diameters[2, 5, 18, 23] in order to minimize pressure losses. In the past the leading edge wedge angle has been determined mainly by the pylon material's heat absorption capabilities and conductivity, and the amount of convective cooling its base provides coupled with the gas spray fuel plume[2]. The bulk of published data on pylon-aided fuel injection have used leading edge wedge angles of approximately 25-30° [2, 4, 5, 18]. Initial testing of this concept of fuel injection was conducted with a liquid fuel injected in the shadow of pylons that had a 15° leading edge wedge angle.[24] Practical limitation such as maintaining pylon height of one quarter of the height of the combustion chamber[18] have been the only published guidelines this author has found that guide pylon height, albeit that the same material properties that limit the

length of the pylon, thermal loading and cooling requirements, would also apply to the height of the pylon.

The naming convention for the pylons used in this parametric study identifies the basic physical geometry of a pylons length, width and height, as scaled by the fuel injector diameter, followed by a modifier indicating how the base geometry was changed from the base pylon. For instance the LWH-7x1x4-8h pylon has the same leading edge wedge angle and width to height ratio as the LWH-7x1x4 pylon but has been scaled up to a total height of 8 diameters. The '-22°' modifier indicates that the pylon has the same height and width as the base pylon, but with an increased length that creates a leading edge wedge angle of 22°. The dimensions of the 20 pylons can be seen below in Table 1. In Figures 11-14 the pylon geometries for each set of test matrices are shown. Note the reader's perspective is from behind the pylon looking upstream.

Table 1. Physical geometries of pylons tested.

		Length (in)	Width (in)	Height (in)	Leading Edge Wedge Angle (°)	Rear Face Area (in²)
Test Matrix 1	**LWH-7x1/2x4**	0.43	0.03	0.25	29.74	0.0077
	LWH-7x1x4	0.43	0.06	0.25	29.74	0.0154
	LWH-7x2x4	0.43	0.12	0.25	29.74	0.0308
	LWH-7x3x4	0.43	0.19	0.25	29.74	0.0461
	LWH-7x4x4	0.43	0.25	0.25	29.74	0.0615
	LWH-7x5x4	0.43	0.31	0.25	29.74	0.0769
	LWH7x6x4	0.43	0.37	0.25	29.74	0.0923
Test Matrix 2	**LWH-7x1x4-5h**	0.54	0.08	0.31	29.74	0.0240
	LWH-7x1x4-6h	0.65	0.09	0.37	29.74	0.0346
	LWH-7x1x4-7h	0.76	0.11	0.43	29.74	0.0471
	LWH-7x1x4-8h	0.87	0.12	0.50	29.74	0.0615
Test Matrix 3	**LWH-7x2x4-5h**	0.54	0.16	0.31	29.74	0.0481
	LWH-7x2x4-6h	0.65	0.19	0.37	29.74	0.0692
	LWH-7x2x4-7h	0.76	0.22	0.43	29.74	0.0942
	LWH-7x2x4-8h	0.87	0.25	0.50	29.74	0.1230
Test Matrix 4	**LWH-7x2x4-15°**	0.93	0.12	0.25	15.00	0.0308
	LWH-7x2x4-22°	0.61	0.12	0.25	22.00	0.0308
	LWH-7x2x4-37°	0.33	0.12	0.25	37.00	0.0308
	LWH-7x2x4-45°	0.25	0.12	0.25	45.00	0.0308
	LWH-7x2x4-50°	0.21	0.12	0.25	50.00	0.0308

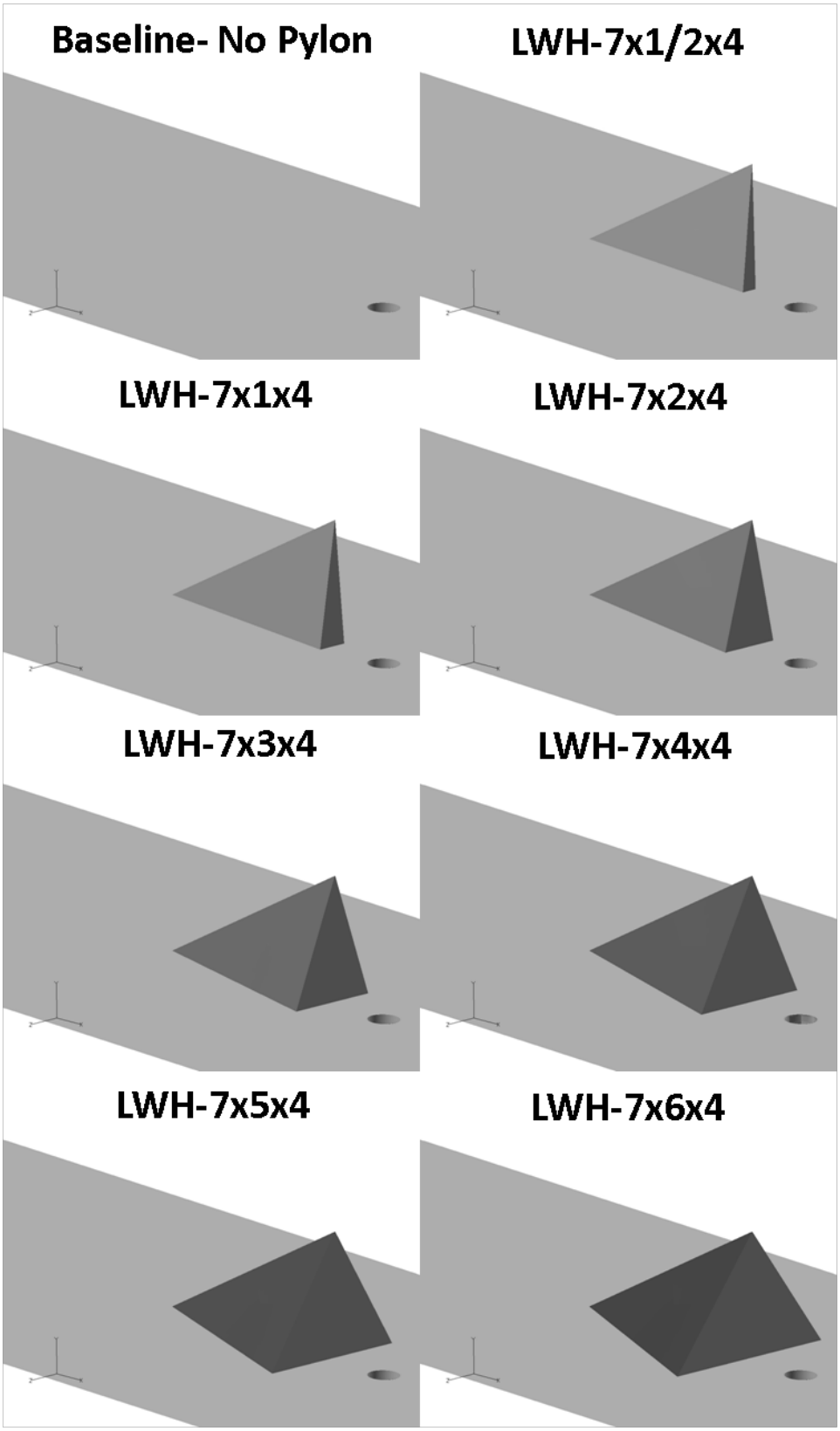

Figure 11. Test matrix 1 pylons representing variations in pylon width.

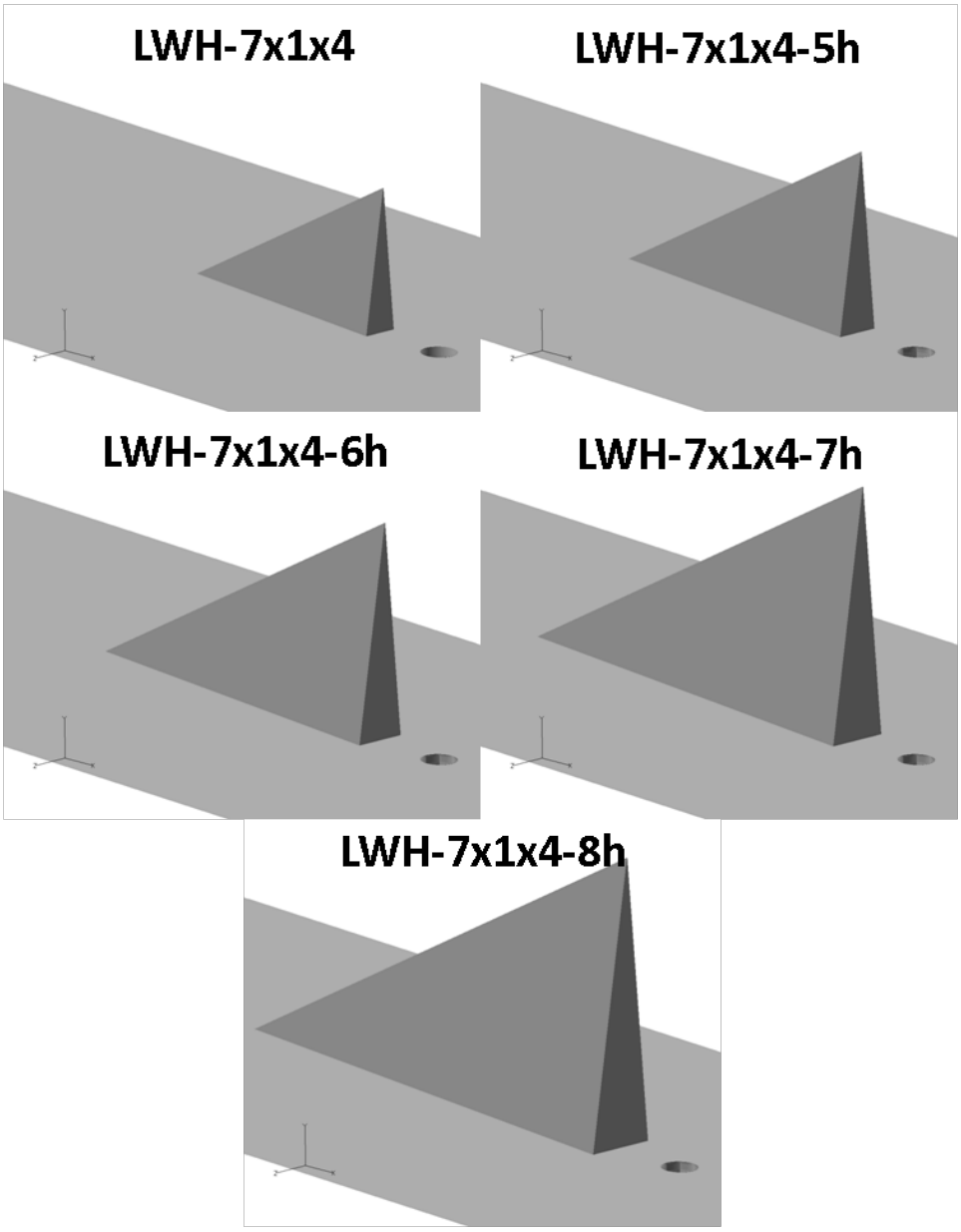

Figure 12. Test matrix 2 pylons representing variations in the LWH-7x1x4 pylon's absolute height.

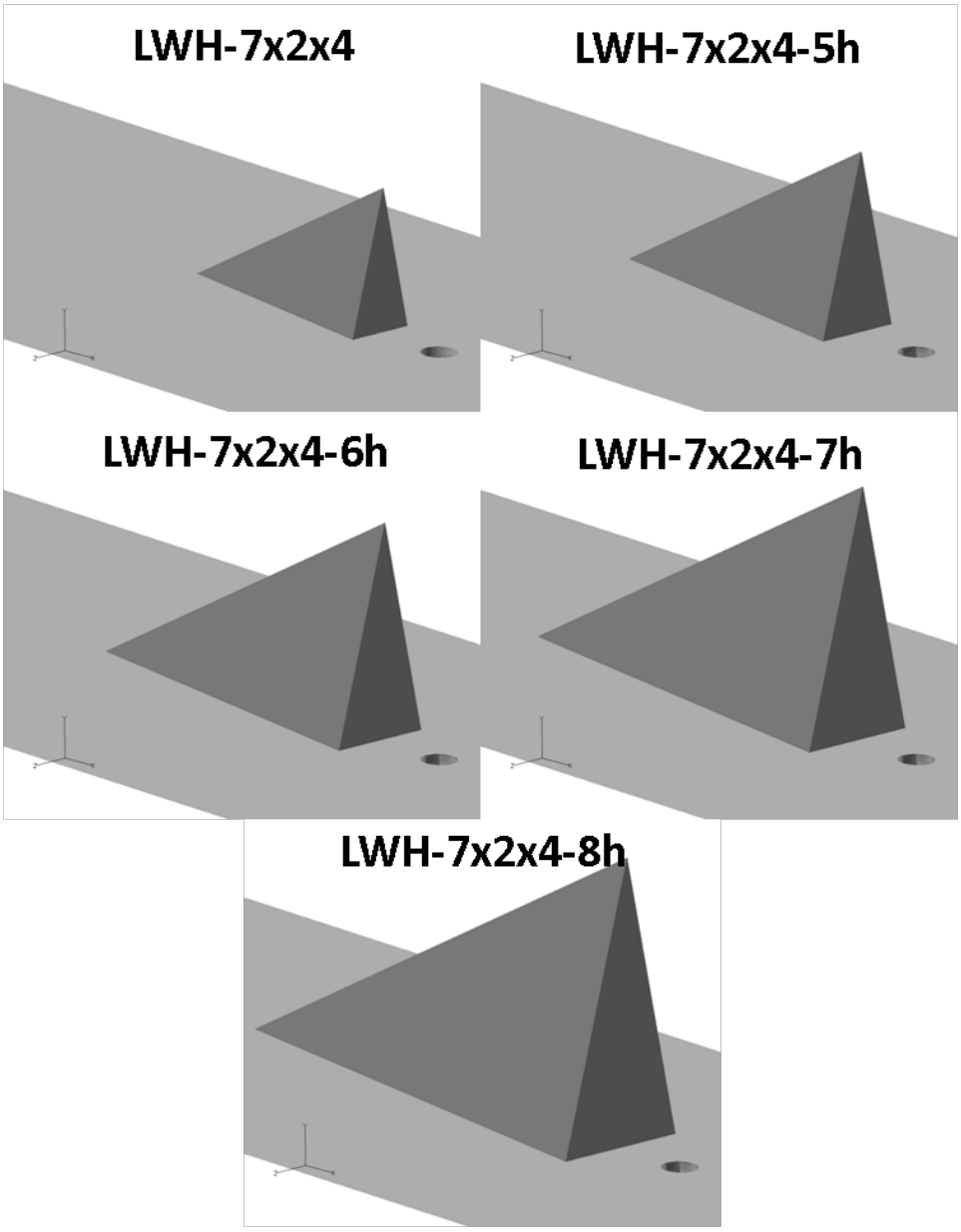

Figure 13. Test matrix 3 pylons representing variations in the LWH-7x2x4 pylon's absolute height.

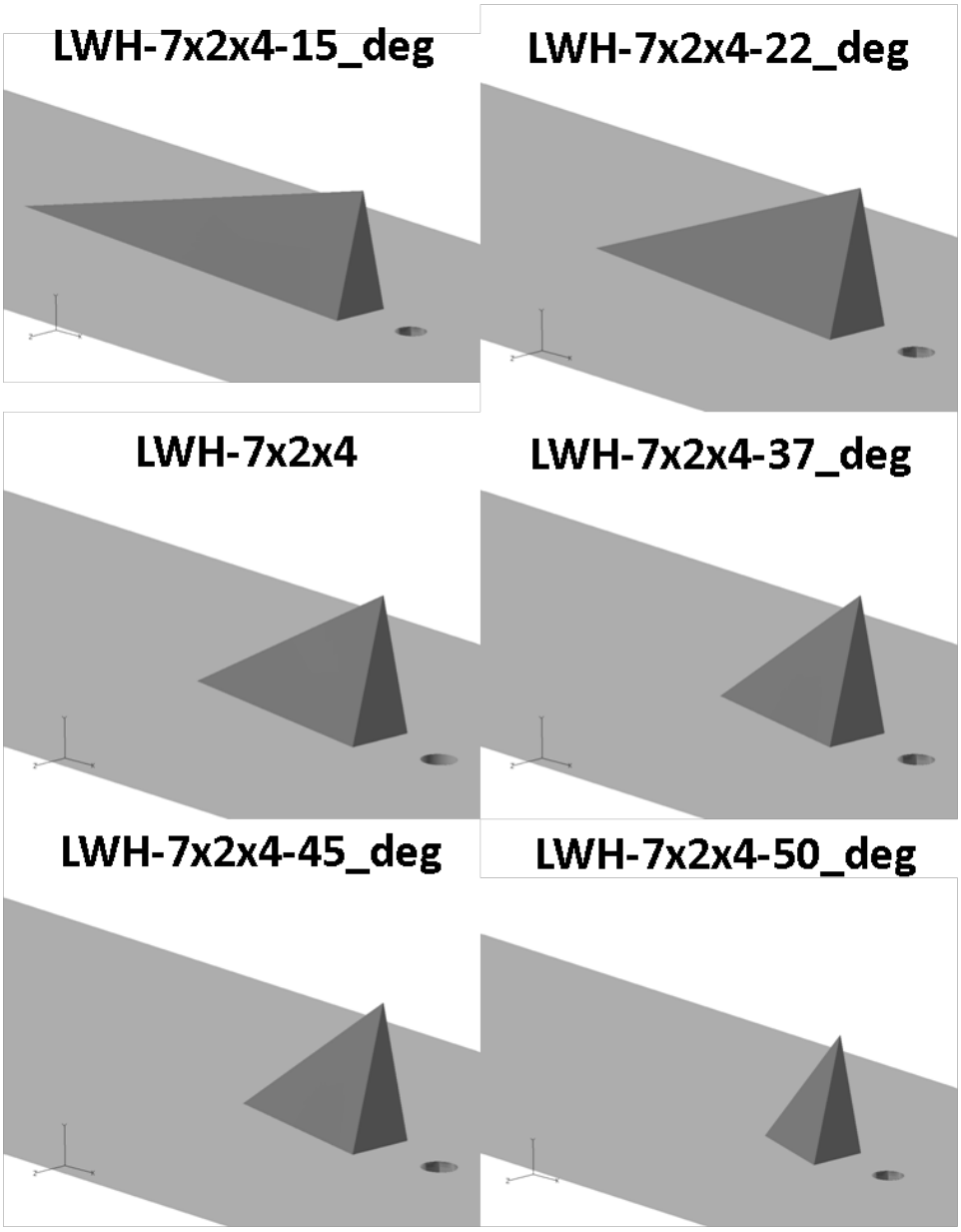

Figure 14. Test matrix 4 pylons representing variations in the LWH-7x2x4 pylon's leading edge wedge angle.

3.3 Flow Conditions

As an extension to the experimental work, the freestream and injection port flow properties in this numerical study were set to duplicate the wind tunnel conditions found in Haulbelt's[1] work. All tests were conducted with a freestream velocity of Mach 2.0 at the inlet of the computational domain. Flow conditions were set for a total pressure of 50 psia and a total temperature of 550° R. Gaseous ethylene (C_2H_4), at an injection pressure of 200 psia and a mass flow rate of $1.4x10^{-2}$ lb/sec, was used as the fuel for these studies. The freestream and fuel injection flow conditions can be seen below in Table 2.

Table 2. Inlet and fuel injector flow conditions.

	Freestream Inlet	**Fuel Injection Port**	
M	2.0	1.0	-
P_t	341.9	1379.0	kPa
T_t	305.5	286.7	K
P	43.7	730.8	kPa
T	169.7	240.6	K
a	261.2	286.2	m/sec
ρ	0.897	11.245	kg/m^3
γ	1.40	1.25	-
$\dot{m}$	3.63	$6.35x10^{-3}$	kg/sec

As stated previously, an important characteristic of a fuel mixing study is the non-dimensional jet-to-freestream momentum flux ratio ($\bar{q}$). Also known as the dynamic pressure ratio this characteristic is defined as:

$$\bar{q} = \frac{(\rho u^2)_{jet}}{(\rho u^2)_\infty} = \frac{(\gamma P M^2)_{jet}}{(\gamma P M^2)_\infty} \quad (1)$$

where the subscript ‘jet’ identifies the properties for the fuel injectant, ∞ is the freestream properties, and γ is the ratio of specific heats. The dynamic pressure ratio was held constant at 4.0 for all test cases.

3.5 Computational Grid

Structured grids, each containing approximately 4.3 million cells, where created using GRIDGEN for each of the 21 test cases. Since the experimental domain is symmetric about the centerline, the computational domain consisted of only half of the test section. Using a symmetry plane in the computational domain allowed for a more refined mesh for the given number of grid points. Figure 15 illustrates a grid used for each of the pylons. Note, not shown in this view are the external side wall, centerline boundary condition, and ceiling of the test section. The pylon and fuel injector are bisected by the line of symmetry that extends the entire streamwise and transverse directions at the $z = 0$ coordinate, the grid immediately surrounding the pylon and fuel injector can be seen in Figure 16.

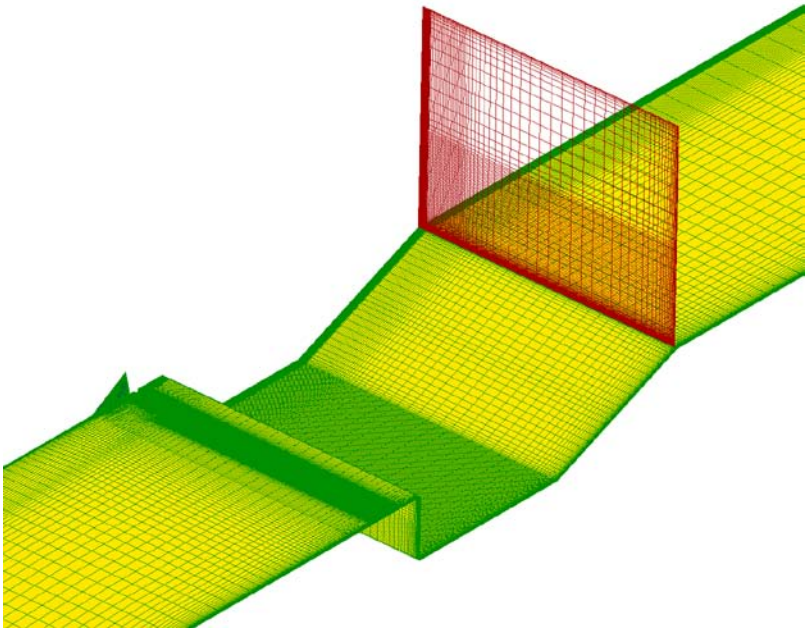

Figure 15. Typical CFD internal grid layout.

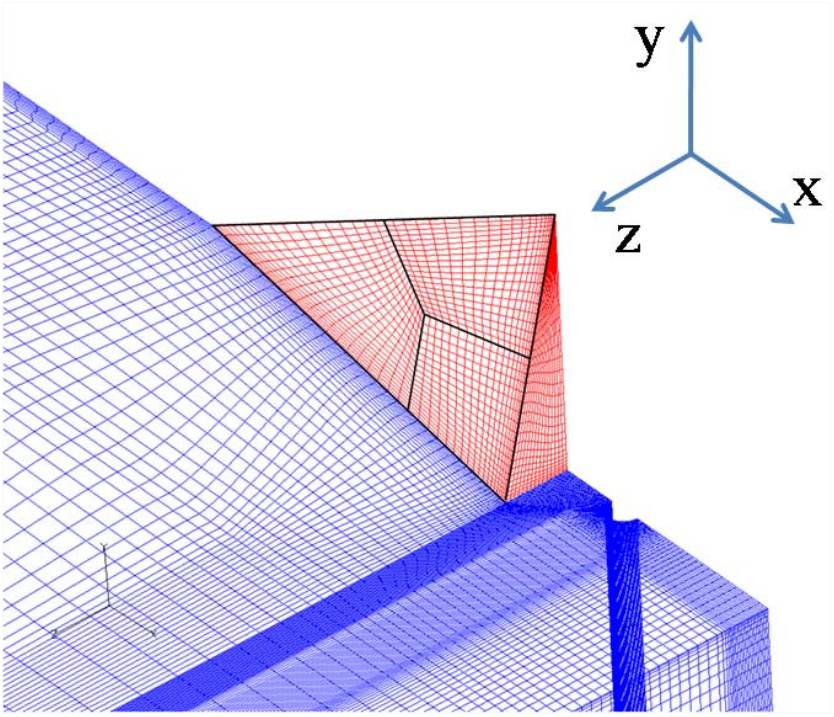

Figure 16. Detail of CFD grid surrounding the pylon and fuel injector.

Since the numerical solver used in this study utilizes structured grids and cannot use singularities, the triangular shape of the pylons had to be modified for proper mesh development. In place of a singularity at the apex of the rear face of the pylon, a minutely small edge was used in such a fashion that the rear face formed a quadrilateral. This small face extended down the 'spine' of the leading edge of the pylon as well. In Figure 17 this 'pseudo-singularity' can be seen at the apex of the pylon as the various views zoom further into the tip of the pylon.

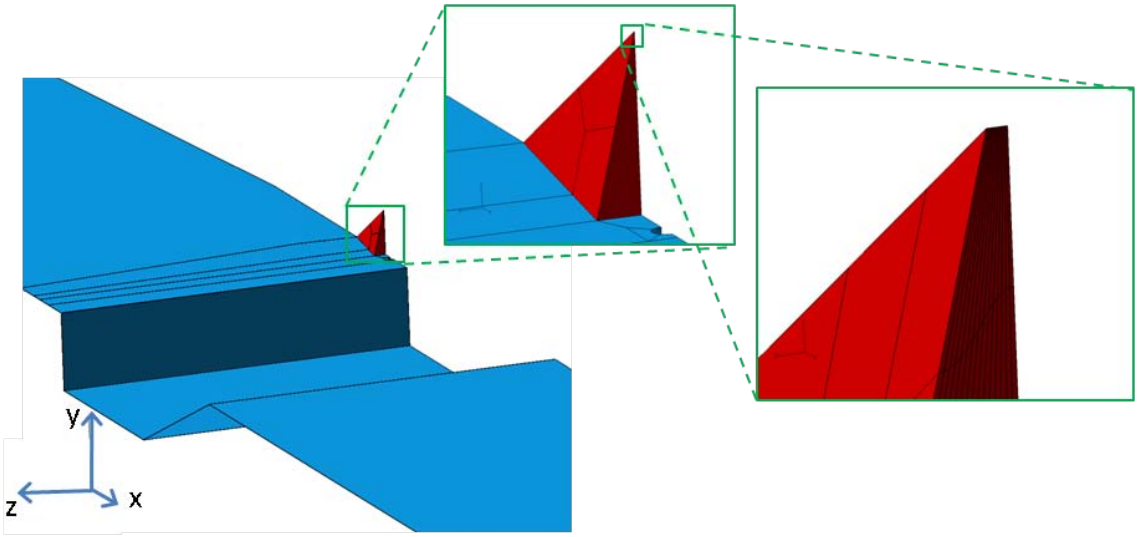

Figure 17. Zoomed view of the rear face of the pylon showing the 'pseudo-singularity' at the pylon apex.

In order to ensure proper capture of small scales of mixing within the fuel plume, a highly refined mesh was created in the wake region of the pylons. The high density of grid points in this region extended streamwise approximately 60 diameters downstream of the pylon, 4 diameters in the spanwise direction, and 16 diameters in the transverse direction yielding cell volumes of approximately 1/8 mm^3. Since the grids used in this

study have a very fine mesh (over 4.3 million cells with 1/8 mm^3 cell volumes in the pylon wake region) a grid convergence study was not undertaken.

3.5 Computational Boundary Conditions

Since the focus of this study is the mixing characteristics of non reacting flow, some levels of fidelity can be decreased in order to aid in the computational speed of the simulations. With no chemical reactions present it was unnecessary to include the products of combustion in this study. Therefore, the conservation of mass equation needed to only be solved for thermally perfect air and gaseous ethylene, greatly reducing the numerical complexity of these simulations.

The entire computational domain consisted of four boundary conditions. The inlet to the test section, representing the furthest upstream location, is composed of a uniform, fully developed supersonic inflow[25] boundary condition for thermally perfect flows. The boundary layer thickness, seen in Haulbelt's experimental work[1], at the exit of the nozzle/ isolator inlet was unknown. Therefore, no artificial boundary layer thickness was inserted at the far upstream location. Numerical simulations by Gouskov[2] indicated that proper boundary layer modeling and therefore boundary layer thickness has negligible impact on fuel-air mixing metrics. The supersonic inflow boundary condition allows the user to specify species mass fractions, density, velocity, temperature, turbulent intensity, and the turbulent to molecular viscosity ratio. This same boundary condition was used as the fuel injector inlet. The exit of the test section consists of a supersonic

outflow boundary condition with zeroth order extrapolation of all variables[25]. The centerline of the test section used a generic symmetry boundary condition.

The test section walls and the pylon surface are composed of a no slip adiabatic wall using wall functions specifically designed for y+ values greater than 2.0 or 3.0. Using AFRL/RZ common practice techniques[26] an initial wall spacing of $1x10^{-3}$ inch was used throughout the domain resulting in wall y+ values greater than 30 on the pylon and within the flame-holding cavity. The y+ values for a typical simulation test run can be seen below in Figure 18.

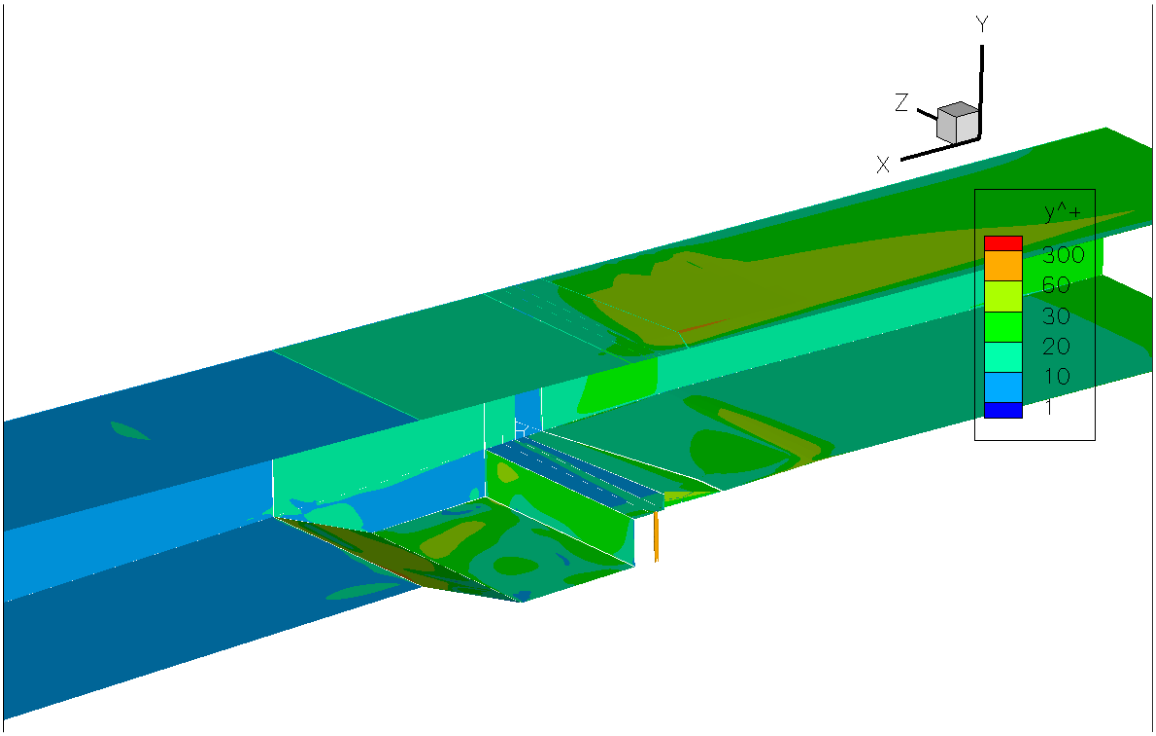

Figure 18. Wall y+ values for LWH-7x2x4-15° test case.

3.6 Flow Solution

The Computational Fluid Dynamics code employed in these simulations was the VULCAN[25] code developed at the NASA Hypersonic Air Breathing Propulsion Branch. The k-ω turbulence model was utilized in conjunction with a multiple-species formulation of the viscous and compressible Navier Stokes flow equations. An elliptic solver using the Edwards low dissipation flux split scheme and a second order Fromme MUSCL scheme with a smooth flux limiter was used in these simulations. In order to properly initialize the flow the computational blocks behind the pylon and on the front face of the flame-holding cavity were set at zero velocity to prevent the formation of a vacuum. Failure to initialize these regions to zero velocity led to a quickly divergent solution in early attempts. All test cases were initially run as laminar cases with the turbulence model disabled. Running laminar flow initially enabled the use of a much larger CFL number (5) and therefore attainment of a converged laminar solution relatively quickly. The ability to use restart files in VULCAN allowed for the use of the laminar restart files from one geometry as the starting point for other grid/ pylon geometries.

Once each of the five pylon geometries had converged in a laminar sense the CFL number was reduced to 0.1 and the turbulence models were then enabled. The simulations proved to be very sensitive to the CFL number, in some simulations the CFL was able to be increased to 0.5. However, this higher CFL value caused most other simulations to quickly diverge and fail. The solution then ran until the convergence criteria was reached. The two convergence criteria were established as a mass flow rate imbalance of less than 1% or a three-orders reduction of the magnitude of the L2 norm.

In practice the L2 norm convergence criteria approached but rarely reached a three order of magnitude reduction required to deem the solution 'converged' and therefore the mass flow rate convergence criteria was used for all simulations.

The k-ω turbulence model was chosen for several reasons. The large number of pylons to be tested combined with the relatively short period of time available to run these simulations placed a premium on computational speed. This time constraint eliminated the more complex turbulence models such as the Large Eddy Simulation turbulence model found in VULCAN. Accuracy was another prime driver in determining the turbulence model used; with large regions of separated flow a simple 1-equation models such as the Spalart-Allmaras turbulence model could not be used[33]. The k-ω turbulence model has been shown to accurately match spreading properties of separated flows[33]. Attempts to use Menter's Shear Stress Transport model were hampered by stability and run-time issues and could not be used in these simulations.

4. Results and Analysis

4.1 Data Reduction

Figure 19 depicts the data reduction planes used in this study. Twelve downstream locations were chosen for reduction of the key areas of merit. Fuel-air mixing metrics include: mixing efficiency (η), fuel plume area (A_p), flammable fuel plume area (A_f) , flammable fuel plume percentage (FPP), species composition contour plots, decay of maximum equivalence ratio (Φ_{max}), and flammable mixture distance (x_{fmd}). Fuel plume penetration height (h_p) and plume core penetration height (h_c) are used to evaluate fuel plume penetration into the freestream. All fuel-air mixing and penetration metrics are compared against a total pressure loss coefficient (ω) to track the losses associated with the various pylon geometries. The twelve data reduction planes correspond to x/d locations of 5, 10, 15, 20, 25, 30, 35, 40, 50, 60, 70, and 80.

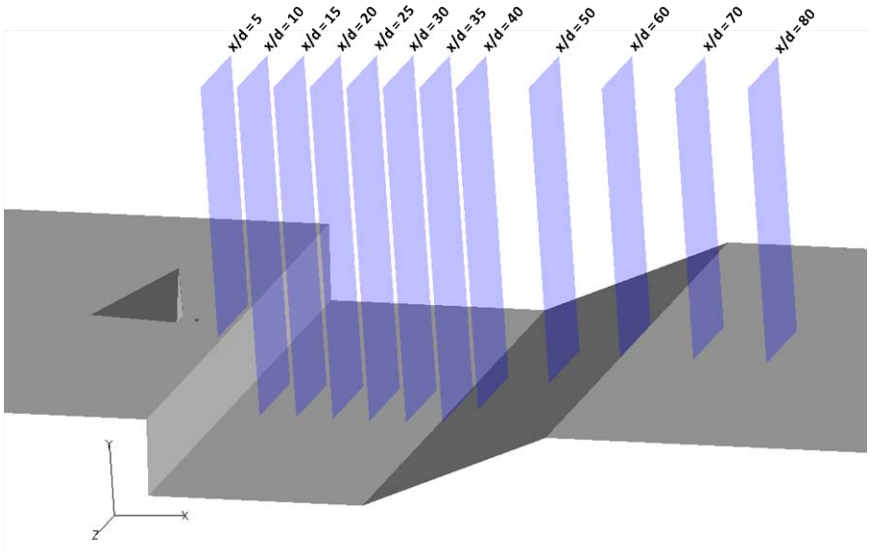

Figure 19. Illustration of the 12 downstream data reduction planes.

The fuel-air mixing metrics data presented here are in a non-dimensional form. Common practice for fuel injection studies, such as this work, is to normalize all length quantities by the fuel injector diameter. Similarly all areas presented here have been normalized by the area of the fuel injector port. Quantities such as the total pressure loss coefficient and mixing efficiency are already in non-dimensional form.

4.2 Fuel-Air Mixing Metrics

In order to evaluate the fuel-air mixing effectiveness and penetration of each of the pylons, nine fuel-air mixing metrics are tracked. The fuel plume flow structure of each of the pylons, seen in the species contour plots, will provide additional insight into how the relative shape, size and position of fuel plume is affected by pylon geometry. Since the mass flow rate and injection pressure of the fuel is constant for all test cases, the nine quantitative fuel-air mixing metrics and qualitative species contour plots will be an evaluation solely of the pylon's impact on fuel-air mixing.

The equivalence ratio (Φ) offers considerable insight into the combustibility of the fuel-air mixture. It is defined as the ratio of the local fuel-air mass ratio to the fuel-air mass ratio for a stoichiometric process. A stoichiometric process is one in which the reactants and the products of a chemical reaction are balanced, in this case where there is just enough air present for complete combustion of the local ethylene. Equation 2 presents the equivalence ratio:

$$\Phi = \frac{(F/A)}{(F/A)_{stoich}} \tag{2}$$

where

$$F/A = \frac{mass\ of\ fuel}{mass\ of\ air} \tag{3}$$

In terms of Φ, a stoichiometric process occurs when Φ = 1. A fuel lean mixture occurs when Φ <1; alternatively Φ > 1 indicates a fuel rich mixture. The stoichiometric fuel-air mass ratio is constant for a specific reaction. To determine this quantity a chemical reaction is written in terms of one mole of a hydrocarbon fuel completely combusting with air to form the products of carbon dioxide, water and nitrogen. Kuo[27] represents a generic hydrocarbon reaction in the following manner:

$$C_aH_b + mol_{air}(O_2 + 3.76N_2) \rightarrow aCO_2 + (b/2)H_2O + 7.52mol_{air}N_2 \tag{4}$$

where

$$mol_{air} = a + b/4 \tag{5}$$

For ethylene, a = 2 and b = 4 (C_2H_4). The stoichiometric fuel-air mass ratio is found in Equation 6 where MW represents the molecular weight of air and the fuel.

$$(F/A)_{stoich} = \frac{1}{4.762\ mol_{air}} \frac{MW_{air}}{MW_{fuel}} \tag{6}$$

For ethylene this leads to a $(F/A)_{stoich}$ of 0.0678.

An empirical one-dimensional measure of the degree of mixing completeness is the mixing efficiency (η). Anderson[28] defines mixing efficiency as the amount of fuel

that would react if complete reaction occurred without further mixing divided by the amount of the amount of fuel that would react if the mixture were uniform. The mass fraction of fuel in air (X) can be determined by the local equivalence ratio and the stoichiometric fuel-air mass ratio; this quantity can be seen in Equation 7. The mass fraction of ethylene in air at stoichiometric conditions (X_{stoich}) can be found by using Equation 7 and setting $\Phi = 1$; for ethylene $X_{stoich} = 0.0635$.

$$X = \frac{\Phi\,(F/A)_{stoich}}{\Phi\,(F/A)_{stoich}+1} \tag{7}$$

The globally lean fuel mixing environment in this fuel-mixing study assumes that the air is completely mixed and the fuel is the reactant of interest to be mixed. Mixing efficiency for a globally fuel-lean situation[29] is depicted below in Equation 8.

$$\eta = \frac{\int X_r \rho u dA}{\int X \rho u dA} \tag{8}$$

where

$$X_r \equiv \begin{cases} X & X \leq X_{stoich} \\ \frac{1-X}{1-X_{stoich}} X_{stoich} & X > X_{stoich} \end{cases} \tag{9}$$

The total fuel plume area (A_p) was defined as the area encompassing the contour level of $\Phi = 0.2$ in each data reduction plane. This value of equivalence ratio was chosen since it was sufficiently below the lower flammability limit of ethylene and is consistent with previous experimental work[1, 3]. It is a measure of the expansion of the physical size

of fuel plume, but not necessarily indicative of the effectiveness of fuel-air mixing. Like fuel plume area, mixing efficiency is a less than ideal metric to properly analyze the fuel-air mixing effectiveness. Mass fractions below stoichiometric, considered perfectly mixed, include regions below the threshold for combustion. Similarly flammable mixtures exist above the stoichiometric conditions[30].

A more pertinent metric is the flammable fuel plume area (A_f). The flammable fuel plume area is bound by both the upper ($\Phi_u = 5.5$) and lower ($\Phi_l = 0.4$) flammability limits of ethylene in air at standard temperature and pressure[31]. Any portion of the fuel plume that is outside of the flammability limits is not in the proper concentration to support combustion. Another key metric is the flammable plume percentage (FPP), as seen in Equation 10. This metric represents the percentage of the fuel plume that is within the defined flammability limits:

$$FPP = \frac{A_f}{A_p} \times 100\% \tag{10}$$

Since hydrocarbon fuels are known to combust above their stoichiometric concentration level, the downstream distance required to reach stoichiometric levels is not extremely pertinent to a mixing analysis. A more telling metric is downstream location where the maximum concentration of the fuel plume is no longer above Φ_u. This distance is referred to the flammable mixture distance (x_{fmd}). The entire fuel plume beyond x_{fmd} is at or below the maximum equivalence ratio required for combustion.

The maximum plume penetration height (h_p) is determined by the maximum transverse distance from the injector port to the edge of the fuel plume ($\Phi = 0.2$). The

decay of maximum equivalence ratio (Φ_{max}) tracks the decay of maximum fuel concentration within the fuel plume in the downstream direction. The location of Φ_{max} within the fuel plume is termed the core penetration height.

The aerodynamic losses or penalty associated with the various injection strategies can be measured by use of a total pressure loss coefficient (ω). This coefficient is found by the mass averaged integral of total pressure as seen below in Equation 11: The data reduction planes spanned the entire test section, from floor to ceiling and centerline to wall.

$$\omega = 1 - \frac{\bar{P}_t}{P_{t_{ref}}} \tag{11}$$

where $P_{t\,ref}$ is the total pressure found at the inlet boundary condition and $\overline{P_t}$ is found from:

$$\overline{P_t} = \frac{\int P_t \rho u dA}{\int \rho u dA} \tag{12}$$

In order to capture the entire structure of the bow shock and the impact of local flow momentum changes brought on by the flow structure within the fuel plume, the cross section of the data collection planes spanned the entire area of the test section. The total pressure loss coefficient ranges from 0, no loss, to 1, complete loss. Therefore small values of ω are desired.

The species contour plots allow for a qualitative analysis of the fuel plume flow structure and general comparisons in the size, shape, location, penetration and floor-gap provided by each of the different pylon geometries.

4.3 Mixing Analysis of Test Matrix 1- Variations in Pylon Width

Species Contour Plots

The first portion in this numerical study was to attempt to identify basic flow structures and fuel-air mixing metrics associated with variations in pylon width. The geometries studied in the first test matrix all share common pylon lengths, height and thus wedge angles. The species contour plot for the baseline test case with no pylon and seven pylons of differing widths can be seen below in Figures 20-27. These figures illustrate the mass fraction of the ethylene over seven downstream locations across the flame-holding cavity. The contours are orientated such that the reader is looking downstream from the pylon. Due to the symmetrical nature of this simulation only half of the contour is presented. The origin of each of the individual contour plots is located at the center of the fuel injector port. The major tick marks on both axes represent a distance of one diameter. To aid in comparison between the different pylon geometries the contour color scales are the same for all plots

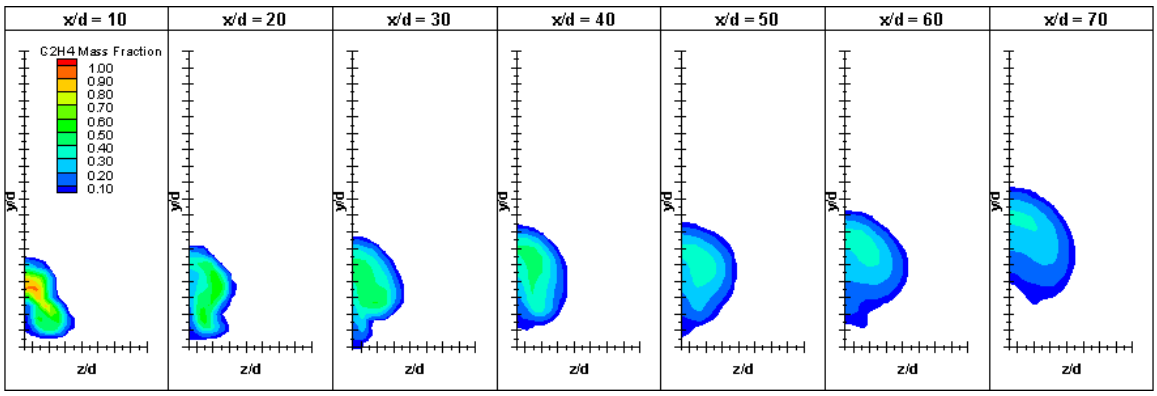

Figure 20. Baseline, no pylon, fuel species contour plot of C_2H_4.

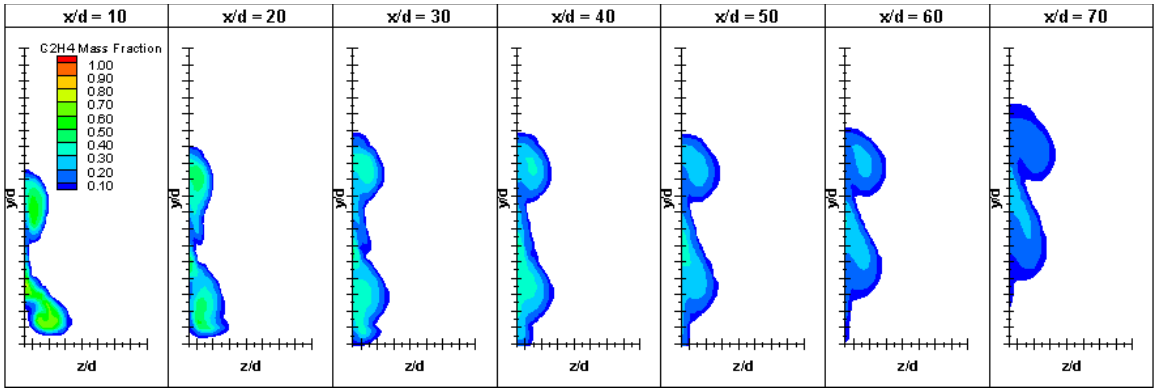

Figure 21. LWH-7x1/2x4 fuel species contour plot of C_2H_4.

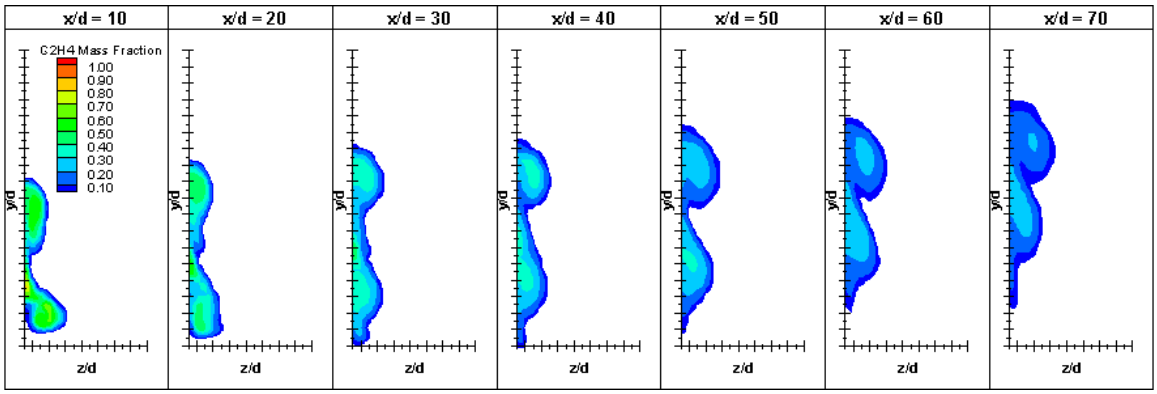

Figure 22. LWH-7x1x4 fuel species contour plot of C_2H_4.

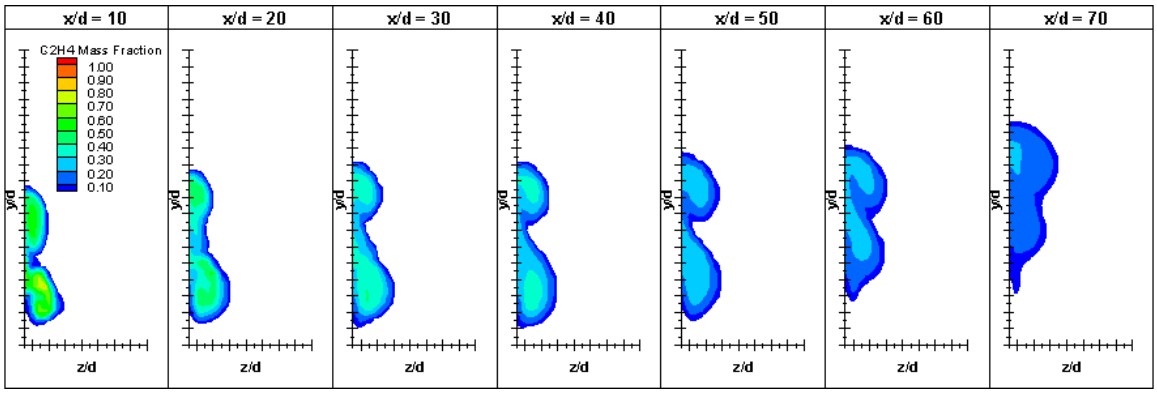

Figure 23. LWH-7x2x4 fuel species contour plot of C_2H_4.

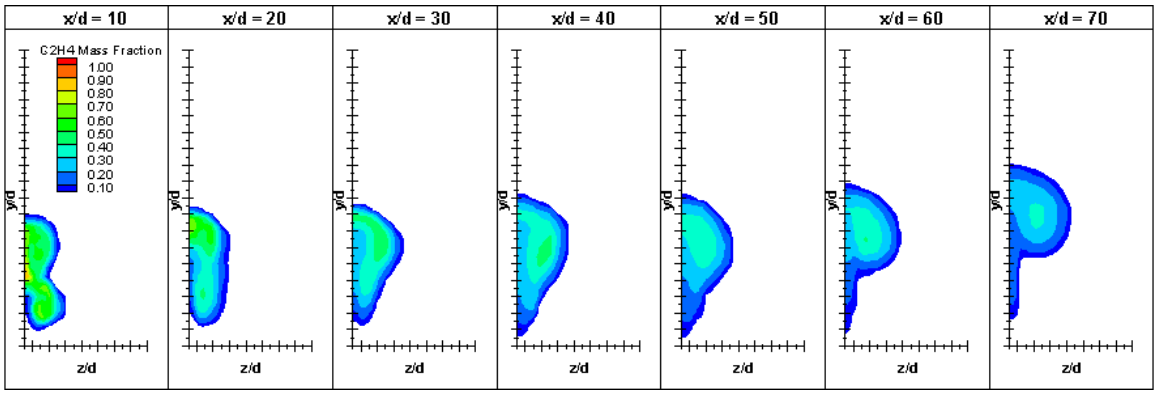

Figure 24. LWH-7x3x4 fuel species contour plot of C_2H_4.

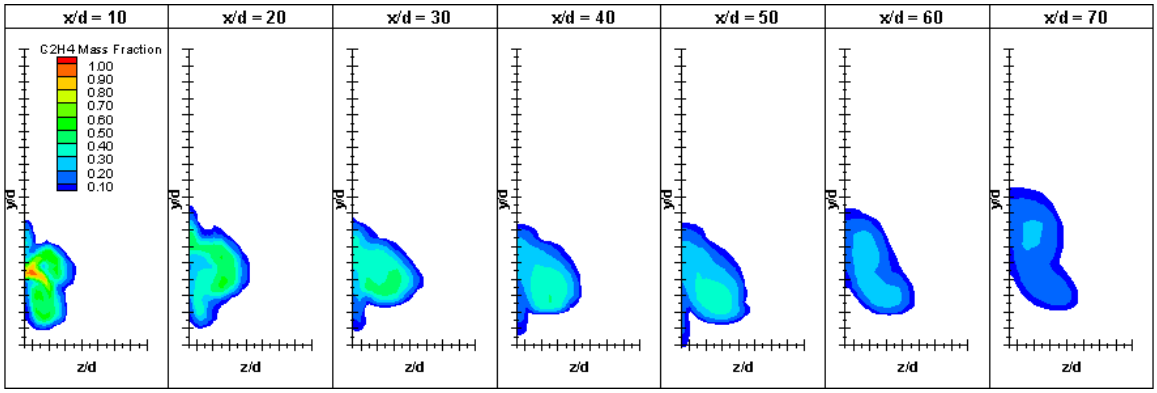

Figure 25. LWH-7x4x4 fuel species contour plot of C_2H_4.

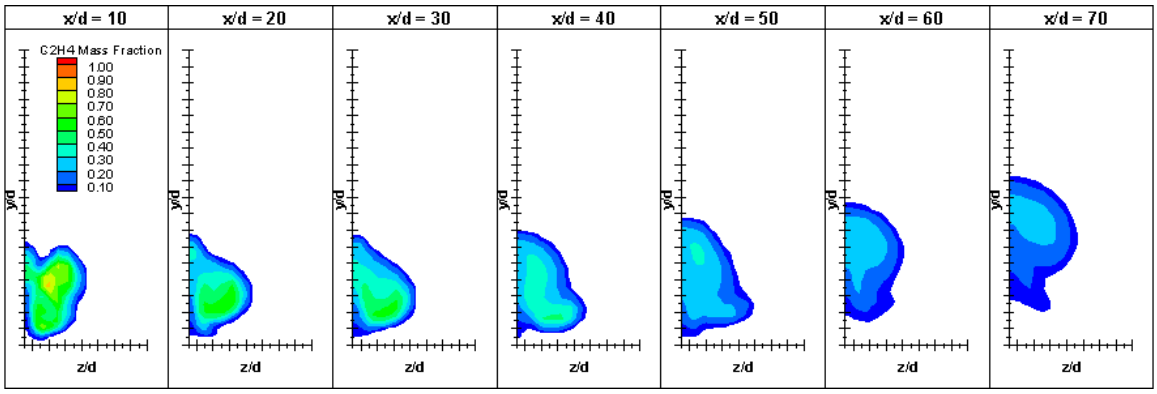

Figure 26. LWH-7x5x4 fuel species contour plot of C_2H_4.

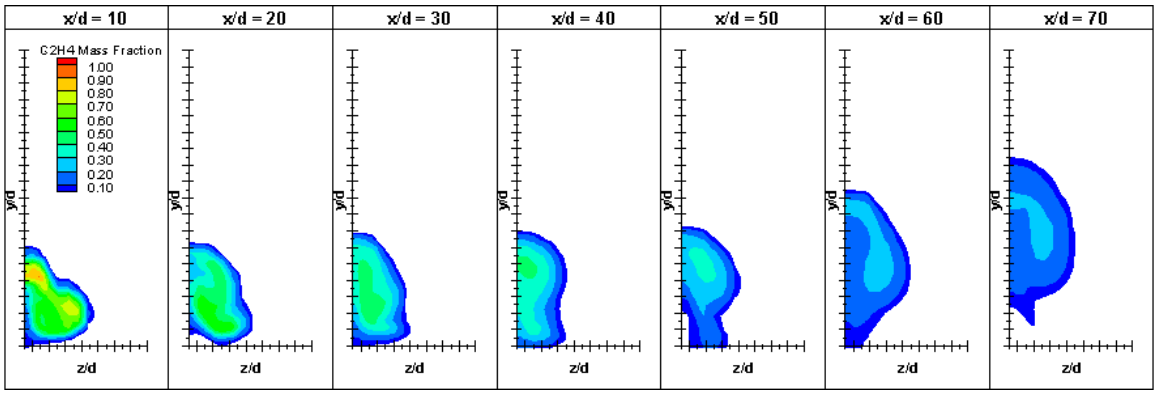

Figure 27. LWH-7x6x4 fuel species contour plot of C_2H_4.

The species concentration plots in Figures 21 through 23 illustrate a similar plume structure resulting from the LWH-7x1/2x4, LWH-7x1x4, and LWH-7x2x4 pylons. These pylons will be referred to as 'narrow' pylons in further discussion. In these plots the fuel is concentrated in two sets of counter-rotating vortices, one each located at the top and one at the bottom of the tall and narrow fuel plumes. The 2-diameter width pylon shows the greatest amount of floor-gap, where the bottom of the fuel plume is well above the floor of the test chamber.

The LWH-7x3x4 pylon appears to be a transition width between the narrow and wide pylons. The same double set of counter-rotating vortices that dominate the narrow

pylons is seen in the LWH-7x3x4 pylon. However, these vortices merge between the x/d = 20 and 30 locations forming one large set of counter rotating vortices. Past this point the fuel plume behaves much like that of the wide pylons.

Vorticity and Velocity Vector Plots

More insight into the fuel plume structure can be gained by overlaying the velocity vector components normal to the main incoming flow on top of the Φ contour plots. Overlaying the vector plots onto the species contour plots allows easy identification of the locations and relative strength of the vortex structures. The relative magnitude of the velocity vector is indicated by the size of the arrow. Figures 28 through 40 are orientated such that the reader is looking upstream at the back of the pylon towards the front face of the flame-holding cavity.

Figure 28 illustrates the flowfield associated with the baseline test case that has no pylon. The fuel injector is barely visible in this view but can be discerned in the lower left portion of the transparent x/d = 5 plane. The fuel plume for the baseline normal fuel injection case is dominated by one large set of counter-rotating vortices and matches the behavior seen in previous numerical[15] and experimental[1, 3, 14] work.

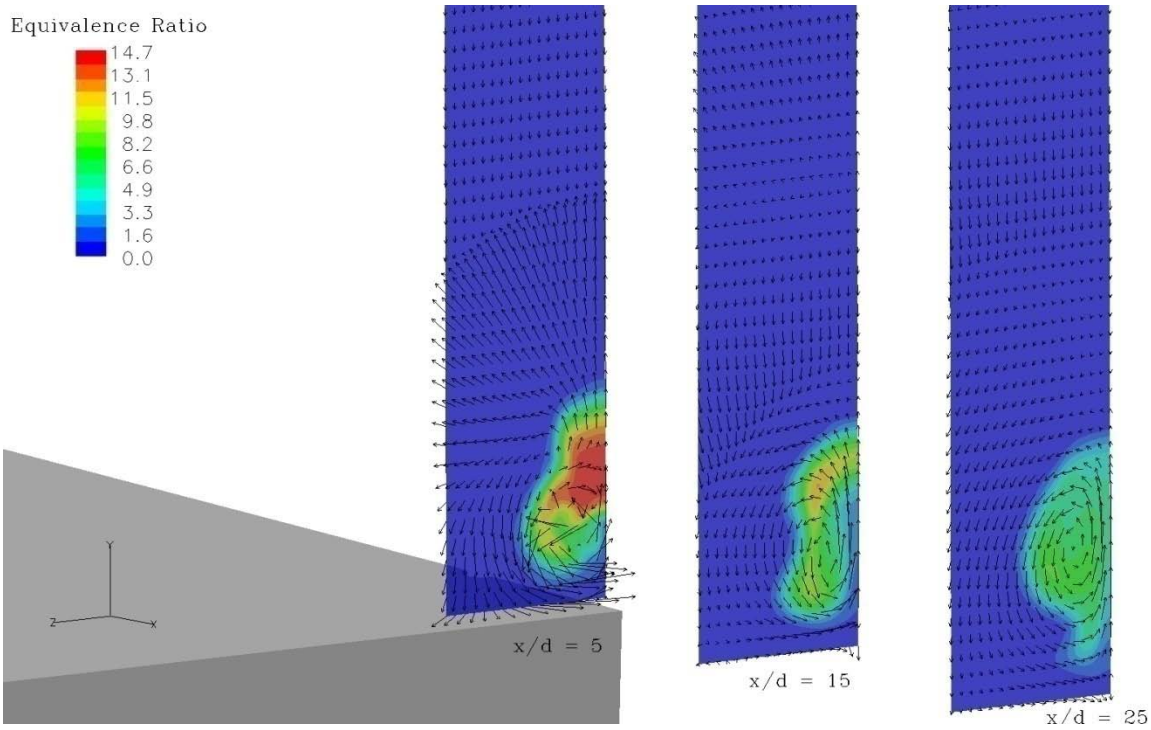

Figure 28. Equivalence ratio contour/velocity vector plot for the baseline- no pylon test case.

A similar view of the vorticity in the flowfield at the same x/d locations will enable quantitative analysis of the streamwise vorticity inherent in each of the fuel plume structures. In Figure 29 the vorticity of the baseline case is shown with the same velocity vectors overlaid. The color scale has been inverted from the equivalence ratio plots for distinction. The bow shock can be seen at the x/d = 5 location where the velocity vectors are seen to form an arc.

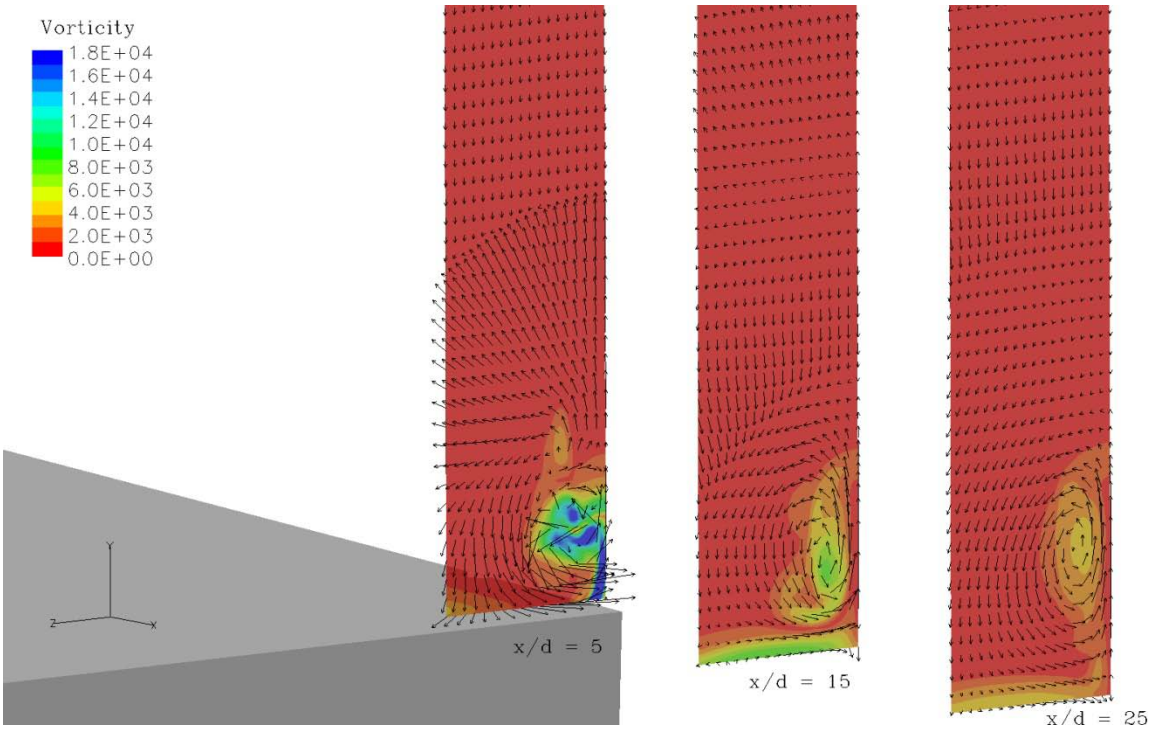

Figure 29. Vorticity contour/velocity vector plot for the baseline- no pylon test case.

Due to the similar flow structure of the fuel plumes found in the LWH-7x1/2x4, LWH-7x1x4, and LWH-7x2x4 pylons, the equivalence ratio plot with overlaid velocity vectors for the LWH-7x1x4 pylon is omitted here (all data can be seen in Appendix A). In Figure 30 the fuel plume associated with the LWH-7x1/2x4 pylon is shown and in Figure 31 the fuel plume from the LWH-7x2x4 pylon is displayed. For these similar fuel plume structures the highest concentration of fuel is seen in the lower half of the fuel plume at the x/d = 5 station. The two counter-rotating vortices can be seen at both the top and bottom of the fuel plume, while the lower set of vortices appears larger and more powerful. The upward momentum from the fuel injector port is visible by the set of strong vertical velocity vectors in the center of the fuel plume. This momentum drives the creation and sustainment of the counter-rotating vortices at the peak of the fuel plume while pulling the area of highly concentrated fuel higher into the plume structure. The

strong counter-rotating vortices at the base of the fuel plume are seen entraining air from the freestream into the fuel plume. The strength of the counter rotating vortices at the base of the fuel plume are shown to diminish markedly from the x/d= 5 location to the x/d =15 station.

Figures 32 and 33 illustrate the vorticity fields for the LWH-7x1/2x4 and LWH-7x2x4 pylons whose species contour plots were shown in the previous two figures. The general behavior that was seen in the vorticity plot for the baseline, no pylon, test case is also apparent in the LWH-7x1/2x4 and LWH-7x2x4 pylons. The baseline test case displays the same general magnitude of vorticity within the fuel plume area that is found in the pylon test cases, the presence of the pylons do not appreciable alter the streamwise vorticity in the fuel plume.

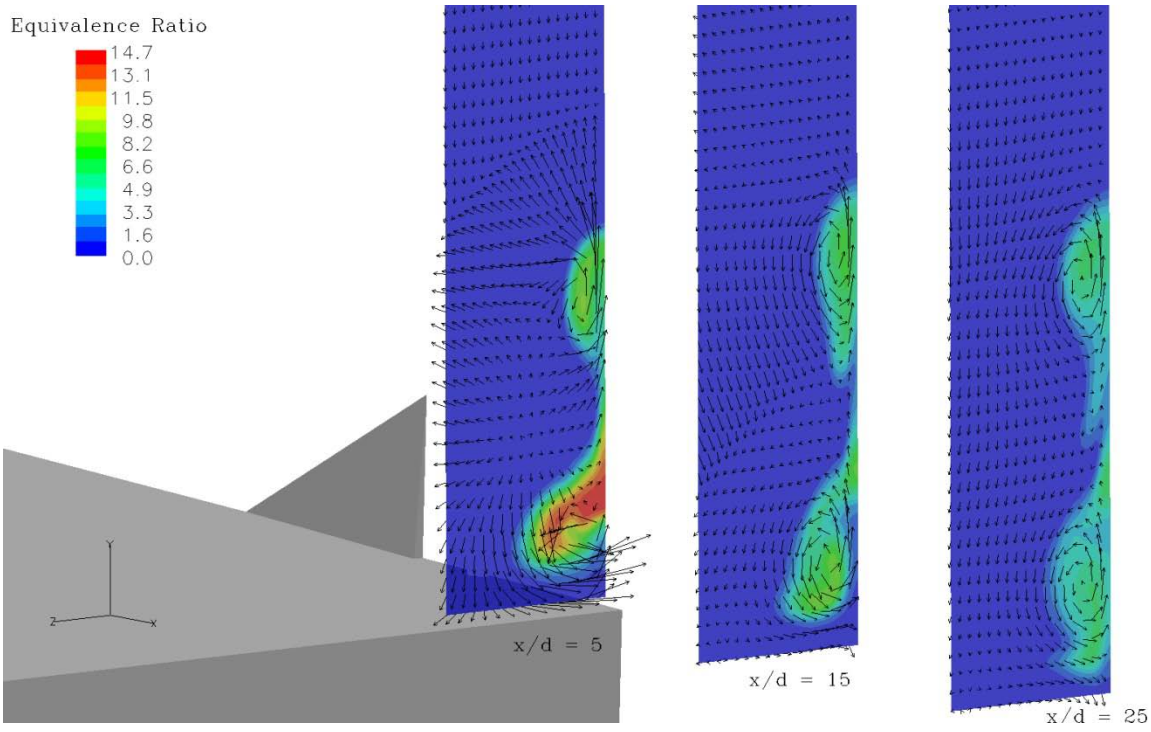

Figure 30. Equivalence ratio contour/velocity vector plot for the LWH-7x1/2x4 pylon.

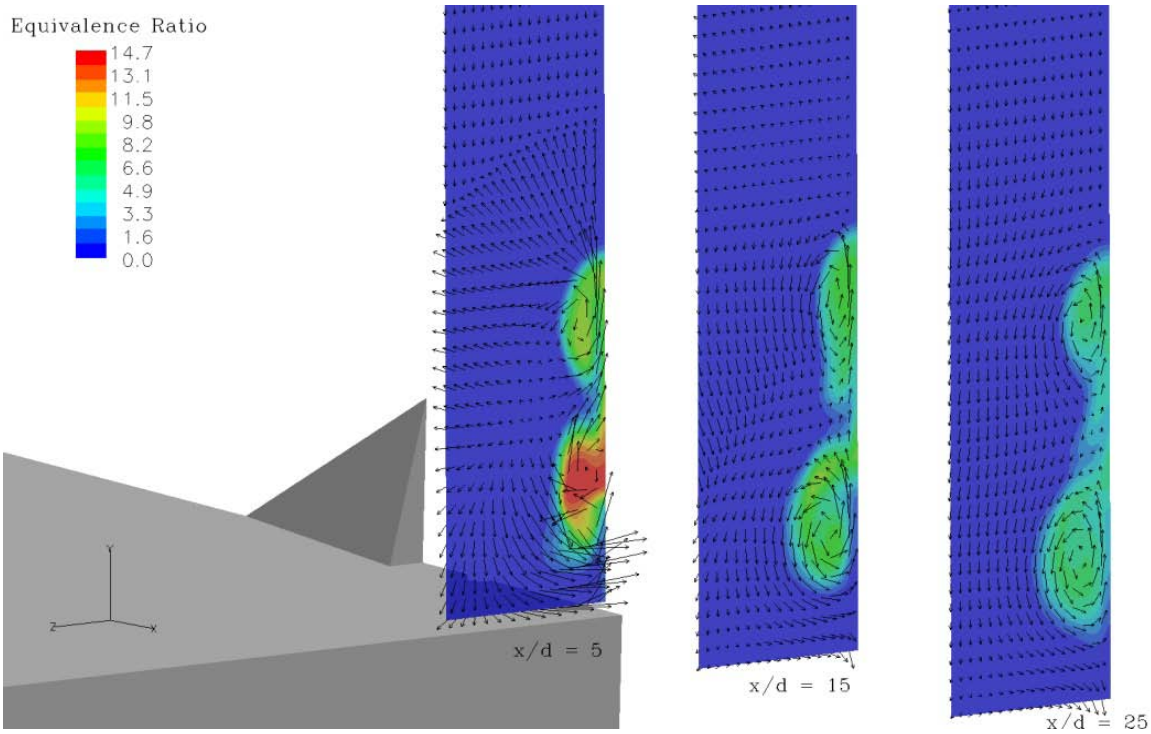

Figure 31. Equivalence ratio contour/velocity vector plot for the LWH-7x2x4 pylon.

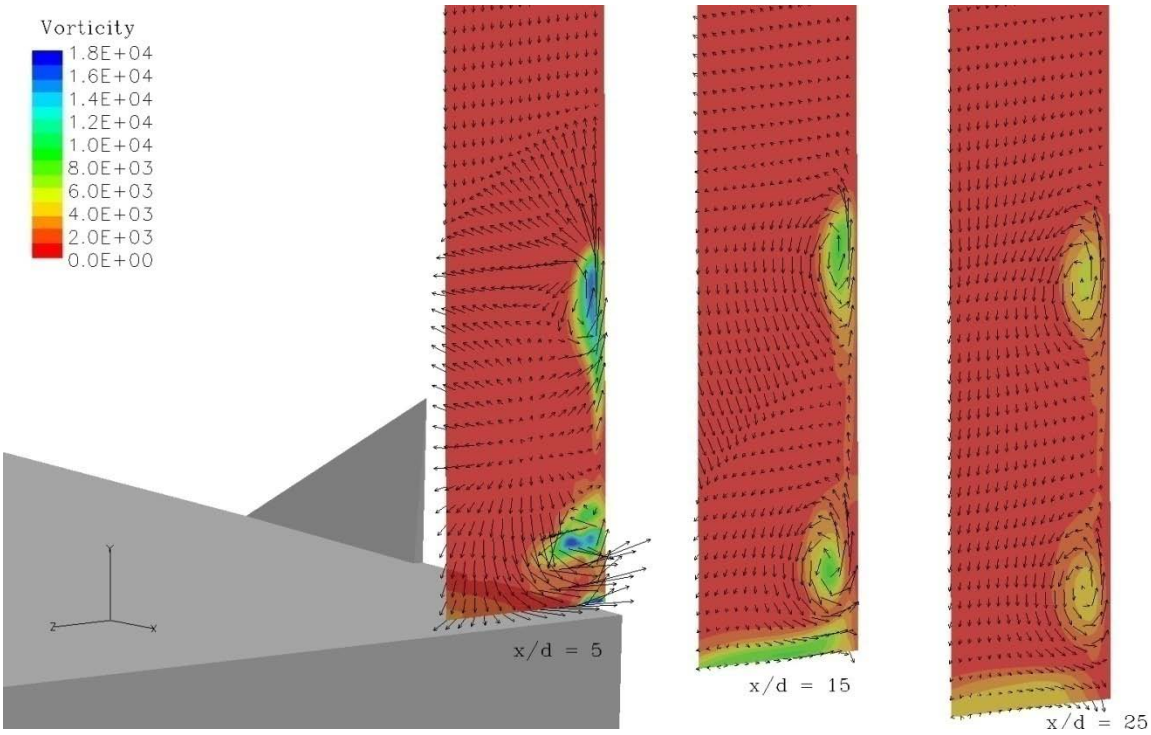

Figure 32. Vorticity contour/velocity vector overlay for LWH-7x1/2x4 pylon.

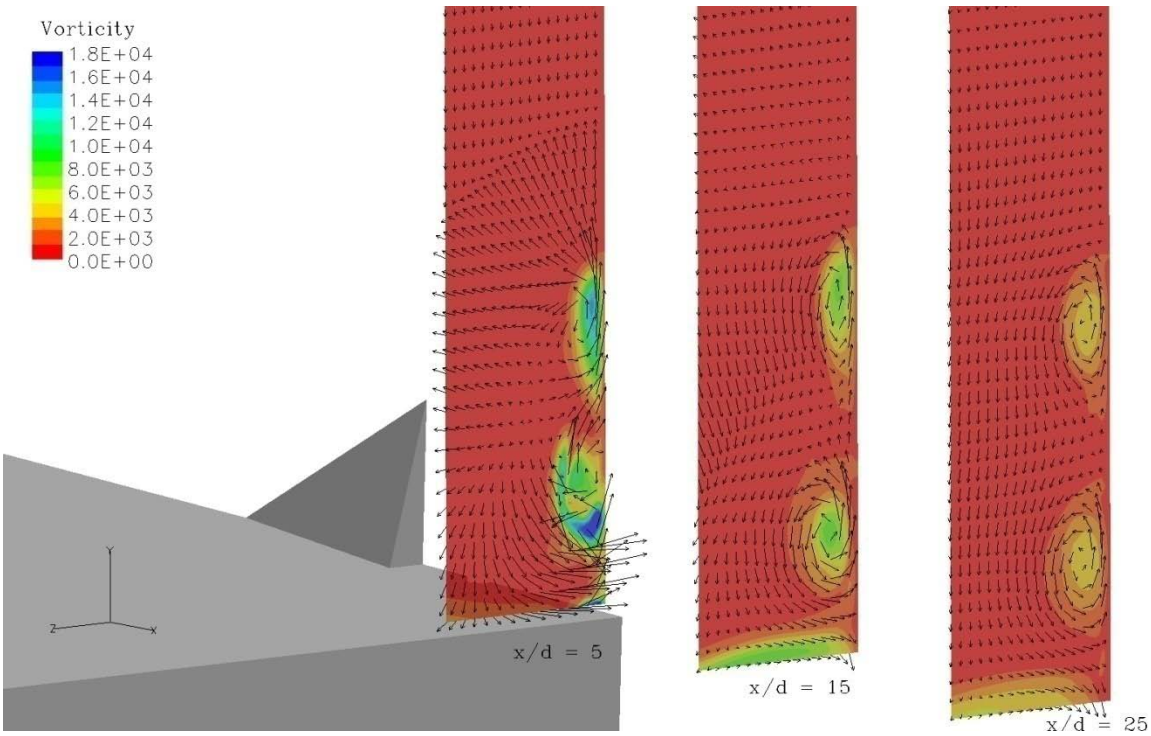

Figure 33. Vorticity contour/ velocity vector for the LWH-7x2x4 pylon.

The species contour-velocity vector plot of the LWH-7x3x4 pylon fuel plume, seen below in Figure 34, illustrates the merging of the upper and lower sets of counter-rotating vortices near the x/d = 25 location. This 3 diameter wide pylon shares some of the attributes of the narrow pylons and of the larger pylons. The LWH-7x4x4, LWH-7x5x4, and LWH-7x6x4 pylons are dominated by one single large vortex structure and will be referred to as the 'wide' pylons in further discussion.

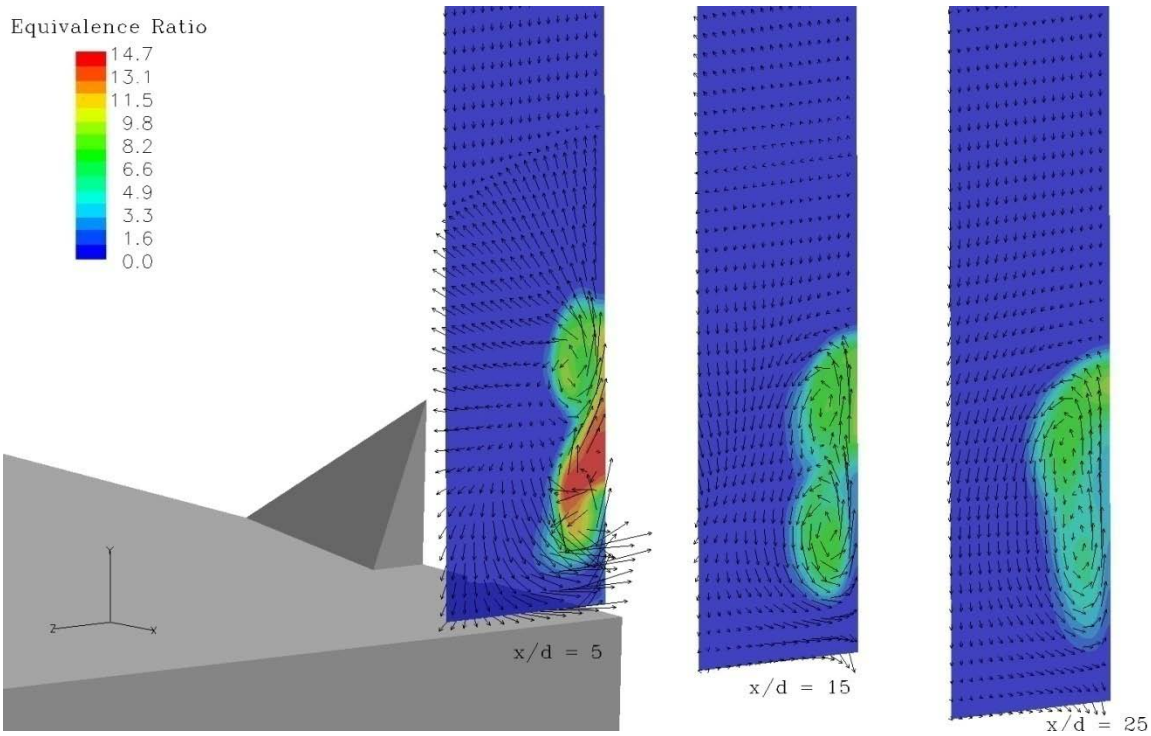

Figure 34. Equivalence ratio contour/velocity vector plot for the LWH-7x3x4 pylon.

In the species contour – velocity vector plots for the wide pylons the size of the vortices appears to increase as the pylon width is increased. In Figure 35 the fuel plume structure for the LWH-7x4x4 pylon initially demonstrates the two sets of vortices found in the narrow pylons. However, the set of counter-rotating vortices quickly merge and form one large single vortex. At the x/d =5 station two sets of counter-rotating vortices can be seen as in Figure 31 for theLWH-7x2x4 pylon. However, in this case, the upper and lower pair of vortices do not spread apart as seen in the narrow pylons, but merge together to form one large vortex by the x/d = 15 station. The merging of the vortices has a clear and negative impact on the maximum penetration of the fuel plume. Though penetration is minimal this pylon geometry still provides a noticeable amount of floor-gap. The vorticity contour plot of the LWH-7x4x4 pylon, seen in Figure 36, depicts the

flow structure of this wide pylon. Though the size of the counter-rotating vortices is larger, the magnitude of the vortices is similar to that seen in the narrow pylons.

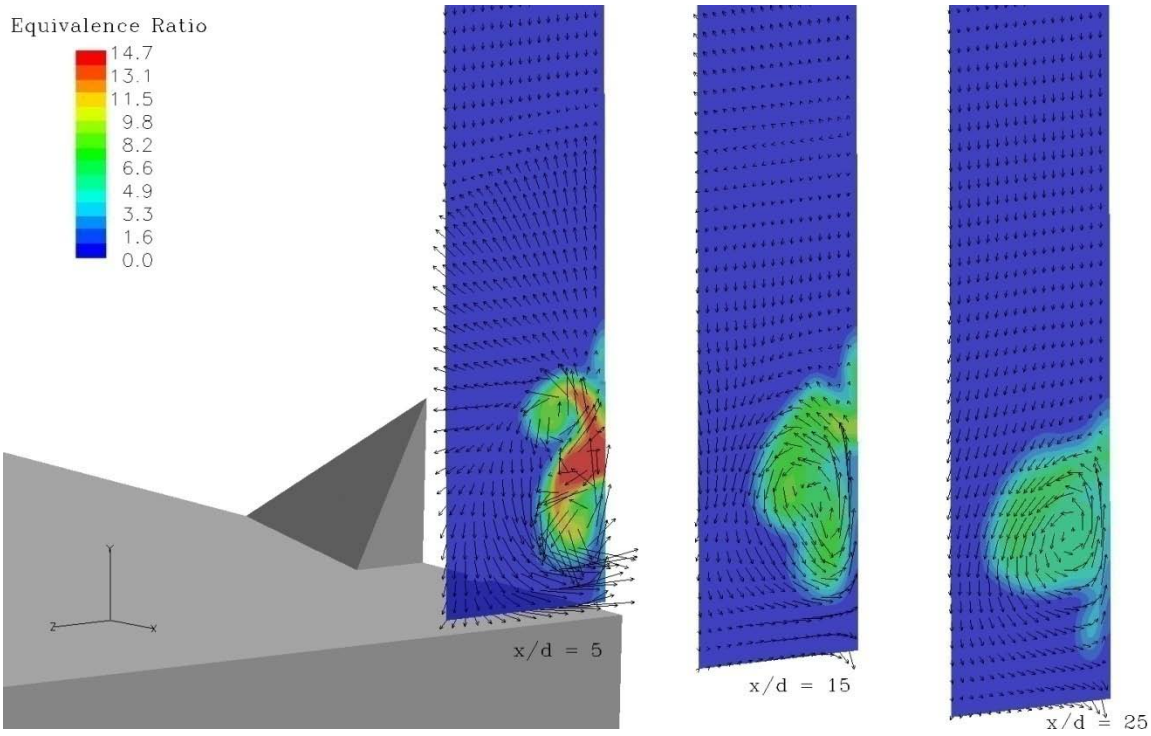

Figure 35. Equivalence ratio contour/velocity vector plot for the LWH-7x4x4 pylon.

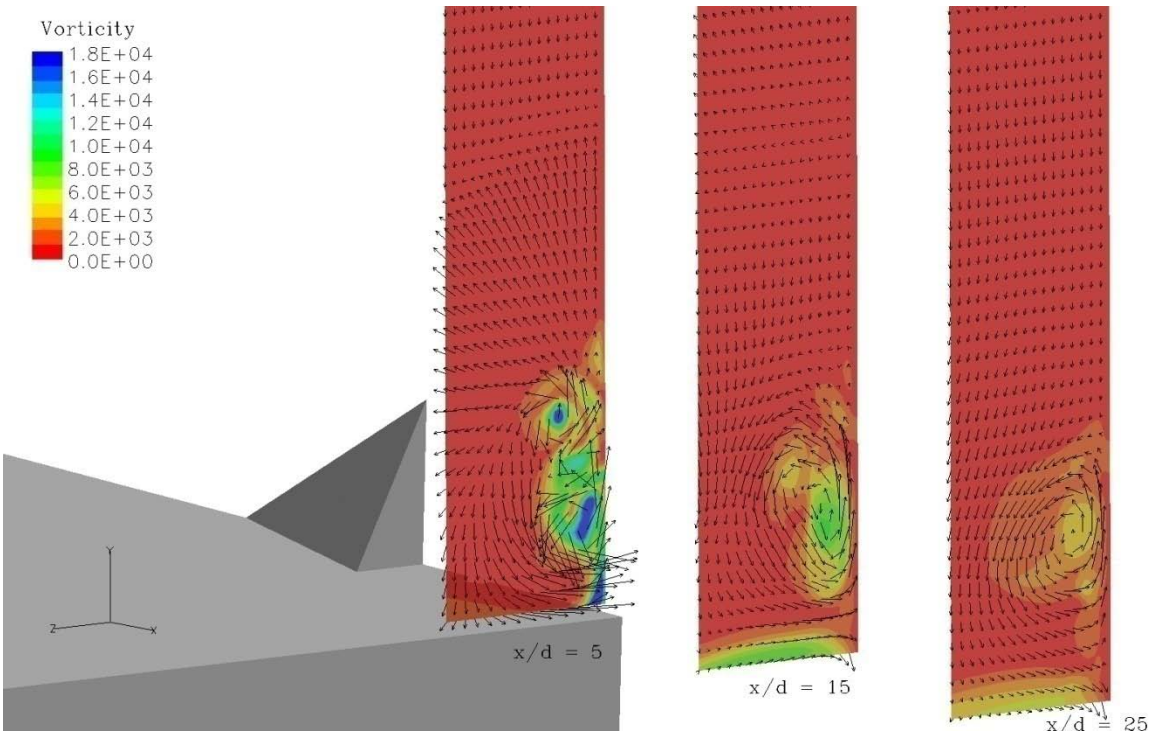

Figure 36. Vorticity contour/ velocity vector for the LWH-7x4x4 pylon.

In Figures 37 and 38, increasing the width of the pylons further to a 5 and 6 diameter wide configuration has minimal impact on the vorticity created by these pylons. The large vortices that form at the base of these wide pylons combine with the wide region of low pressure behind these pylons to limit the total penetration into the freestream. Though the size of the vortices varies significantly between the narrow and wide pylons the magnitude of these vortices is relatively constant. Visual inspection shows that the maximum vorticity occurs at the x/d = 5 location for all pylons, pulling clean freestream air into the lower portion of the fuel plume. The vorticity contour plot of the LWH-7x6x4 pylon shares similar behavior to the previous test cases even though the geometry is much more radical, as seen in Figure 39.

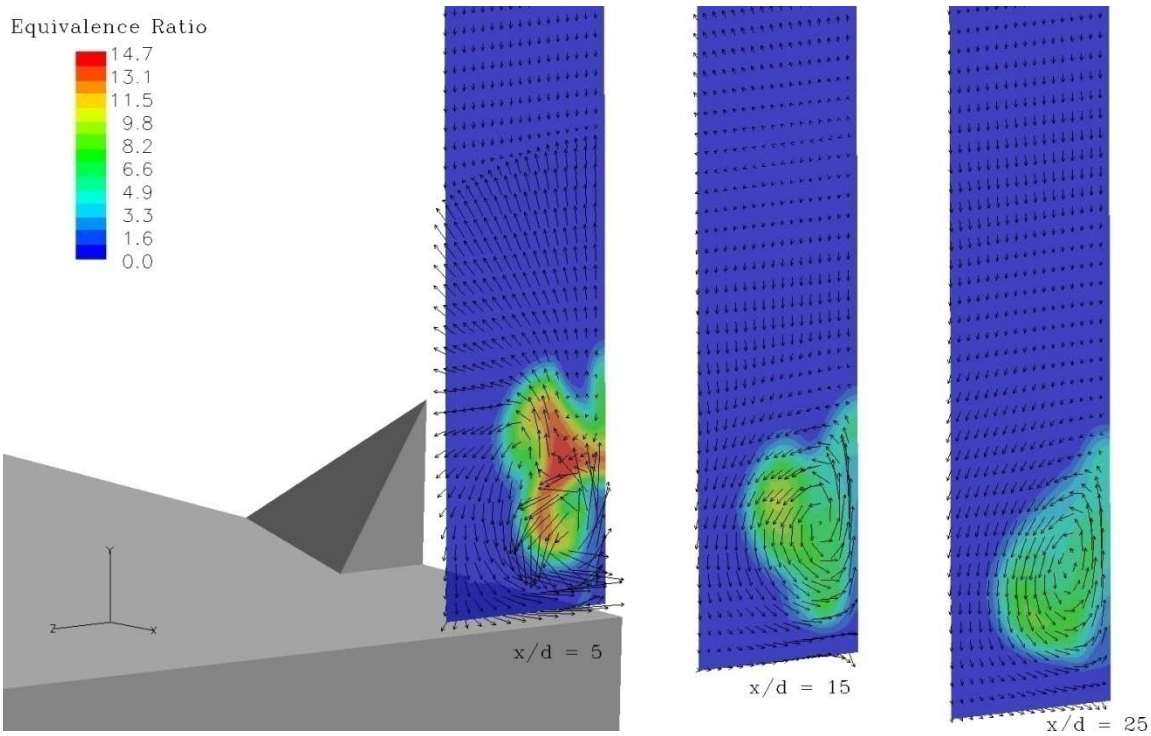

Figure 37. Equivalence ratio contour/velocity vector plot for the LWH-7x5x4 pylon

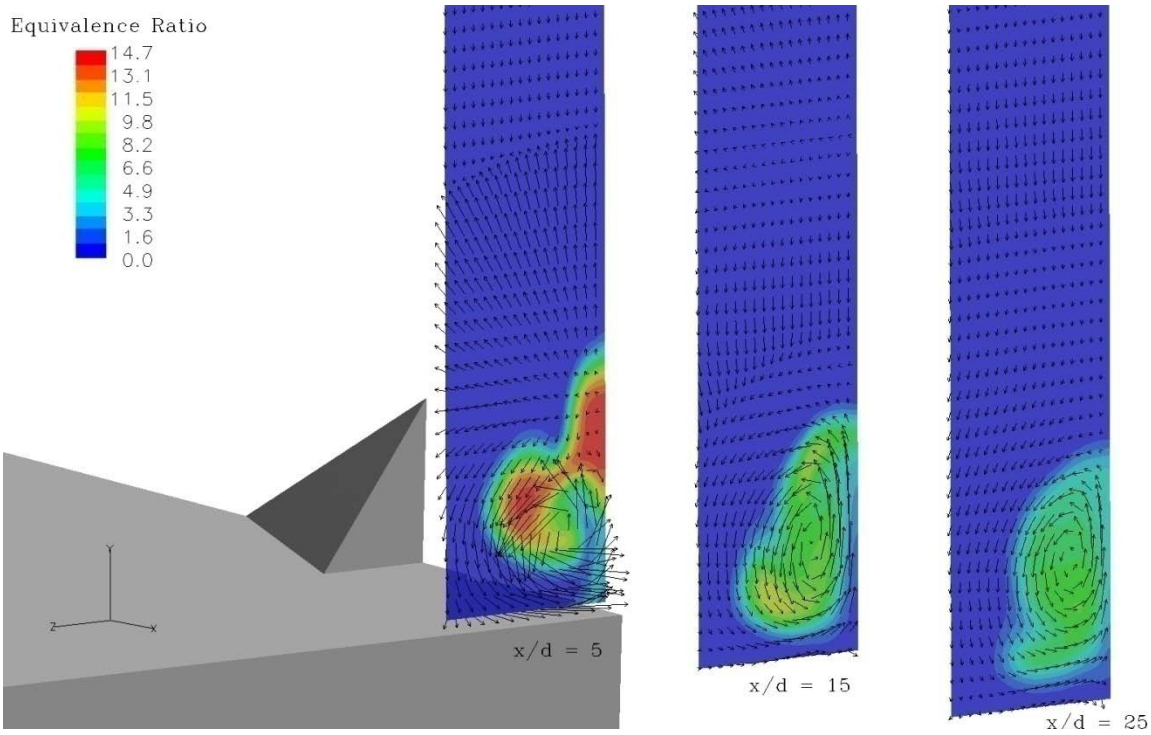

Figure 38. Equivalence ratio contour/velocity vector plot for the LWH-7x6x4 pylon.

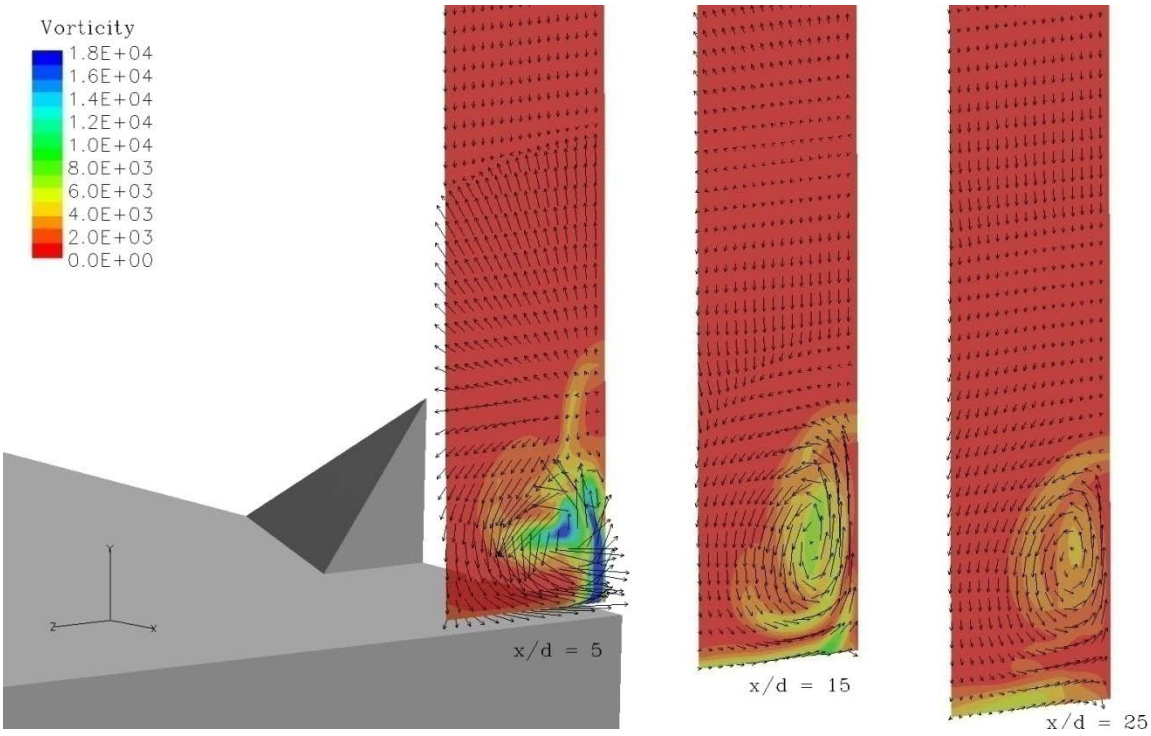

Figure 39. Vorticity contour/ velocity vector for the LWH-7x6x4 pylon.

Fuel Plume Distortion by the Flame-holding Cavity

The species contour plots for the first test matrix, seen in Figures 20 through 27, illustrate a shift in many of the fuel plume structures at approximately the x/d = 60 location. This upward shift, or increased penetration and distortion of fuel plume structure, was due to interaction of the fuel plume flow structure with vortices emanating from the flame-holding cavity. Figures 40 and 41 illustrate the interaction between the flow exiting the flame-holding cavity and the fuel plume structure. The strong counter-rotating vortices, seen in red, form a subsonic disturbance in the flow that forces the fuel plume to elevate further into the freestream, artificially increasing fuel plume penetration in the far downstream data reduction planes.

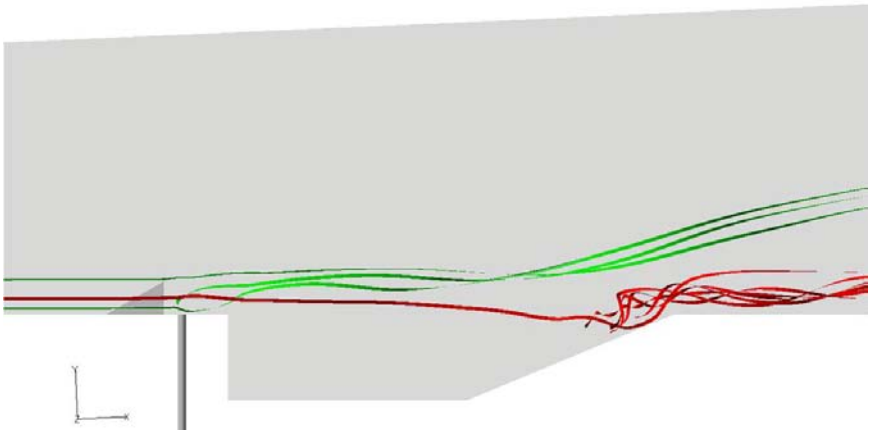

Figure 40. Side view of flow structure within the flame-holding cavity that distorts the fuel plume.

The contour/ vector insert in Figure 41 illustrate the relative strength of the counter-rotating vortices exiting the flame-holding cavity. These counter-rotating vortices aid in entraining clean unmixed air into the fuel plume, increasing both the flammable fuel plume area and total fuel plume area.

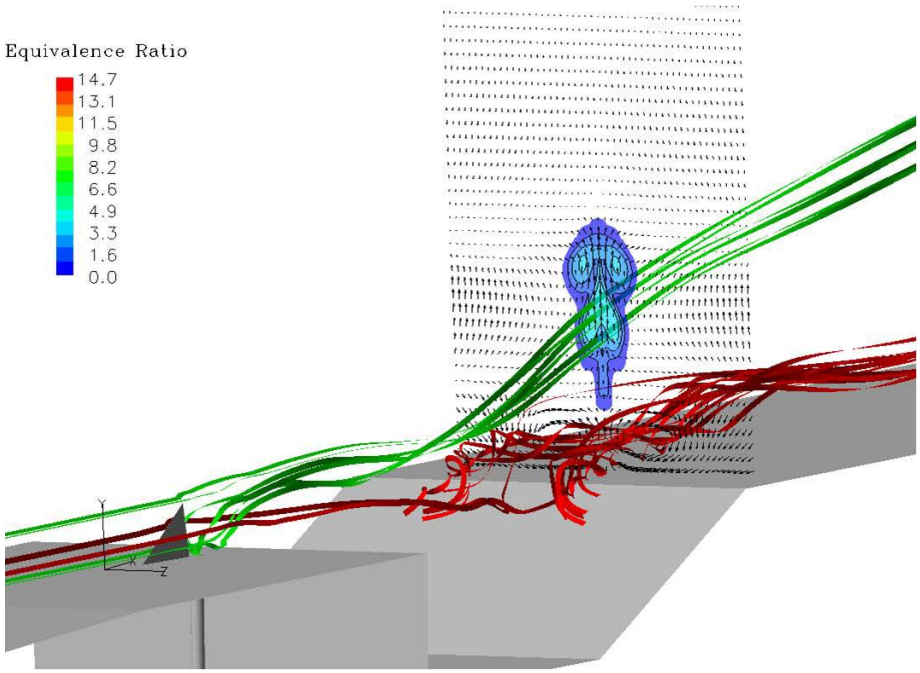

Figure 41. Iso-view of flow structure interaction between the flame-holding cavity and freestream including vector plot and contour plot at x/d = 60 location of LWH-7x1x4 pylon.

Mixing Efficiency

The mixing efficiency for each of the eight test cases from the first test matrix are presented in Figure 42. A side view of the pylon-injector-cavity arrangement is provided at the bottom of the figure providing relative geometry location. Here it can be seen that all of the pylon test cases had higher mixing efficiencies than the baseline test case. Both the narrow and wide sets of pylons displayed noticeably increased mixing efficiency over the baseline case. However the LWH-7x3x4 pylon performed relatively poorly in comparison to the rest of the pylons. The slope of the mixing efficiency curve increases slightly near the end of the flame-holding cavity. This effect is most likely due to the increased mixing via the interaction of the fuel plume with the subsonic, counter-rotating vortices exiting from the rear of the flame-holding cavity.

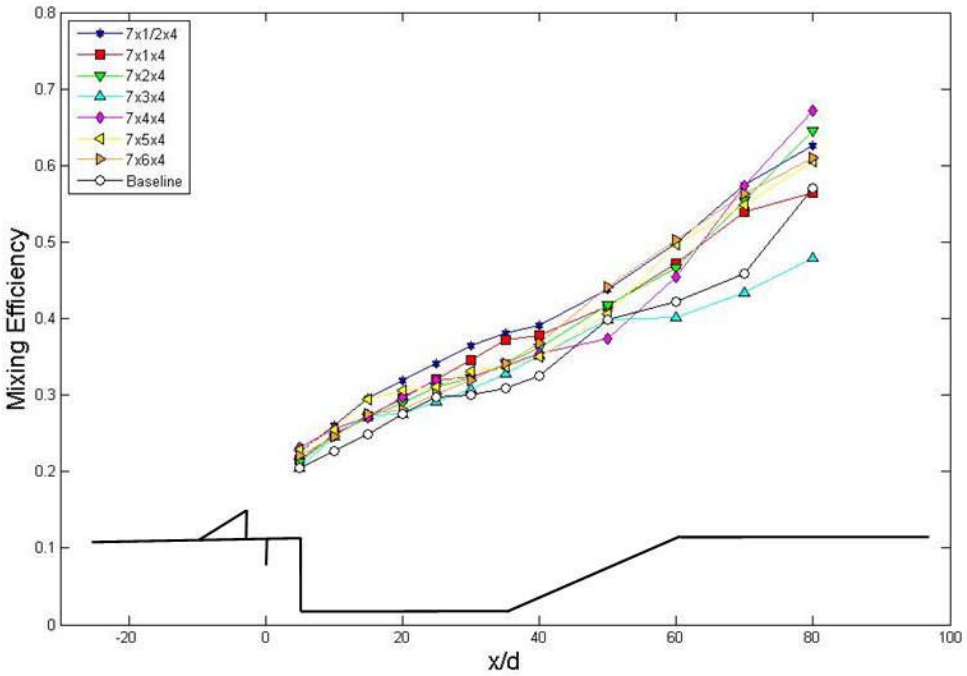

Figure 42. Mixing efficiency for the first test case matrix, representing pylons with differing widths.

Fuel Plume Area

The total fuel plume area for the pylons tested in the first test case can be seen below in Figure 43. Here it can be seen that the 5 and 6 diameter wide pylons generally create the largest fuel plumes through the x/d = 20 location. The LWH-7x1/2x4 pylon presents a plume area that is comparable in size to the LWH-7x5x4 pylon. This narrow pylon is supplanted midway through the cavity by the two large pylons. The plume areas for the rest of the pylons are grouped together and slightly larger than the baseline test case until the end of the flame-holding cavity. The outlying data point in the LWH-7x6x4 pylon, located at x/d = 40 location, is much larger due to the fact that fuel has been entrained in the flame-holding cavity. The lack of floor-gap, or separation, for the 6 diameter wide pylon that was seen in Figure 27 led to large amounts of the fuel plume to

reside below the fuel injector in the turbulent region of the flame-holding cavity. The LWH-7x6x4 pylon exhibits a considerably larger plume that continues to spread as the plume traverses down the test area. The elongation of the LWH-7x1/2x4 flume plume that was identified in Figure 21 by the spreading apart of the two sets of counter-rotating vortices rapidly increases the pylon's plume area. This effect is more pronounced than in the other narrow pylons. The increased size of the 4 -diameter wide pylon did not appreciably increase the plume area when compared to the narrow pylons.

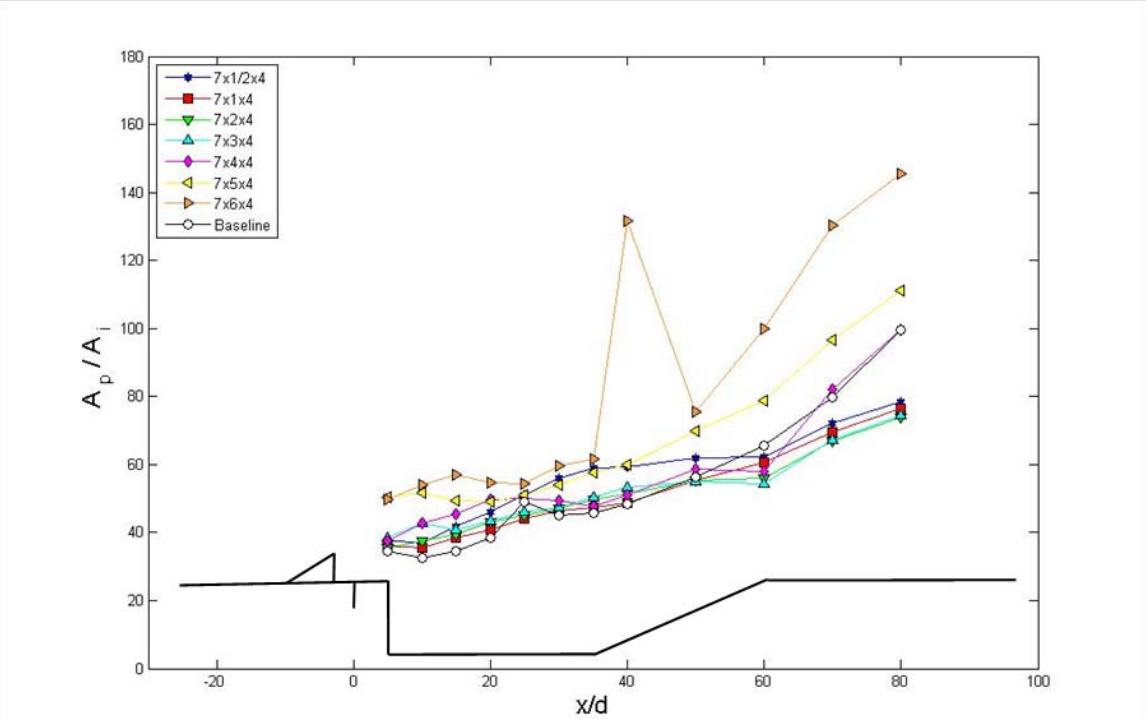

Figure 43. Total fuel plume area for the first test case matrix, representing pylons with differing widths

Flammable Fuel Plume Area & Flammable Mixture Distance

In Figure 43 two key metrics are shown that provide more insight into the effectiveness of the mixing. The flammable fuel plume area from each of the pylons is

presented along with the flammable mixture distance. With the pylon-injector-cavity assembly overlaid at the bottom portion of the figure, the relative position and differential of the flammable mixture distances can be easily seen. Here the 2 -diameter pylon has the shortest x_{fmd} followed by the 1 then 1/2 -diameter pylons. The 4 -diameter wide pylon's x_{fmd} is further downstream than the flammable mixture distance of the baseline test case, indicating a relatively low degree of fuel-air mixing.

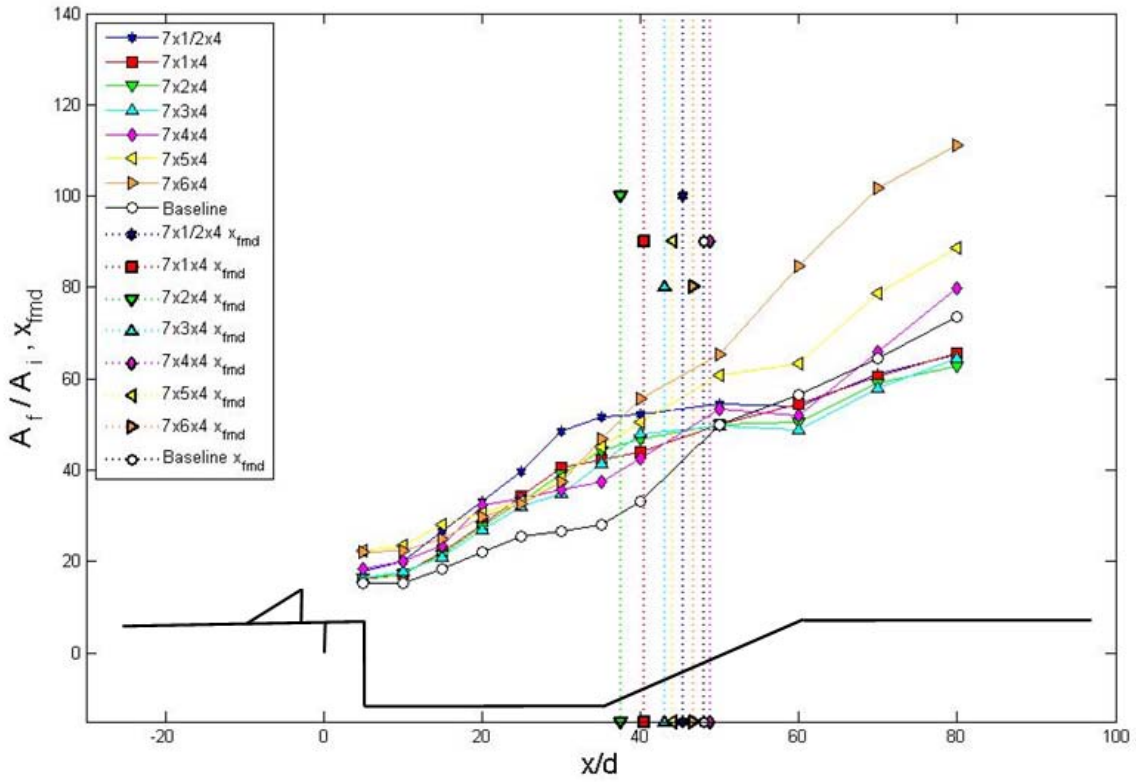

Figure 44. Flammable fuel plume area and flammable mixture distance for the first test case matrix, representing pylons with differing widths.

The larger flammable fuel plumes of the 5 and 6 diameter wide pylons at the upstream data reduction planes is surpassed by the LWH-7x1/2x4 pylon at the x/d = 30 location. This narrow pylon continues to rapidly increase its A_f until the x/d = 40

location where the flammable fuel plume area plateaus and stays relatively constant. The other two pylons from the narrow group present similar behavior as the 1/2 -diameter width pylon albeit on a slightly smaller scale. The flammable plume areas of the wide pylons continue to spread as downstream distance increases with all ultimately providing larger plume area than seen in the narrow pylons. The 6 -diameter wide pylon providing almost twice the flammable plume area at station x/d = 80 as the narrow pylons. The baseline test case, with a fuel plume structure comparable to the wide pylons behaved similarly to the wide pylons. The baseline test case presented initially the smallest A_f. When the narrow pylons flammable fuel plume area began to plateau at the rear end of the flame-holding cavity, the baseline test case's A_f exceeded that of the narrow pylons.

Flammable Fuel Plume Percentage

Figure 45 presents the flammable plume percentage for pylons in the first test matrix. The narrow pylons again share similar behavior and trends as all three pylons increase, plateau, and then decay at similar locations and rates. The wide pylons fuel plumes have a markedly lower FPP than the narrow pylons across nearly all stations. Here in Figure 45 the outlaying point from the 6 -diameter pylon is the result of the large total fuel plume area found within the flame-holding cavity at the at the x/d = 40 location that in turn drastically reduces the FPP. The baseline test case FPP behavior is similar to the wide pylons, though it generally has the lowest flammable fuel plume percentage of across the flame-holding cavity. Though the 6 -diameter wide pylon has a low FPP across the test area, the pylon has a much larger total plume area and flammable plume area than the other pylons. The 6- diameter wide pylon's low FPP is not indicative of a

poorly performing pylon. The flammable fuel plume percentage metric is a more accurate indicator of mixing ability when comparing fuel plumes of similar total plume area. The FPP value is seen when trying to determine the proper location to ignite the fuel plume, this is typically done at the location of highest flammable fuel plume percentage.

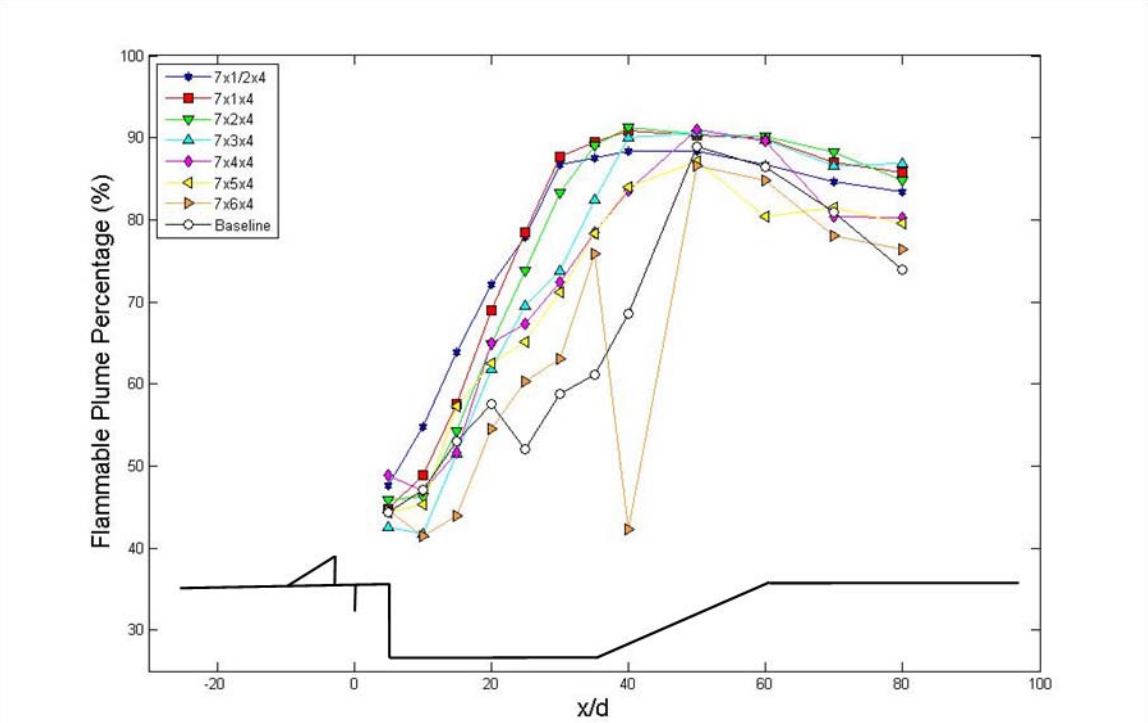

Figure 45. Flammable Fuel Plume Percentage for the first test case matrix, representing pylons with differing widths.

Maximum Equivalence Ratio

The magnitude and location of the maximum equivalence ratio within the fuel plume provide additional information on effectiveness of the fuel injection strategy. Figure 46 depicts the decay of maximum equivalence ratio as a function of downstream distance. All test cases display very similar exponential rates of Φ_{max} decay. The

penetration of Φ_{max} into the freestream is seen in Figure 47. In this figure the wide pylons depict reduced penetration into the freestream as compared to the baseline case. These pylons are dominated by a single large vortex pair. The dual set of counter-rotating vortices in the fuel plume structure of the narrow pylons often leads to drastic changes in the core penetration height. This dramatic shift in core penetration is due to the fact that the highest percentage of fuel concentration is found slightly above the lower set of vortices or entrained in the upper set of counter-rotating vortices in these narrow fuel plumes. The narrow pylons have the ability to carry higher concentrations of fuel deeper into the freestream.

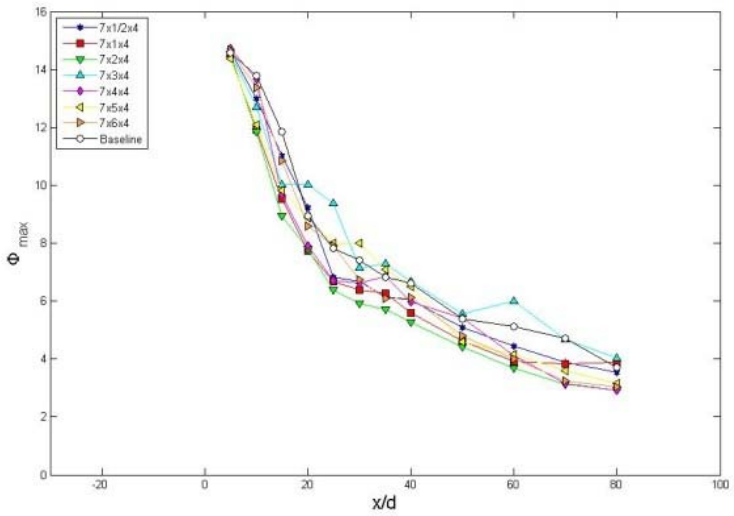

Figure 46. Decay of maximum equivalence ratio for the first test case matrix, representing pylons with differing widths.

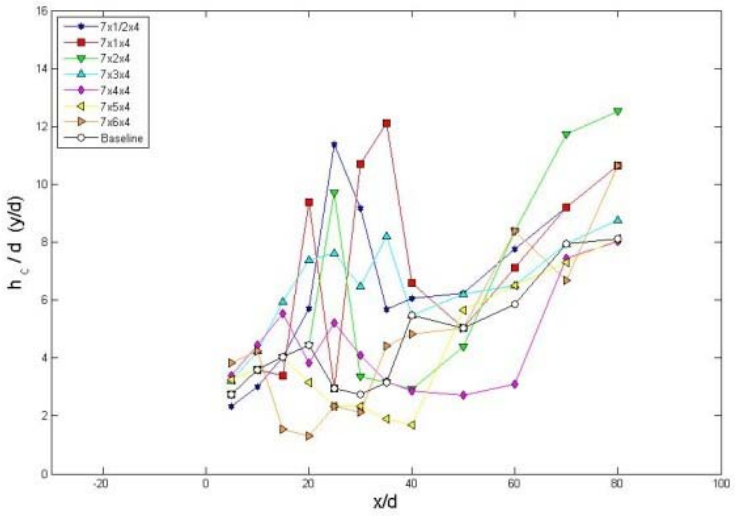

Figure 47. Penetration of location of maximum equivalence ratio for the first test case matrix, representing pylons with differing widths.

Total Penetration

Plume penetration for test matrix 1is shown in Figure 48. The total penetration of the fuel plume into the freestream reveals the stark contrast between the narrow and wide pylons. The LWH-7x1/2x4 pylon initially demonstrates the best penetration into the freestream. Near the x/d = 45 streamwise location the 1 –diameter wide pylon begins to penetrate farther into the freestream than the 1/2 –diameter wide pylon. As width is increased in the narrow pylons total penetration is reduced. The wide pylons initially demonstrate greater penetration than the baseline case. However, midway across the flame-holding cavity, near the x/d = 40 location, the penetration of the baseline case and the wide pylons is essentially equal. Note all pylons shown below have a total height of 4 –diameters.

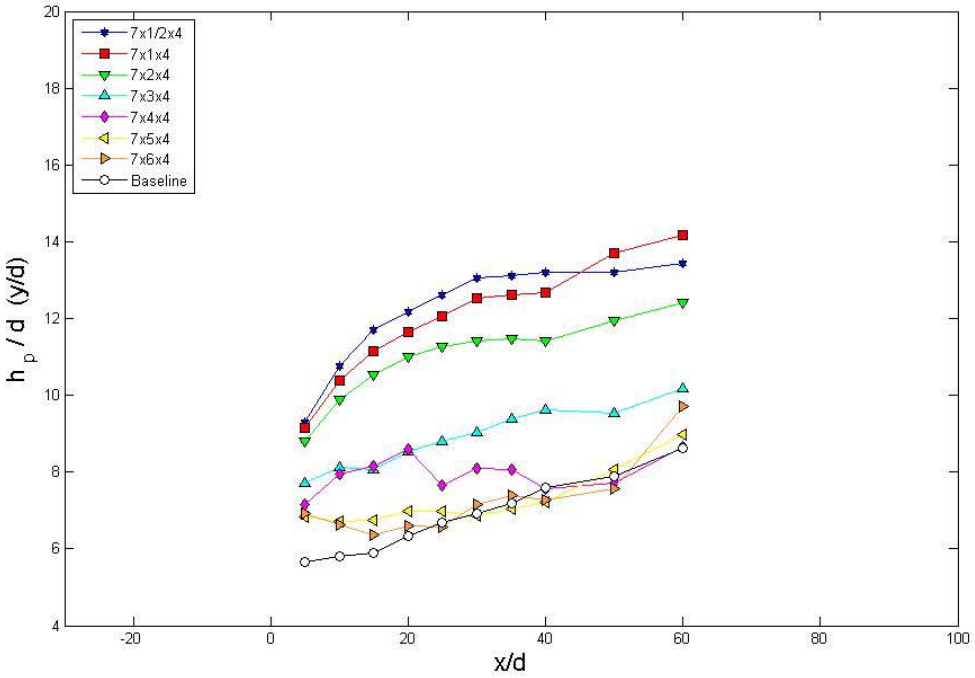

Figure 48. Total fuel plume penetration for the first test case matrix, representing pylons with differing widths.

Total Pressure Loss

The total pressure loss coefficients for the pylons in the first test matrix are shown below in Figure 49. Past research into the use of pylon-aided normal fuel injection[1, 2, 3, 5, 18] has shown that the use of pylons may actually decrease pressure losses when compared to normal fuel injection and has suggested that the pylon's width should be limited to 1-2 diameters wide to reduce aerodynamic losses. The baseline case below is seen to suffer the highest losses across the flame-holding cavity. The baseline case increased losses stem from the stronger normal shock that is found upstream of the fuel injector port. The pylons suffer lower losses due to the weaker bow shock that is created by the pylons.

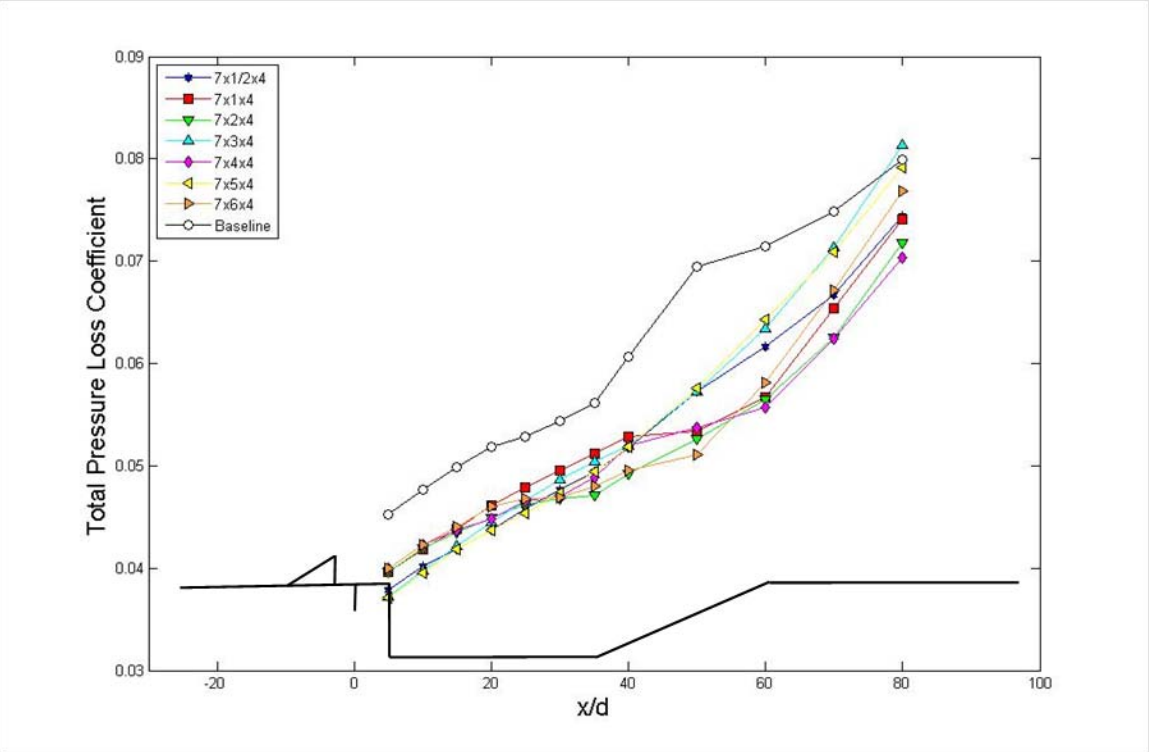

Figure 49. Total pressure loss coefficient for the first test case matrix, representing pylons with differing widths.

The conventional wisdom that the pylons must be on the order of 1-2 diameters wide to minimize pressure losses did not bear out in this study. In fact there was no direct correlation between pylon size and pressure loss. The smallest pylon tested, the LWH-7x1/2x4 (1/2 diameter wide) pylon presented higher losses than the largest pylon tested (6 diameters wide) at the end of the flame-holding cavity. Pressure losses also did not correlate to fuel plume size or penetration. At the x/d= 80 location the 3 diameter wide pylon presents the most pressure loss even though the LWH-7x3x4 pylon produces the smallest fuel plume at that location. Similarly at the x/d = 60 data reduction plane the 1/2 diameter wide pylon suffers lower losses than the 5 diameter wide pylon even though the 1/2 diameter wide pylon penetrates much further into the freestream. At the far upstream data reduction plane the baseline case shows losses approximately 20% greater

than the best pylon case, this increases to about 28% at the x/d = 60 location. It was not until the data reduction planes past the flame-holding cavity in the divergent ramp that a pylon geometry presented higher losses than the baseline test case.

Narrow Pylon Comparison

Taking a closer look at the critical fuel-air mixing metrics of the narrow pylons as well as the fuel species contour plots in Figures 20 through 32 allows for several general trends to be identified. Mixing efficiency, flammable fuel plume area, flammable mixture distance, total plume penetration and pressure losses are critical fuel-air mixing metrics. In Figure 50, seen below, these metrics are presented for the narrow pylons (LWH-7x1/2x4, LWH-7x1x4, and LWH-7x2x4) as well as for the LWH-7x3x4 pylon that shares many characteristics with the narrow pylons. Starting with the LWH-7x1/2x4 pylon; increasing the pylon width has the following effects:

- Maximum Penetration is Reduced
- The lower set of counter-rotating vortices migrates deeper into the freestream, decreasing the distance between the two sets of counter-rotating vortices
- Increased Floor-gap is Achieved
- Flammable Fuel Plume Area is Decreased
- Flammable Mixture Distance is Decreased

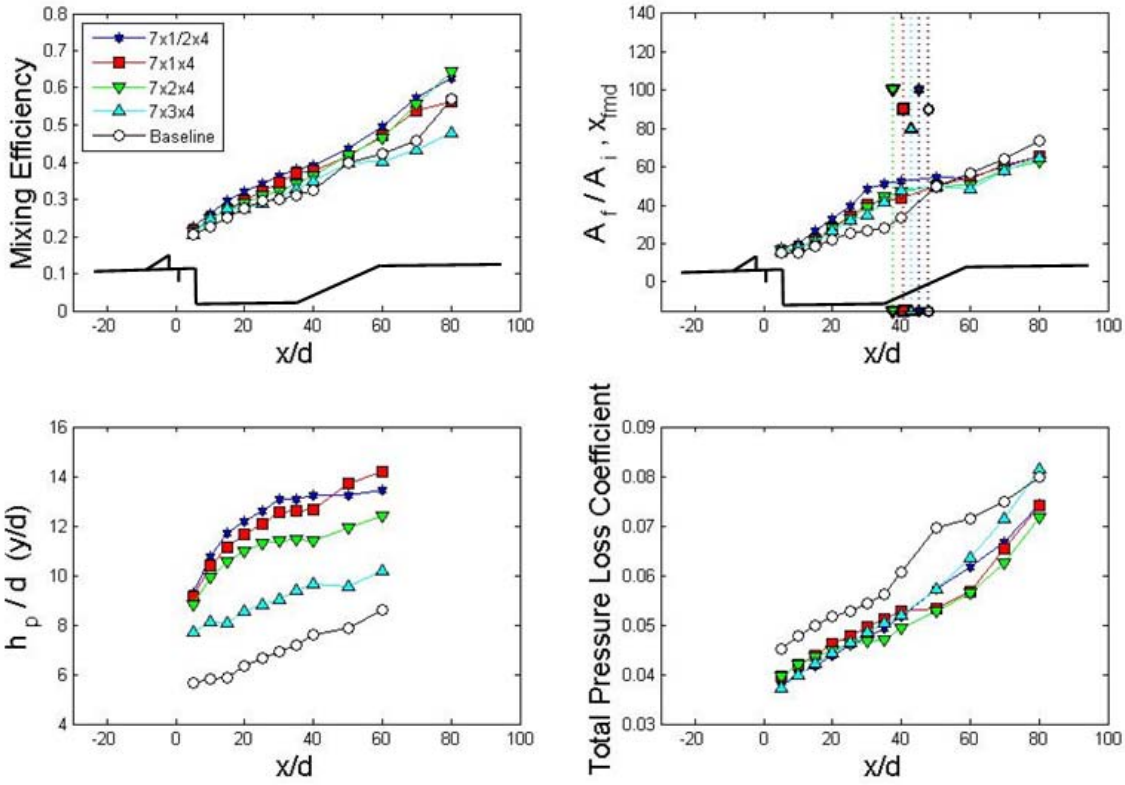

Figure 50. Critical fuel-air mixing metrics for the narrow pylons.

Wide Pylon Comparison

The fuel-air mixing metrics and species contour plots also allow for general trends to be identified for the wide pylons that are dominated by the singular large set of counter-rotating vortices. Below in Figure 51 the critical mixing metrics for the wide pylons are given. Included is the data for the baseline test case as well to provide some perspective to narrow pylons and overlays of the pylon-injector-cavity geometry. The scale of each of metrics on Figures 50 and 51 are consistent as well.

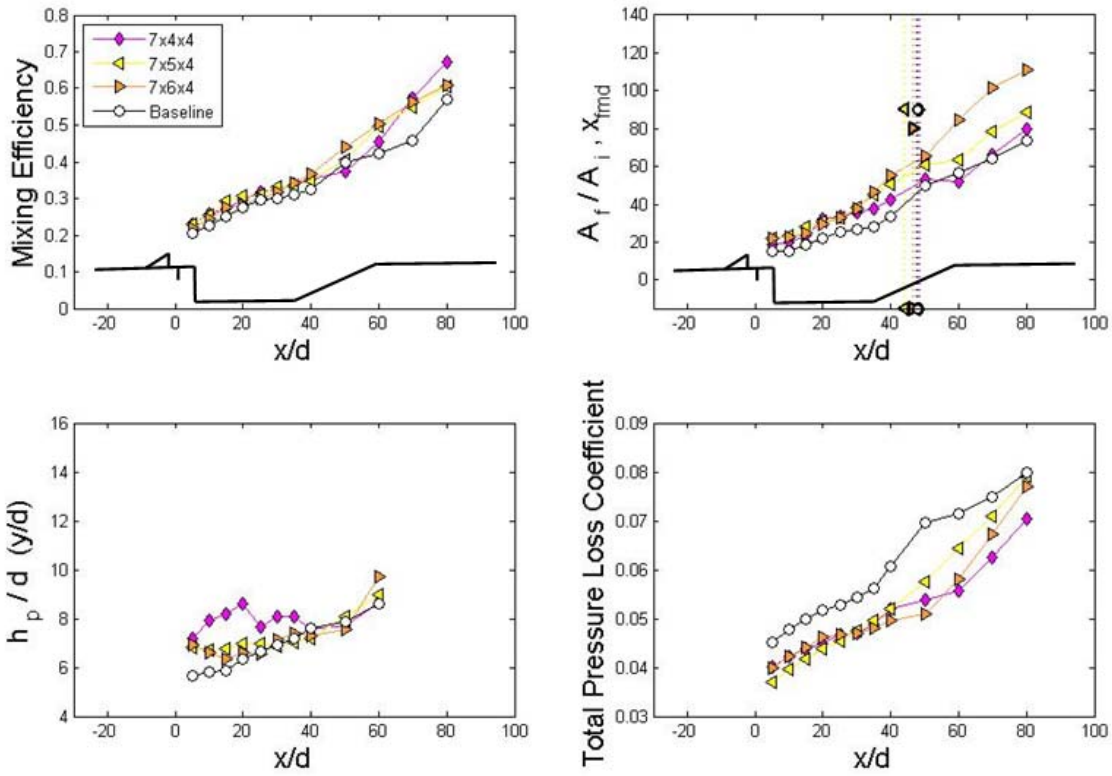

Figure 51. Critical fuel-air mixing metrics for the wide pylons.

With the mixing metrics presented above in Figure 51, the species contour plots seen in Figures 33 to 39 can be utilized to identify a few general trends associated with the wide pylons. Flammable mixture distance remains relatively unchanged when increasing the pylon width and pressure losses do not correlate with the pylon size. Starting with the 4 diameter wide pylon (LWH-7x4x4) increasing the pylon width has the following effects

- Decreased Penetration
- Decreased Floor-gap
- Increased Flammable Fuel Plume Area

4.3 Mixing Analysis Test Matrix 2- Pylon Height Variation Part I

Species Contour Plots

The second test matrix is part of the investigation into the effect of increasing the absolute height of one of the pylons from initial test matrix. These simulations maintained the leading edge wedge angle and height to width (h/w) ratio of the LWH-7x1x4 pylon and increased the absolute pylon height from 4 diameters to 8 diameters tall. Once again the fuel injection parameters are fixed for all test cases. Figures 52 through 56 present the species contour plots for the five variations in absolute pylon height for the LWH-7x1x4 pylon.

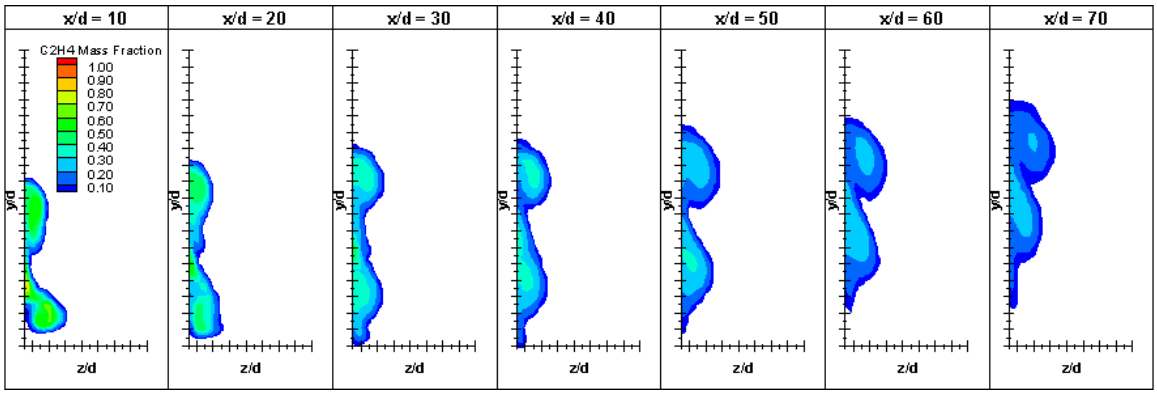

Figure 52. LWH-7x1x4 fuel species contour plot of C_2H_4.

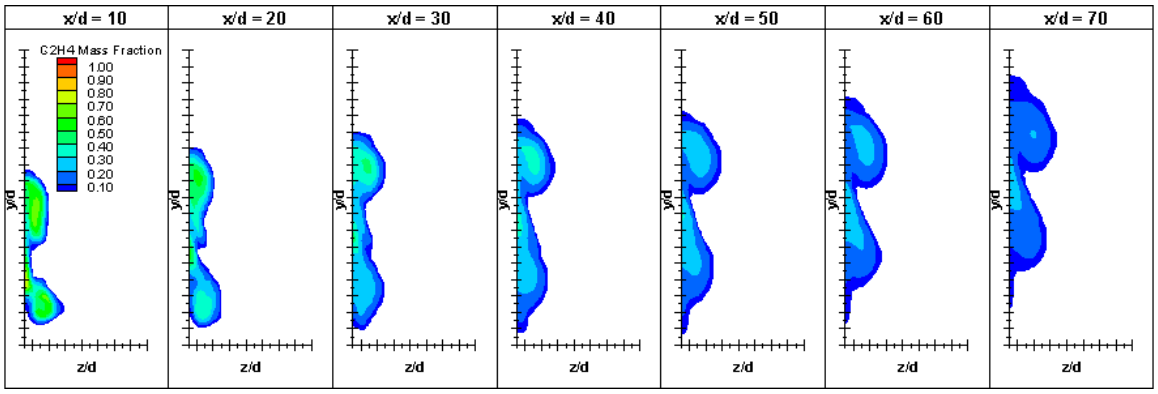

Figure 53. LWH-7x1x4-5h fuel species contour plot of C_2H_4.

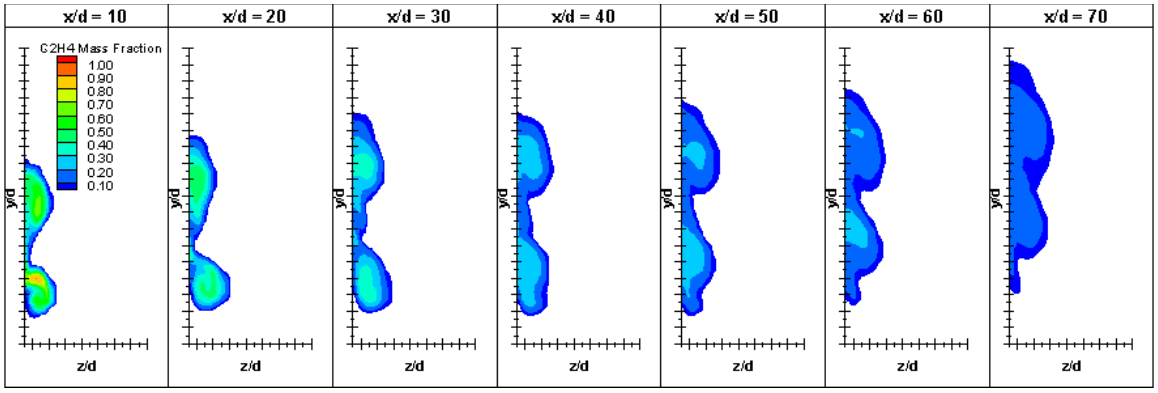

Figure 54. LWH-7x1x4-6h fuel species contour plot of C_2H_4.

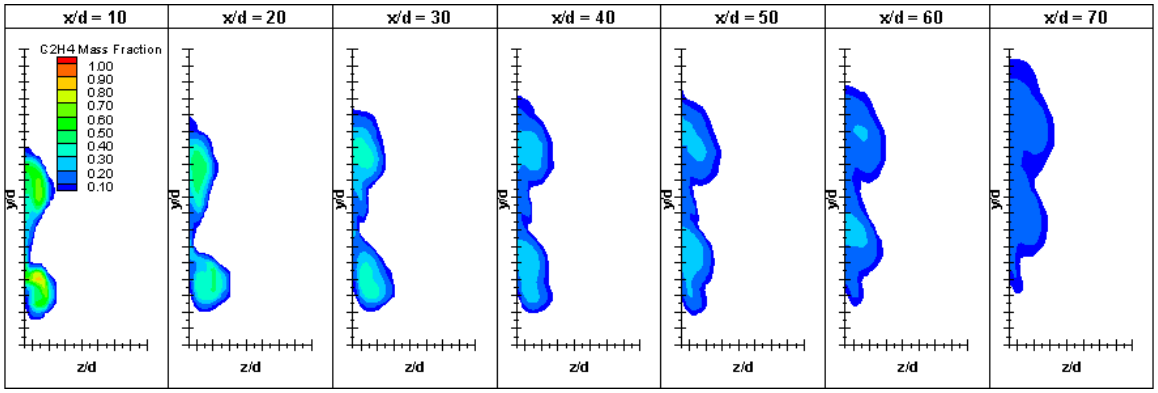

Figure 55. LWH-7x1x4-7h fuel species contour plot of C_2H_4.

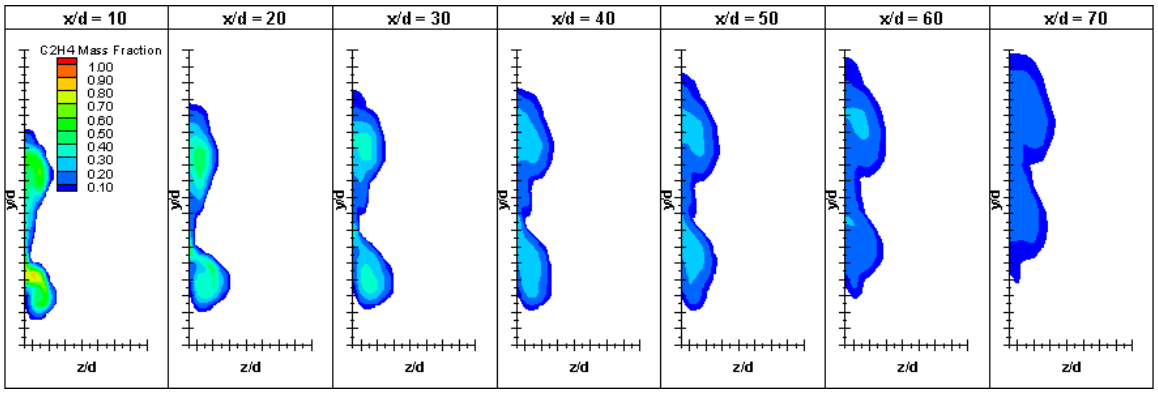

Figure 56. LWH-7x1x4-8h fuel species contour plot of C_2H_4.

Increasing the height by scaling the entire pylon up has several effects on the fuel plume structure. The fuel plumes maintain the dual set of counter-rotating vortices at both the top and bottom of the plume that is seen in the 4 –diameter tall pylon. The first incremental size increase to the 5-diameter tall pylon decreases the size of the lower set of counter-rotating pylons. However, all further modifications to the pylon size led to changes in position of the vortices and not to their overall size. The fuel plume elongates as the pylon height is increased, with both sets of vortices penetrating higher into the freestream. Looking at the plume structure of the 4, 6, and 8 diameter tall pylons in Figures 57 through 59 illustrates the migration of the vortices higher into the freestream as the pylon height is increased. The species contour plots with the velocity vector overlay for the 5 and 7-diameter tall pylons can be seen in Appendix A.

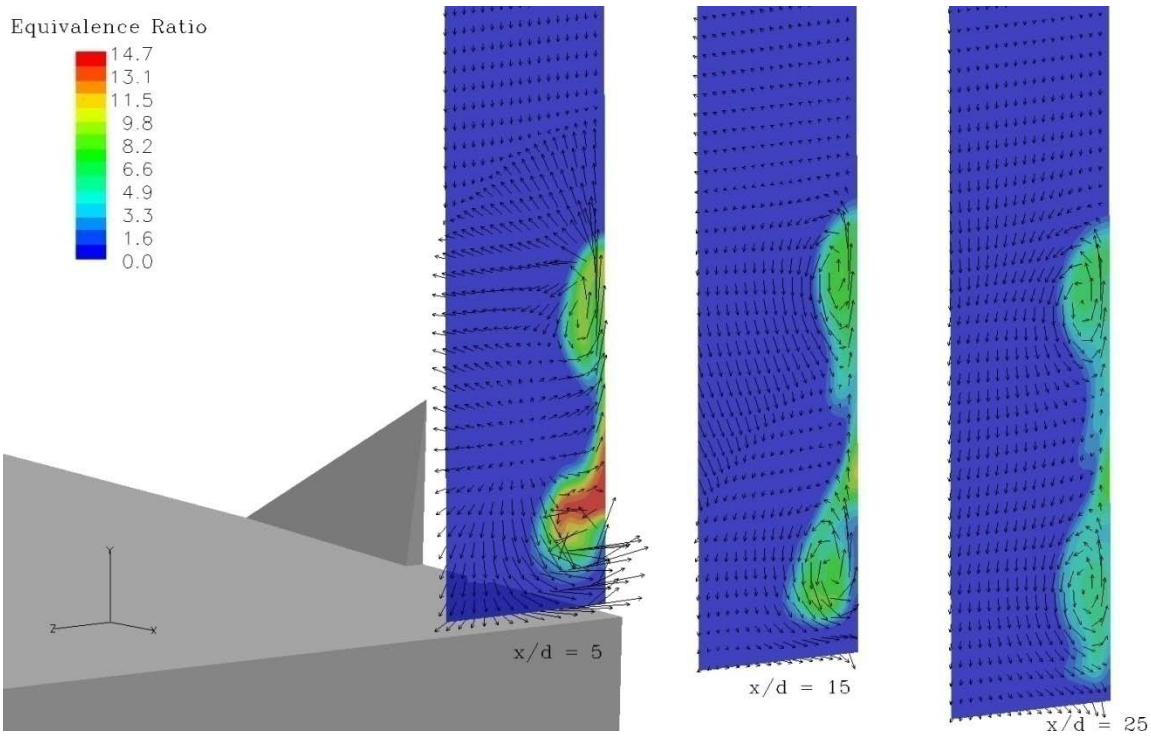

Figure 57. Equivalence ratio contour/velocity vector plot for the LWH-7x1x4-4h pylon.

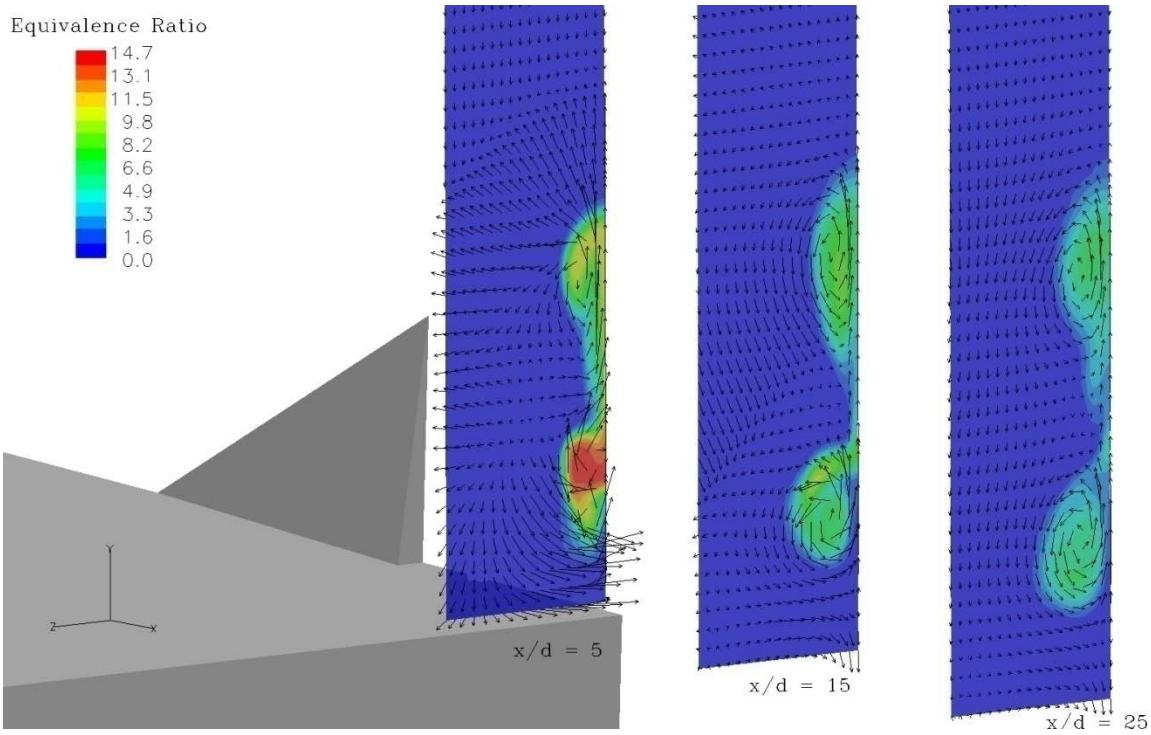

Figure 58. Equivalence ratio contour/velocity vector plot for the LWH-7x1x4-6h pylon.

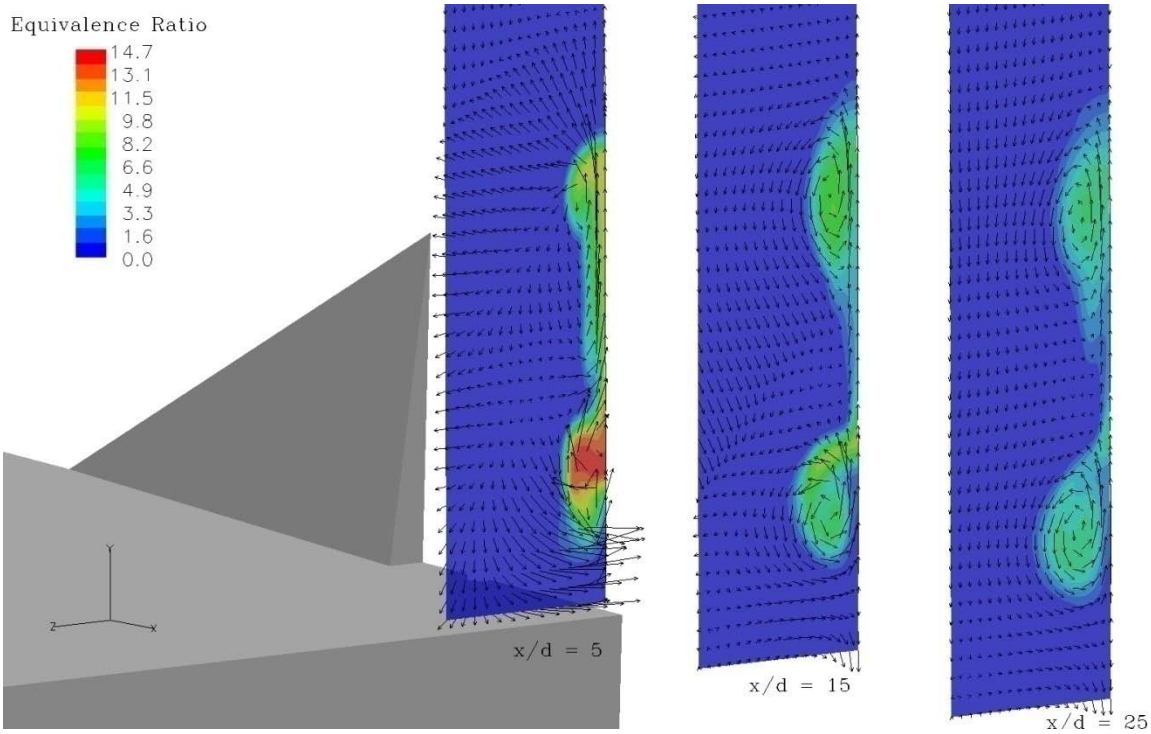

Figure 59. Equivalence ratio contour/velocity vector plot for the LWH-7x1x4-8h pylon.

Fuel-Air Mixing Metrics

The key metrics of fuel plume area, flammable fuel plume area, flammable mixture distance, total penetration, and pressure loss will be used to evaluate the effect of increasing the size of the pylons for the second test matrix. Figures of the mixing efficiency, flammable fuel plume percentage, decay of maximum equivalence ratio, and core penetration for the variations in pylon height for the LWH-7x1x4 pylon can be found in Appendix A. In Figure 60 the total fuel plume area is presented for the five variations in absolute pylon height for the LWH-7x1x4 pylon. The scale of the figures for the second, third, and fourth test matrix are identical to that of the first test matrix. The increase in pylon size has a consistent impact on fuel plume area, with each incremental increase in pylon height producing an analogous increase in fuel plume area.

The tallest pylon (8-diameters tall) ultimately created a fuel plume area 33% larger than the original 4 diameter tall pylon.

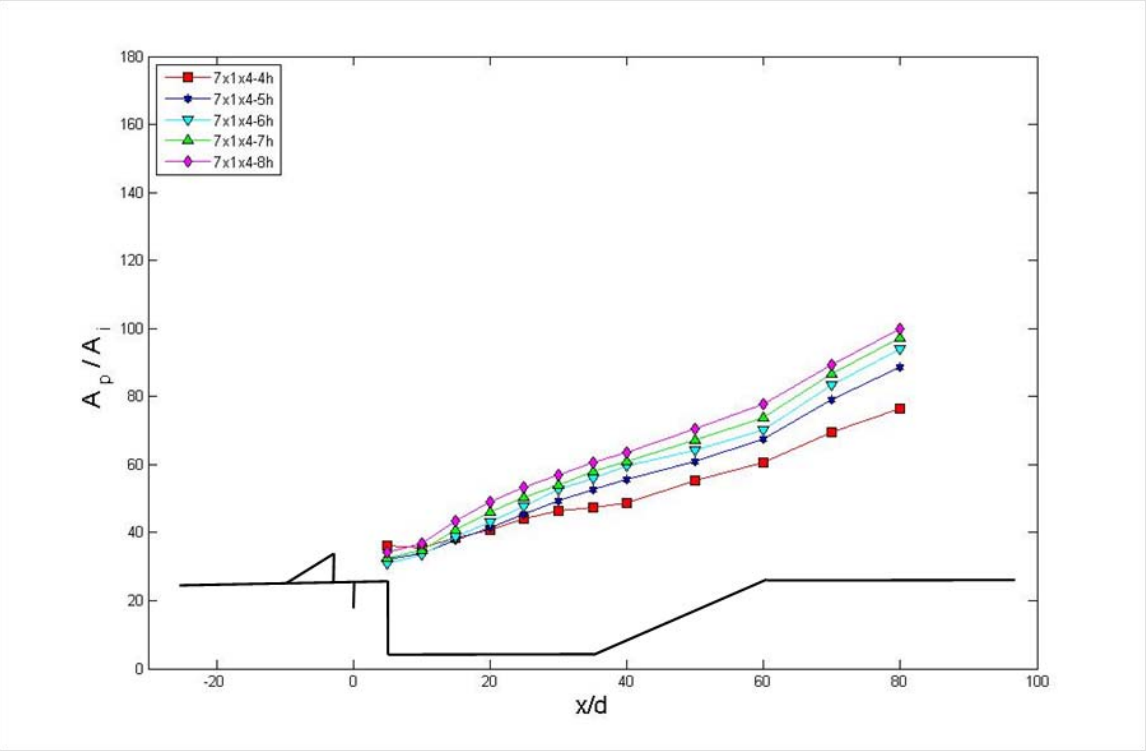

Figure 60. Total fuel plume area for the second test case matrix, representing variation in absolute pylon height for the LWH-7x1x4 pylon.

The flammable fuel plume area and flammable mixture distance for the variations in pylon height of the LWH-7x1x4 pylon can be seen in Figure 61. Increasing the pylon height has a regular impact and positive impact on the flammable fuel plume area. Here the 8 diameter tall pylon produces a flammable fuel plume area approximately 30% larger than the 4 diameter tall pylon. All pylons presented similar behavior in the spreading of the flammable fuel plume area. These pylons A_f values exponentially grow from injection to the x/d = 30 location. The plume then linearly increases in size to the

x/d =60 plane, where all pylons then begin a steeper increase in flammable fuel plume area.

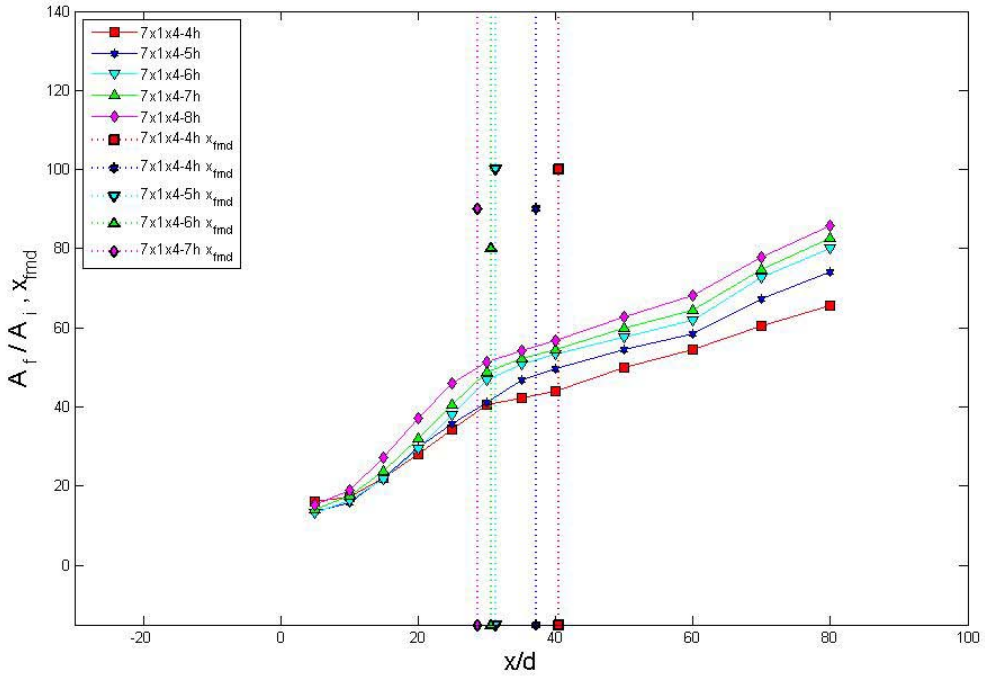

Figure 61. Total flammable fuel plume area for the second test case matrix, representing variation in absolute pylon height for the LWH-7x1x4 pylon.

The flammable mixture distance decreased with each increase in pylon height. This positive trend means that the fuel plumes have reached the minimum requirements for combustion quicker as the pylon height is increased.

Total fuel plume penetration into the freestream can be seen in Figure 62. Here again the increase in pylon height has a marked and consistent positive impact on this key metric. The 8-diameter tall pylon exhibits approximately 30% increase in total penetration over the original 4 diameter tall pylon and a 110% increase of the baseline-no pylon test case seen in the first test matrix. Generally, every incremental increase in pylon height by 1 diameter yeilds approximately a 1 diameter increase in total pylon

penetration into the freestream. The general behavior of the plume penetration is consistent for each of the variations in pylon height as well. The plumes are seen to increase in a general 3rd order fashion.

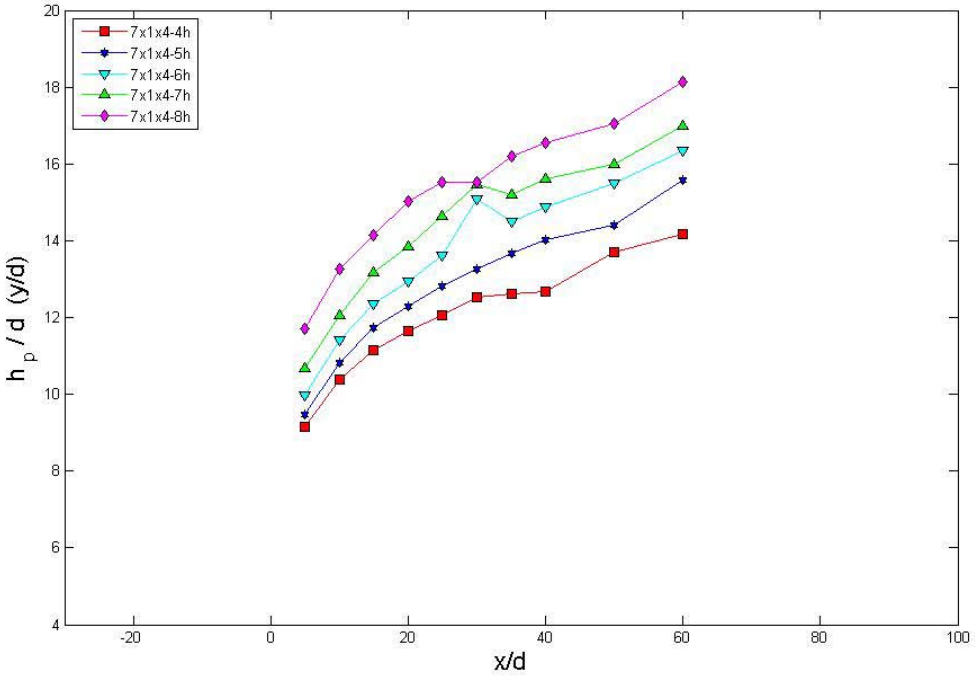

Figure 62. Total fuel plume penetration for the second test case matrix, representing variation in absolute pylon height for the LWH-7x1x4 pylon.

The aerodynamic losses for this test matrix are seen in Figure 63. This figure shows virtually no drastic variation in the losses associates with the 5, 6, 7, or 8 – diameter tall pylons. The original LWH-7x1x4-4h pylon displays notably different behavior than the other four pylons in this test section. The LWH-7x1x4-4h pylon initially exhibits higher pressure losses, but undergoes a minor delay in pressure loss halfway across the flame-holding cavity, and then increases considerably over the rear face of the cavity. The first test matrix with pure variations in pylon width found no direct correlation between pressure loss and any other fuel-air mixing metric. From

injection through the x/d = 40 location close inspection shows that the largest pylon displays slightly higher losses than the rest of the pylons. Each smaller pylon exhibited slightly lower losses than the larger pylon tested before it. The pressure loss curves collapse for all pylons at the x/c = 50 location. The cause for this unexpected variation is not certain. All pylons meet the same convergence criteria, however the modified pylons (the -5h, -6h, -7h, and -8h) took many more iterations to meet the convergence criteria. It would appear that the modified pylons would represent a more accurate flow solution.

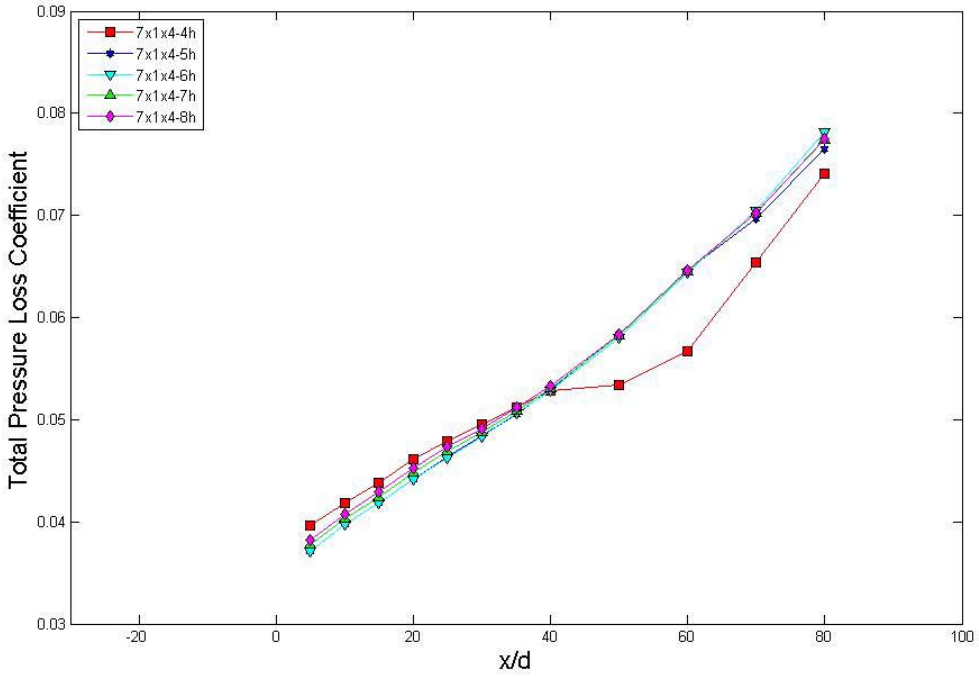

Figure 63. Total pressure loss coefficient for the second test case matrix, representing variation in absolute pylon height for the LWH-7x1x4 pylon.

LWH-7x1x4 Variation in Pylon Height Summary

Increasing the scale of the LWH-7x1x4 pylon to heights of 5, 6, 7, and 8 diameters tall produced favorable impacts on the key fuel-air mixing metrics. These modified pylons maintained the same 29.7° leading edge wedge angle and width to height ratio of 0.25 as the LWH-7x1x4 pylon. Beginning with the unmodified LWH-7x1x4 pylon, increasing the absolute size of the pylon :

- Increased Floor-gap
    - The lower set of vortices penetrates higher into the freestream
- Increased Penetration
    - The upper set of vortices
- Increased Flammable Fuel Plume Area
- Decreased Flammable Mixture Distance
- Minimal Impact on Pressure Loss

4.4 Mixing Analysis Test Matrix 3- Pylon Height Variation Part II

Species Contour Plots

The third test matrix seeks to validate the general conclusions from the second test matrix where the scale of a pylon was increased to identify the impact of taller pylons. The LWH-7x2x4 pylon was chosen for the third test matrix since this pylon was also part of the narrow fuel plume structures that were identified in the initial test matrix. Once again these simulations maintained the leading edge wedge angle and height to width (h/w) ratio of the LWH-7x2x4 pylon and increased the absolute pylon height to 5, 6, 7, and 8 diameters tall. Figures 64 through 56 present the species contour plots for the five variations in absolute pylon height for the LWH-7x2x4 pylon.

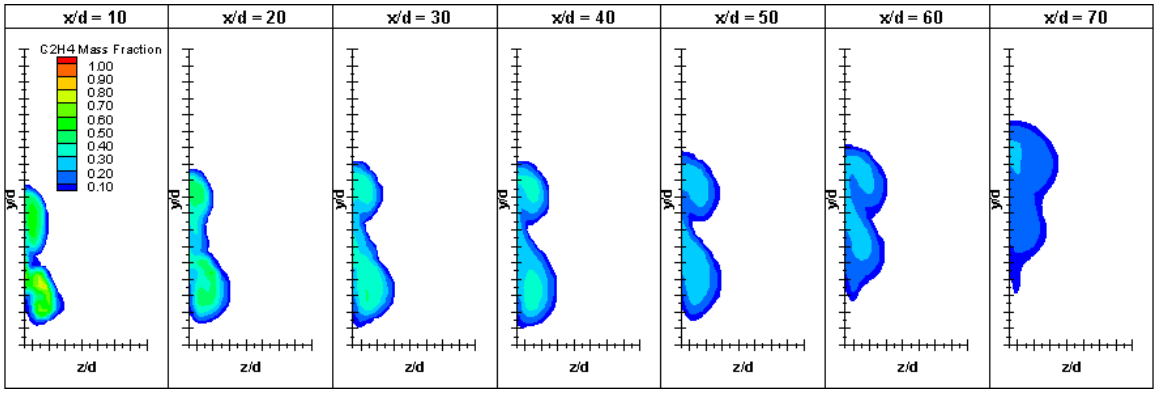

Figure 64. LWH-7x2x4-4h fuel species contour plot of C_2H_4.

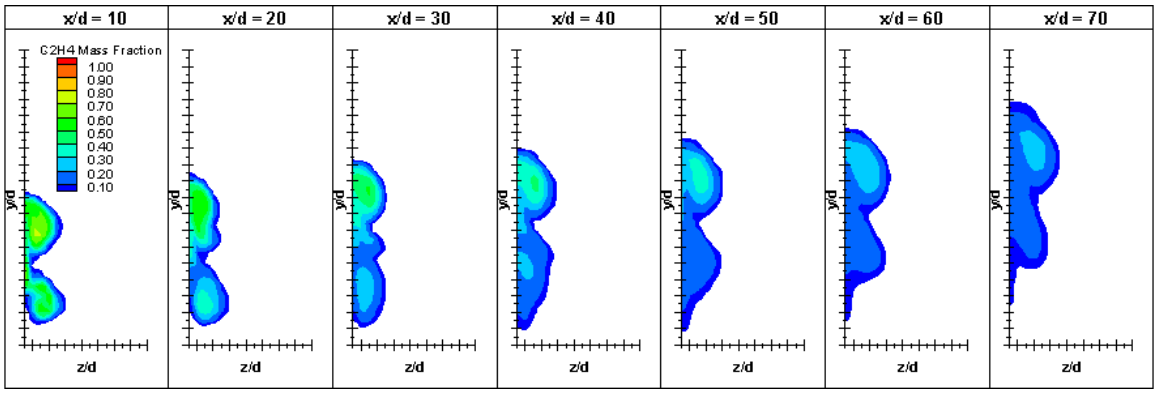

Figure 65. LWH-7x2x4-5h fuel species contour plot of C_2H_4.

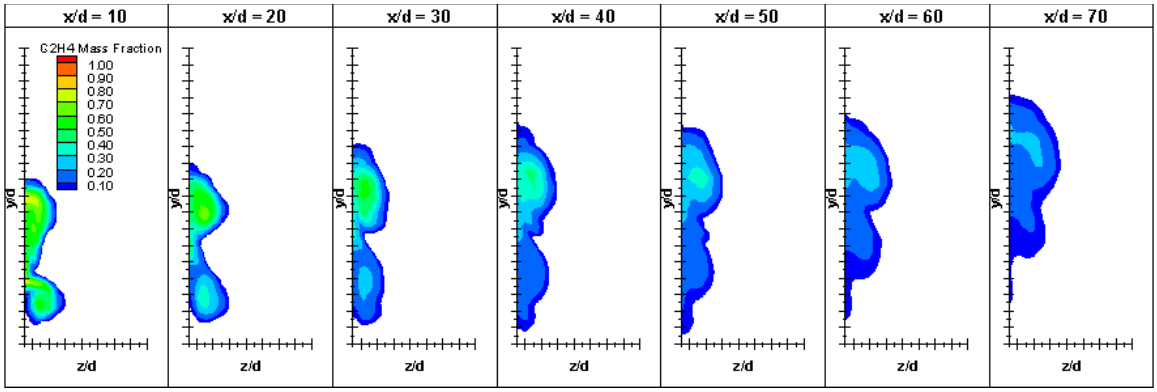

Figure 66. LWH-7x2x4-6h fuel species contour plot of C_2H_4.

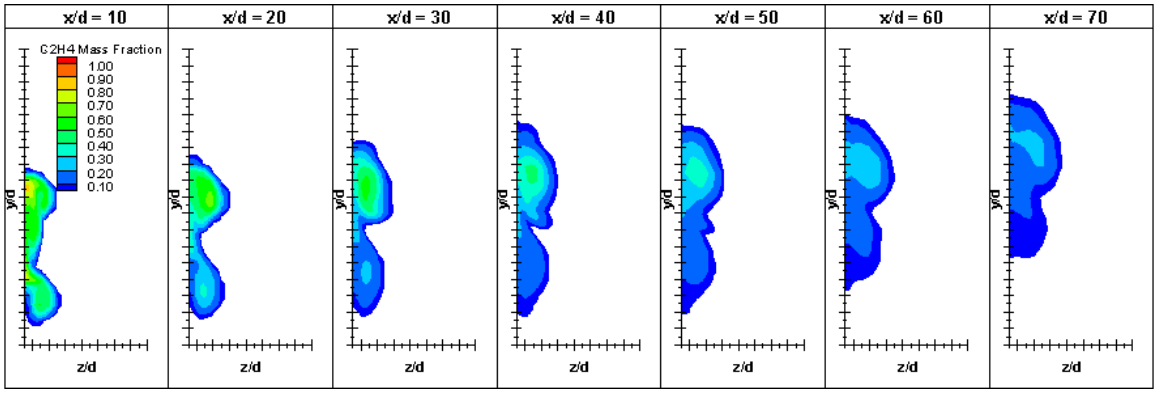

Figure 67. LWH-7x2x4-7h fuel species contour plot of C_2H_4.

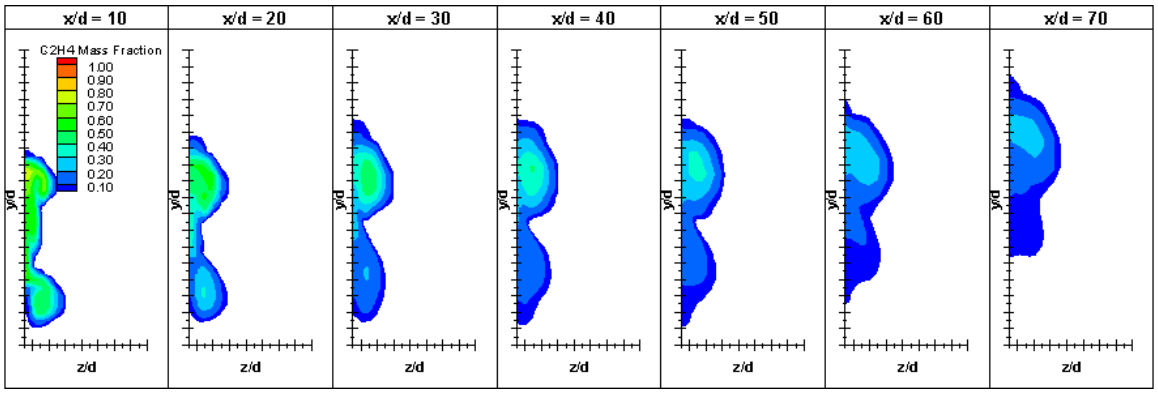

Figure 68. LWH-7x2x4-8h fuel species contour plot of C_2H_4.

Minimal deviations were seen in the species contour plots for the variations in the absolute height of the LWH7x2x4 pylons. The main effect of increasing the height of this pylon was a migration of the area of highest concentration into the upper set of counter-rotating vortices. The lower pair of vortices diminishes in size and fuel concentration rapidly as the height of this pylon is increased. There is slight upward movement of the both the lower and upper sets of vortices in addition to increased floor-gap in the 7 and 8 diameter tall pylons. The species contour plots with velocity vector overlay are not presented here but can be found in Appendix A.

The dramatic shift of high concentration of fuel to the top of the fuel plume within the upper vortices is clearly shown in the core penetration plot of Figure 69. This shift happens with the very first incremental scaling of the pylon. The location of maximum fuel concentration is over 40% deeper into the freestream for the LWH-7x2x4-5h than the original LWH-7x2x4-4h pylon. The 6, 7, and 8 diameter tall pylons' core penetration plots are grouped tightly together in the far downstream locations, representing approximately a 50% increase in penetration over the unmodified pylon.

The total fuel plume penetration for this test matrix can be seen in Figure 70. Increasing the pylon height has a similar effect on the LWH-7x2x4 pylon as was seen in the LWH-7x1x4 pylon. Total penetration for the LWH-7x2x4-8h pylon is 20% greater than the unmodified LWH-7x2x4-4h pylon. Increasing the height of the LWH7x1x4 Pylon 1 diameter equated to an approximately 1 diameter increase in penetration. A similar 1:1 ratio was seen in the LWH-7x2x4 pylons as well.

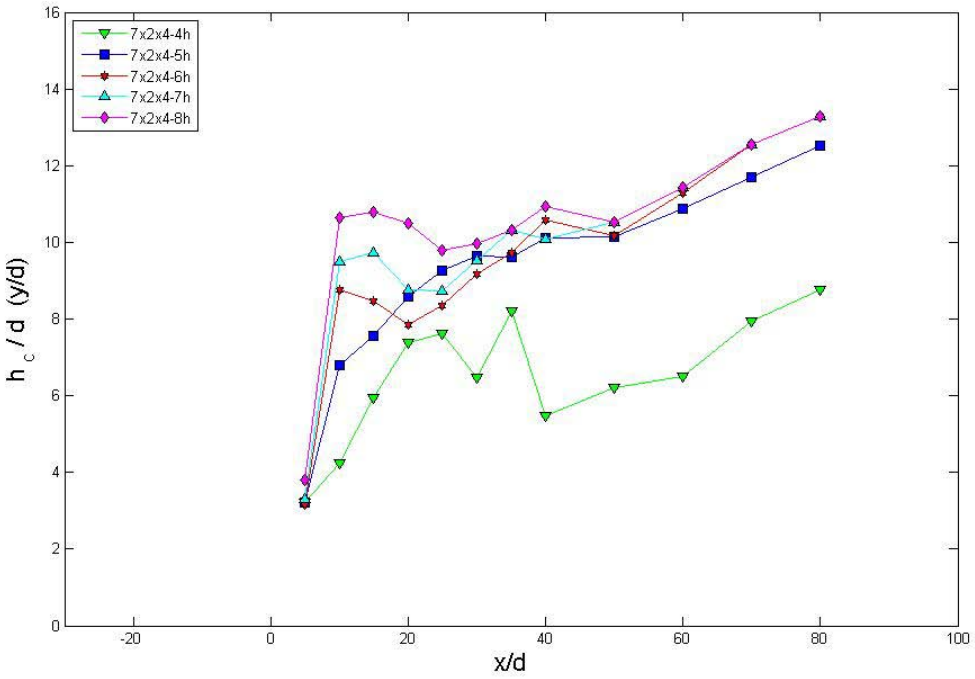

Figure 69. Penetration of location of maximum equivalence ratio for the third test case matrix, representing variation in absolute pylon height for the LWH-7x2x4 pylon.

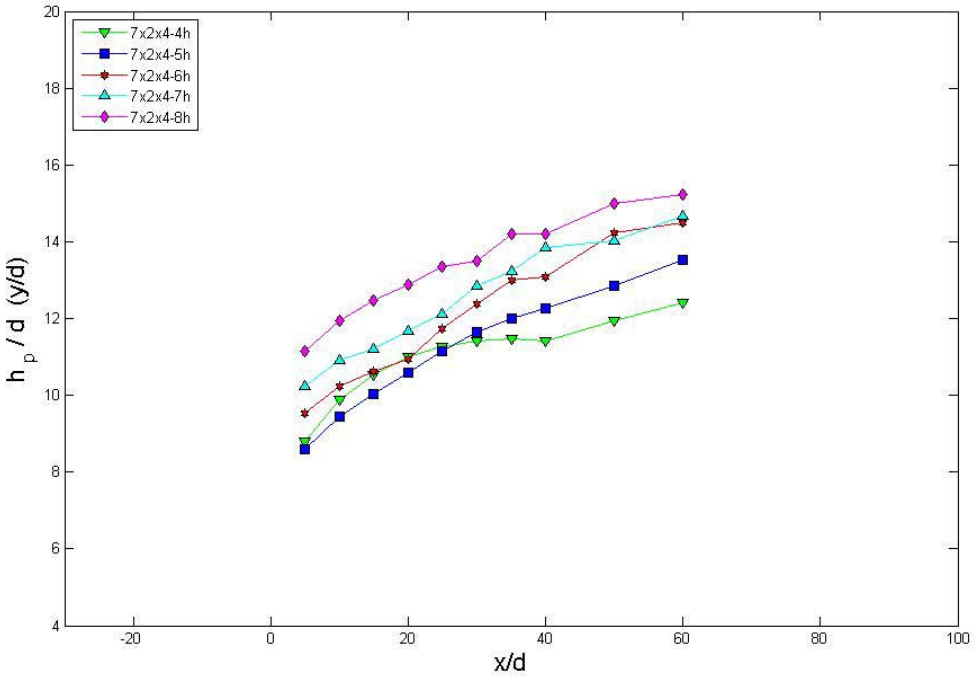

Figure 70. Total Penetration for the third test case matrix, representing variation in absolute pylon height for the LWH-7x2x4 pylon.

The change in total plume area for the third test matrix was similar to that seen in the second test matrix. Increasing the absolute pylon height related to linear increase in plume area for the LWH-7x2x4 pylons. All pylons displayed similar behavior in total plume spreading. From the injector to the end of the flame-holding cavity the plume linearly increased in size, beyond the flame-holding cavity (x/d = 60) the rate of plume spreading increased but still behaved linearly. The largest pylon, LWH-7x2x4-8h, exhibited a fuel plume area 34% larger than the unmodified LWH-7x2x4-4h pylon.

The flammable fuel plume area increased in a similar fashion to what was seen in the second test matrix. The flammable fuel plume areas for the height variations of the LWH-7x2x4 pylon all maintained similar rates of growth. Each plume saw a near linear increase in flammable fuel plume area as the downstream distance increased. The slope

of the linear increase in spreading rate increases slightly as the pylon height increased. Ultimately the 8 diameter tall pylon produced a flammable fuel plume area 33% larger than the unmodified LWH-7x2x4 pylon. The flammable mixture distance varied greatly with different sized pylons. In the first test matrix the LWH-7x2x4 pylon had the shortest x_{fmd} for the 7 pylons tested with varying widths. In the previous the matrix it was seen that increasing the height of the LWH-7x1x4 pylon decreased the flammable mixture distance; however, there was no corollary in this test matrix. Increasing the height of the LWH-7x2x4 pylon did not shorten the x_{fmd} nor was there a linear increase in $x_{fmd.}$ The height of theLWH-7x2x4 pylon does not seem to correlate to the flammable mixture distance. The total fuel plume area for the LWH-7x2x4 pylons can be seen below in Figure 71, Figure 72 depicts the flammable fuel plume area and flammable mixture distance for the variations in height of the LWH-7x2x4 pylon.

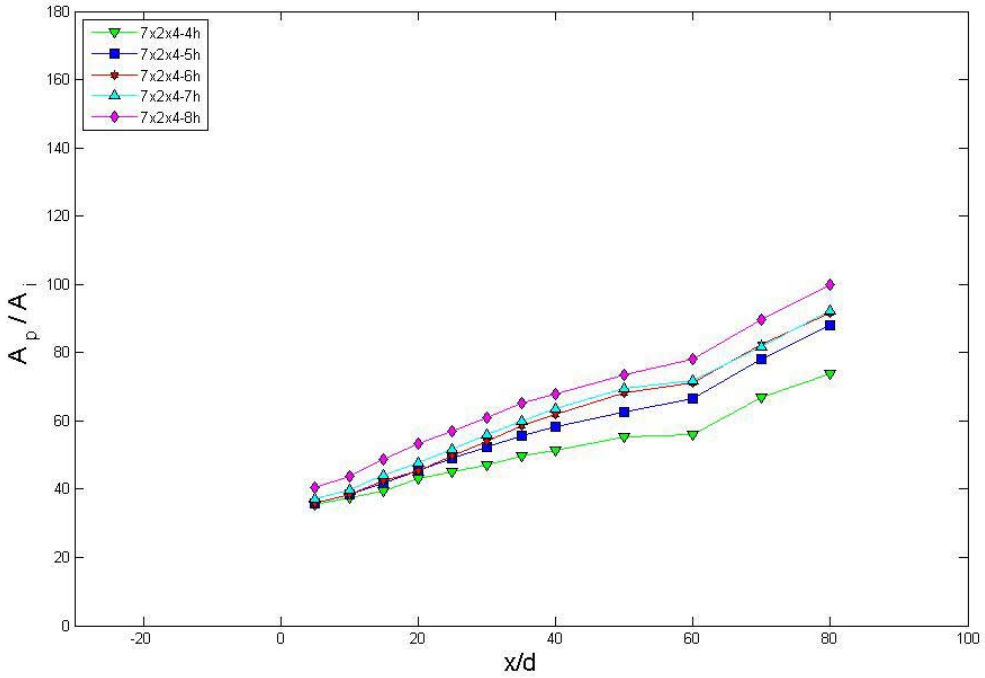

Figure 71. Fuel plume area for the third test case matrix, representing variation in absolute pylon height for the LWH-7x2x4 pylon.

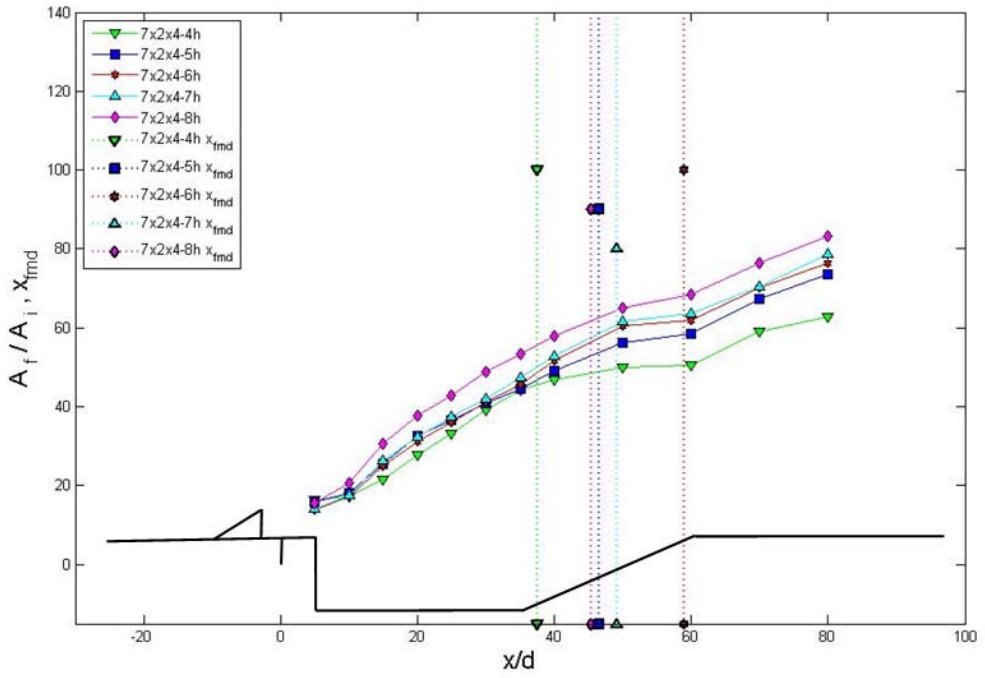

Figure 72. Flammable fuel plume area and flammable mixture distance for the third test case matrix, representing variation in absolute pylon height for the LWH-7x2x4 pylon.

The pressure loss curves for the absolute height variations in the LWH-7x2x4 pylon can be seen in Figure 73. Once again the pressure loss associated pylon aided normal fuel injection was seen to be minimal. And much like the behavior seen in the second test matrix the total pressure loss coefficient appears to be skewed for the unmodified 4 diameter tall pylon. The 5 diameter tall pylon posses the lowest loss at the first data reduction point, with slight increases in losses for the corresponding larger pylons. These pressure loss curves begin to merge towards the back portion of the flame-holding cavity (x/d = 50). At the far downstream locations the pressure loss curves begin to diverge again with the larger LWH-7x2x4-7h and 8h pylons showing higher losses than the other smaller pylons. While meeting the same convergence criteria the modified pylons ran for more iterations than the unmodified pylon.

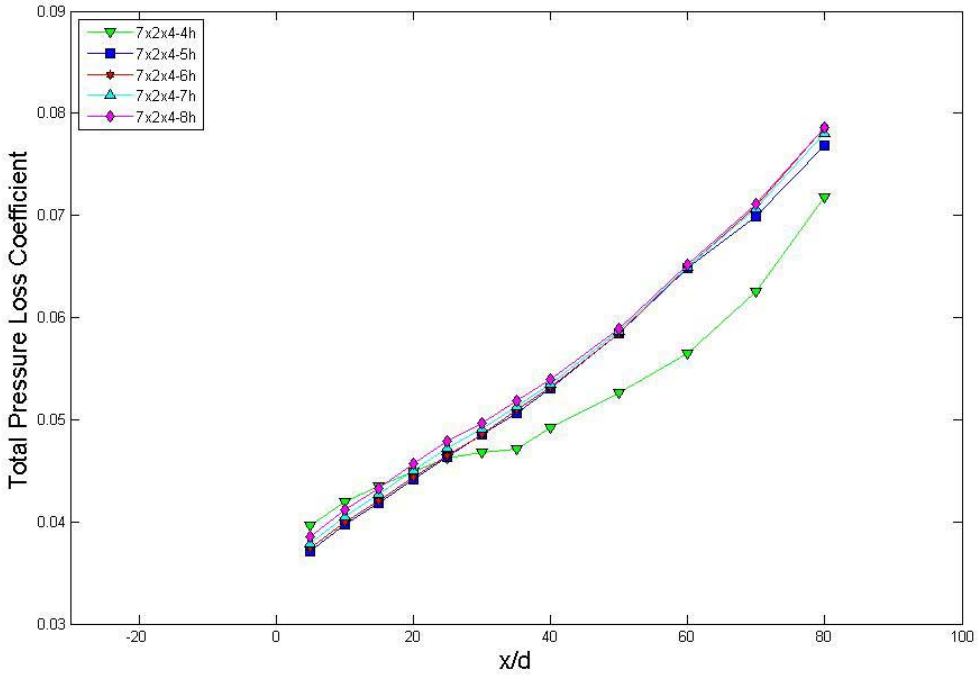

Figure 73. Total pressure loss coefficient for the third test case matrix, representing variation in absolute pylon height for the LWH-7x2x4 pylon.

LWH-7x2x4 Variation in Pylon Height Summary

Increasing the scale of the LWH-7x2x4 pylon to heights of 5, 6, 7, and 8 diameters shared some of the improvements that were seen in second test matrix. These modified pylons maintained the same leading edge wedge angle and width to height ratio of 0.5 as the LWH-7x2x4 pylon. With the unmodified LWH-7x2x4 pylon as a starting point, increasing the absolute size of the pylon had the following effects:

- Slightly Increased Floor-gap
    - The lower set of vortices penetrates higher into the freestream
- Increased Fuel Core Penetration
- Increased Total Plume Penetration
- Increased Flammable Fuel Plume Area
- Minimal Impact on Pressure Loss

4.5 Mixing Analysis Test Matrix 4- Pylon Wedge Angle Variation

Species Contour Plots

The last set of simulations seeks to identify the impact of varying the leading edge wedge angle on the fuel-air mixing metrics. For these simulations the LWH-7x2x4 pylon with a 29.7° leading edge wedge angle was chosen as the baseline pylon with the injection properties still remaining the same throughout. The length of the pylon was altered to create wedge angles of 15°, 22°, 37°, 45°, and 50° for a total of 6 variations spanning 35° in approximately 7.5° increments. The pylons with a leading edge wedge angle greater than the unmodified pylon area referred to as 'blunt' whereas those pylons with wedge angles less than 30° are referred to as 'sharp' All pylons in this test matrix maintain a height of 4 diameters and a width of 2 diameters. Figures 74 through 79 provide the fuel species contour plots associated with these pylons.

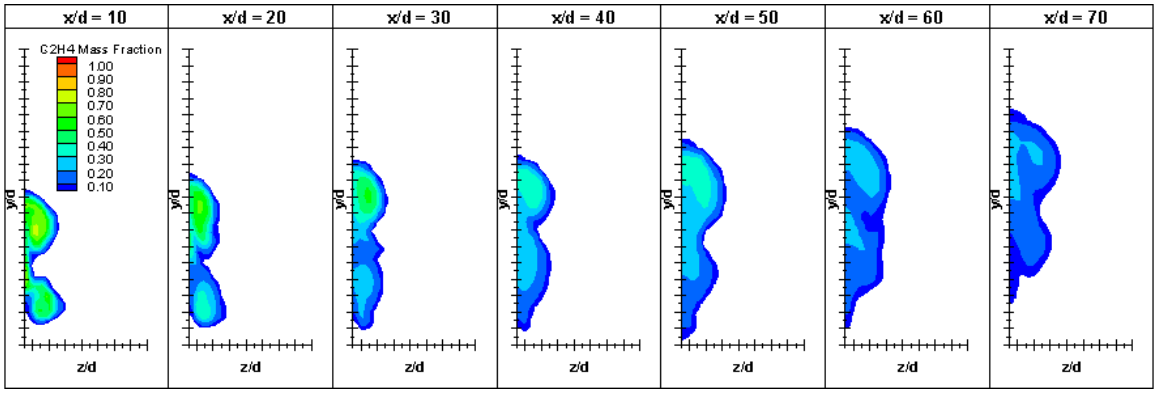

Figure 74. LWH-7x2x4-15° leading edge wedge angle fuel species contour plot of C_2H_4.

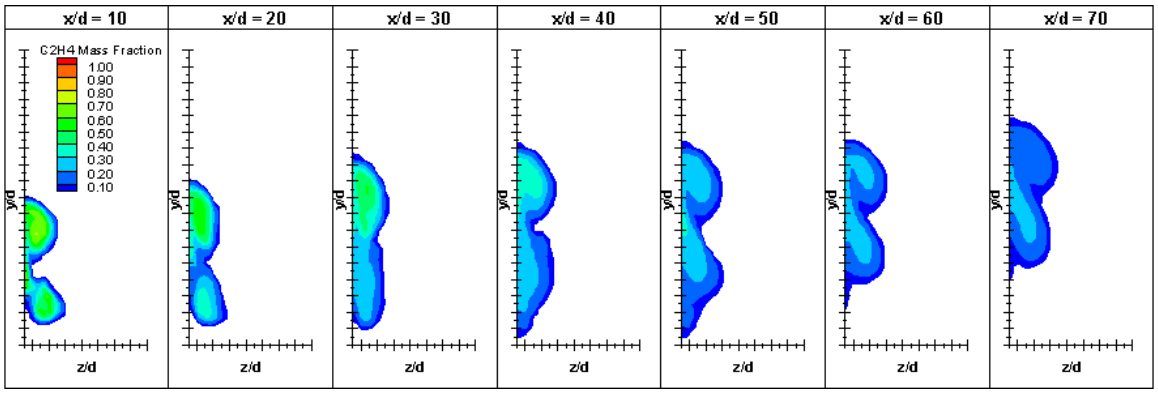

Figure 75. LWH-7x2x4-22° leading edge wedge angle fuel species contour plot of C_2H_4.

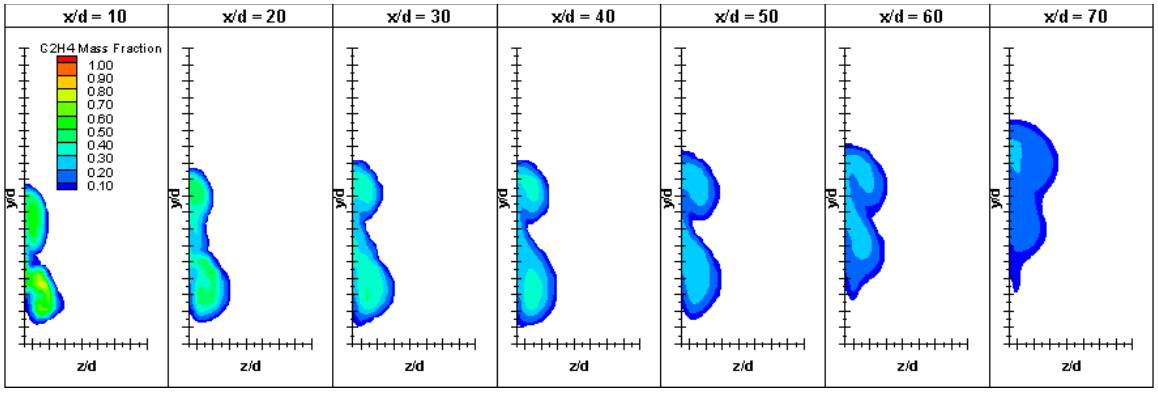

Figure 76. LWH-7x2x4-30° leading edge wedge angle fuel species contour plot of C_2H_4.

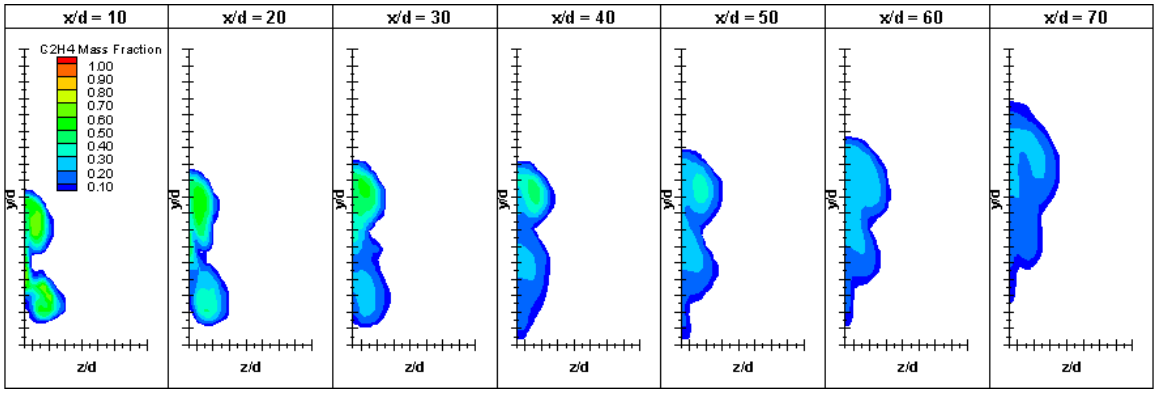

Figure 77. LWH-7x2x4-37° leading edge wedge angle fuel species contour plot of C_2H_4.

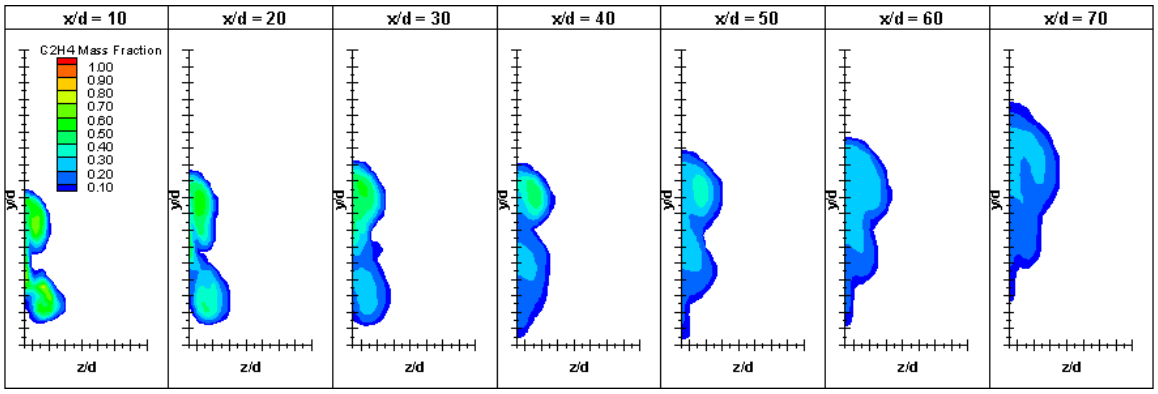

Figure 78. LWH-7x2x4-45° leading edge wedge angle fuel species contour plot of C_2H_4.

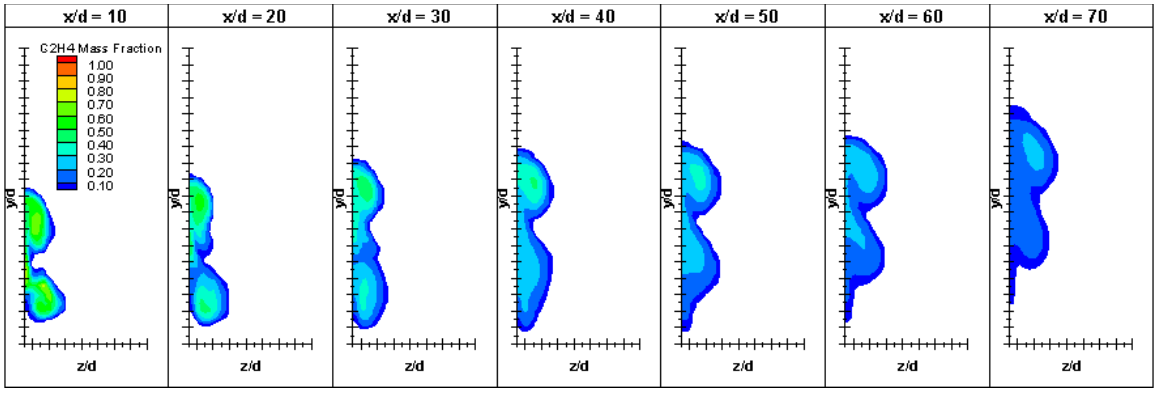

Figure 79. LWH-7x2x4-50° leading edge wedge angle fuel species contour plot of C_2H_4.

Elongating the length of the pylon to create a more acute, or sharp, leading edge wedge angle (22° and 15°) seems to move the greatest concentration of fuel higher into the fuel plume away from the lower set of vortices and into the upper set. Penetration and floor-gap do not appear to be drastically affected by the increasingly sharp leading edge wedge angle. Decreasing the length of the pylon and creating a blunter leading edge (37°, 45°, and 50° leading edge wedge angle) also appears to shift the fuel higher into the fuel plume. A very slight decrease in floor-gap is seen in the blunt pylons when compared to the unmodified LWH-7x2x4-30° pylon; however, this is also seen in the

sharp pylons. Once again it appears that there is inconsistent behavior in the first test matrix results. The unmodified LWH-7x2x4-30° results are taken from this first test case. The variations that are seen in the modified pylon species contour plots are insignificant.

Inspection of the total fuel plume areas, as seen below in Figure 80, shows relatively minor variation in this mixing metric. The two sharp pylons each present slight deviations from the mean plume area midway over the flame-holding cavity. Overall the behavior of these different pylons is quite similar in fuel plume spreading. Figure 81 illustrates the flammable fuel plume area and flammable mixture distance for this test matrix. The two sharp pylons again show the same slight deviation from the rest of the pylons midway over the cavity, but these differences are minor. The flammable mixture distance does not appear to correlate to the leading edge wedge angle. The sharp pylons x_{fmd} bracket those of the blunt pylons. All five of the modified pylons produce longer flammable mixture distances than the unmodified 30° leading edge wedge angle pylon.

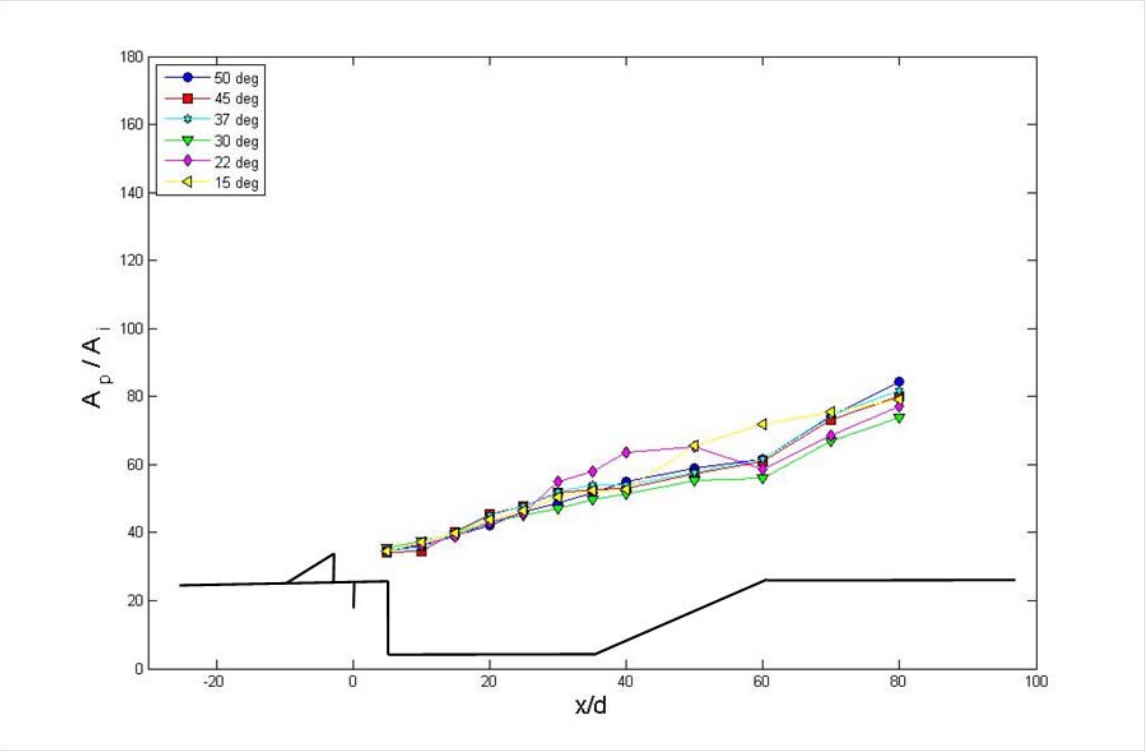

Figure 80. Total fuel plume area for the fourth test case matrix, representing variation in leading edge wedge angle for the LWH-7x2x4 pylon.

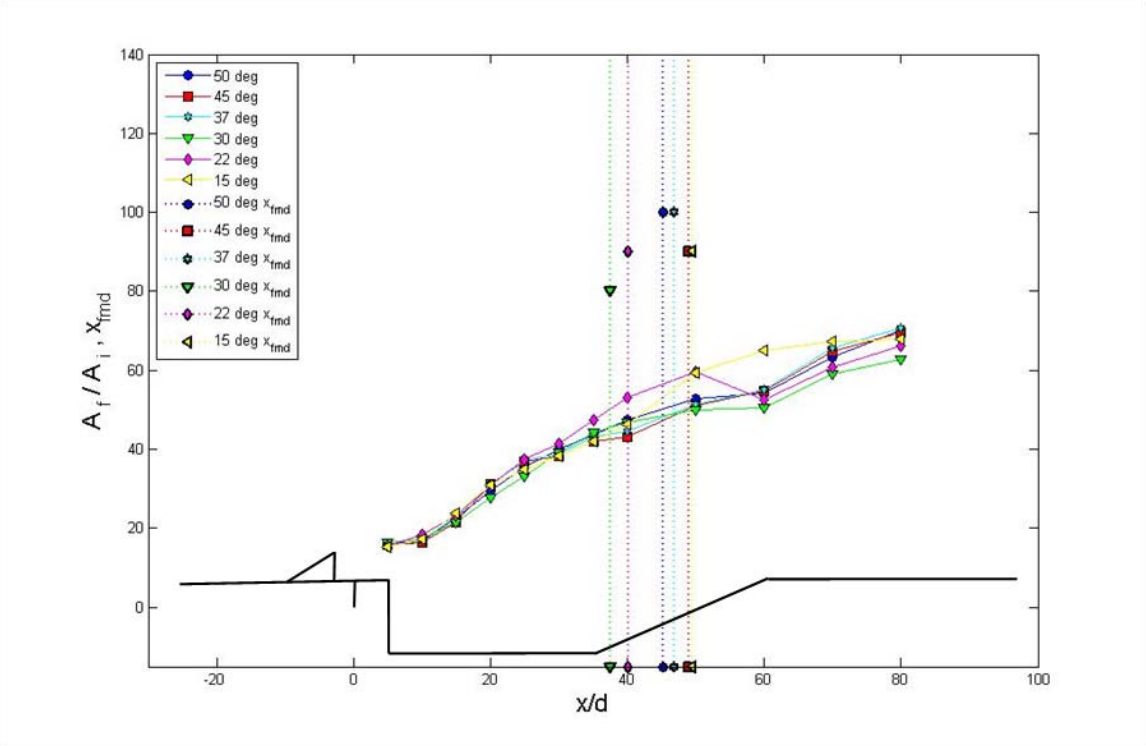

Figure 81. Total flammable fuel plume area and flammable fuel mixture distance for the fourth test case matrix, representing variation in leading edge wedge angle for the LWH-7x2x4 pylon.

Total plume penetration and core plume penetration into the freestream are not greatly affected by the leading edge wedge angle. Below in Figure 82, the total plume penetration for the fourth test matrix is given. All modified pylons appear to slightly increase penetration into the freestream in the far downstream locations. The penetration of the core of the pylon into the freestream, seen in Figure 83, indicate that the highest concentration of fuel migrates further into the freestream for the modified pylons over the base LWH-7x2x4-30° pylon. The blunt pylons display slightly greater penetration than the sharp pylons and the 45° and 37° produce near identical values of core penetration. In general the leading edge wedge angle has minimal impact on both total fuel plume penetration and core fuel plume penetration.

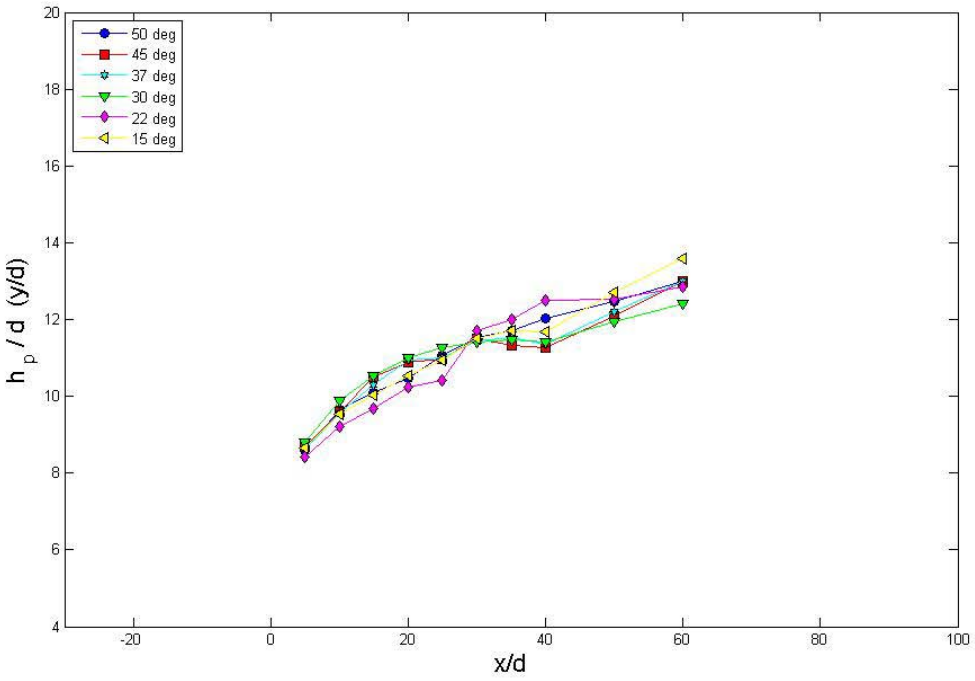

Figure 82. Total fuel plume penetration for the fourth test case matrix, representing variation in leading edge wedge angle for the LWH-7x2x4 pylon.

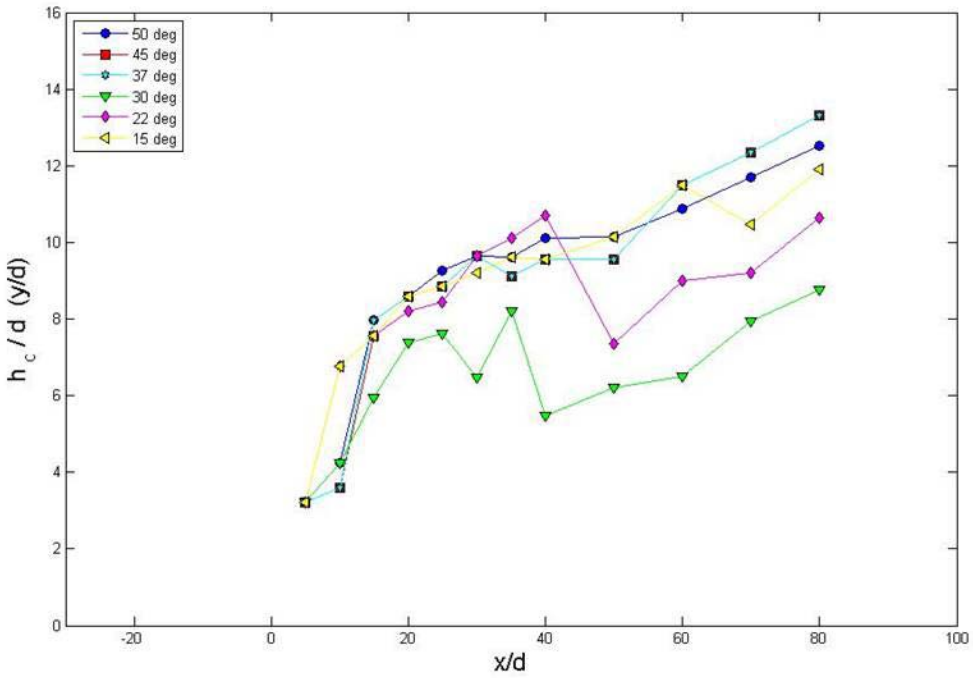

Figure 83. Fuel core penetration for the fourth test case matrix, representing variation in leading edge wedge angle for the LWH-7x2x4 pylon.

The total pressure loss coefficient does appear to be affected by the leading edge wedge angle. In the first test matrix it was postulated that the presence of the pylon and associated weak bow shock lowered overall pressure loss when compared to the baseline case with no pylon. All pylons in the first test matrix maintained the same length, and thus, the same leading edge wedge angle. There was no direct correlation with pressure loss and pylon width. The 1/2 diameter wide pylon showed similar losses as the 5 diameter wide pylon in the first data collection plane. Creating a longer pylon, with a corresponding more acute leading edge wedge angle, should create a weaker bow shock and thus decrease pressure loss. This effect was seen in the LWH-7x2x4-15° pylon, which displayed the lowest initial losses of all the modified pylons. However the 22°

showed no noticeable improvement in initial pressure loss over the blunt pylons. And once again, as seen in the second and third test matrix, the unmodified 30° pylon displayed pressure loss behavior that did not trend in a similar fashion to the rest of modified pylons in the test case. The total pressure loss coefficient for the fourth test matrix representing variations in the leading edge wedge angle for the LWH-7x2x4 pylon can be seen below in Figure 84.

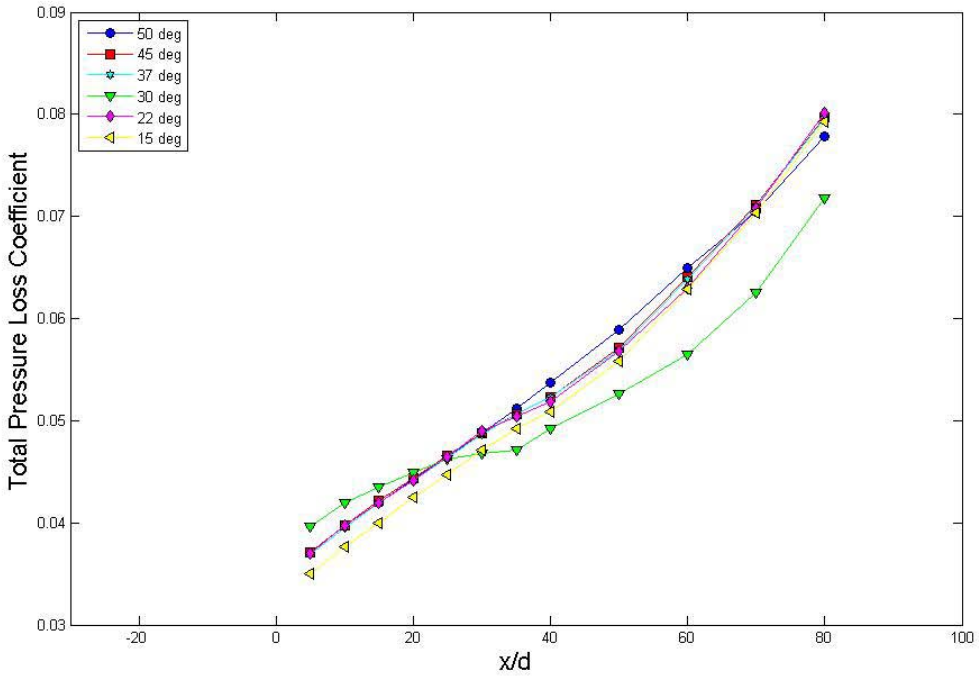

Figure 84. Total pressure loss coefficient for the fourth test case matrix, representing variation in leading edge wedge angle for the LWH-7x2x4 pylon.

LWH-7x2x4 Variation in Pylon Leading Edge Wedge Angle Summary

The species contour plots and fuel-air mixing metrics seen in Figures 74 through 84 suggest that the leading edge wedge angle has no significant impact on the mixing performance of a pylon. Some improvement was seen in the total pressure loss

coefficient with the use of the long and sharp LWH-7x2x4-15° pylon. However, there was no corresponding effect on total pressure loss for the 22° pylon, which shared similar losses as the three blunt pylons. Trends in the migration of maximum fuel concentration higher into the fuel plume that were observed in this test matrix may be caused not by differences in the actual flow structure caused by the different pylons, but by a less than fully converged baseline test case (LWH-7x2x4-30°).

4.6 Comparison to Experimental Work

As stated in Chapter 3, these numerical simulations are a direct follow on effort to experimental work performed by Haubelt[1]. The experimental setup used in his work was duplicated in this CFD study. There is uncertainty in the exact manner in how Haubelt collected some of his penetration data. This uncertainty comes from the fact that the baseline or floor from which penetration heights are measured from is not clearly defined. Since the floor of the test section (containing the pylon fuel injector, and flame-holding cavity) is on a 2.5° diverging ramp it is unclear whether the 'zero' used to define penetration is the physical floor of the test section or the transverse location of the fuel injector. The data presented here in these simulations uses the y coordinate of the center of the fuel injector. Depending on the origin used the penetration height may vary as a function of the downstream distance multiplied by the tangent of the 2.5° ramp; this equates to approximately 2.6 diameters at the x/d = 60 location. Due to this 2.5° declination of the ramp floor the data reduction planes are also skewed slightly. The data

reduction planes presented here are normal to the ceiling of the test section, and not the floor.

Comparing the species contour plots from the numerical simulations performed here to the experimental work performed by Haubelt[1] and Montes[3] yields mixed results. Montes performed similar experimental work to Haubelt with two main differences. The pylons and fuel injector used in Montes work were placed further upstream from the cavity than Haubelt. The pylons used in Montes' work is placed 2.3 inches upstream of the flame-holding cavity as opposed to the 0.35 inches used in both Haubelt's experimental work and this CFD study. Additionally Montes used nitric oxide instead of ethylene as an injectant. Nitric oxide has a similar molecular weight as ethylene. The difference in fuel-air mixing metrics from using nitric oxide verse ethylene is expected to be minimal[1]. In Figure 85 the species contour plots for the baseline test case at the x/d = 12 location can be seen for both experimental and CFD simulations. The image on the left is the experimental data collected by Haubelt and the image on the right are results from this study. The equivalence ratio scale is the same for both species contour plots. Inspection of this figure shows similar overall fuel plume structures. The CFD data shows a much higher concentration of fuel in the fuel plume and a smaller overall size. It appears that the turbulence model has insufficiently modeled the level or magnitude of turbulence created by the complex flow structure associated with normal fuel injection. The smaller plume area and higher fuel concentrations indicate a lack of spreading and mixing of the fuel plume with the freestream. The floor-gap and penetration into the freestream of the numerical results is consistent with the experimental results.

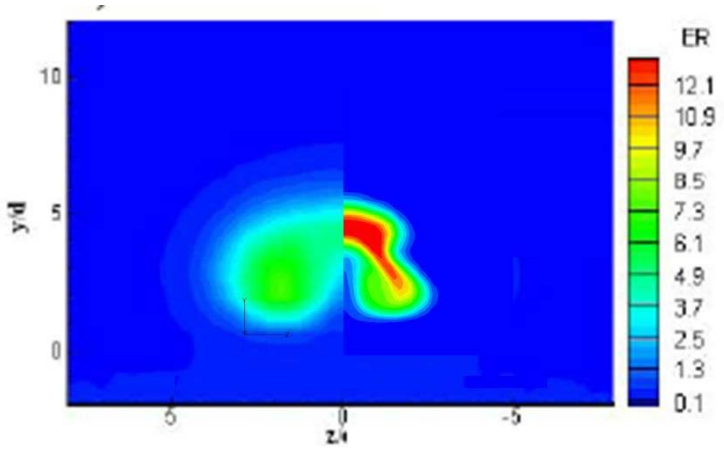

Figure 85. Comparison of experimental[1], on the left, and computational results, on the right, of equivalence ratio contour plots for the baseline, no pylon, test case at x/d = 12.

Figure 86 presents both experimental[1] and CFD species contour plot of for pylon-aided normal fuel injection. The 'medium' pylon used here was approximately 0.25 inches tall, 0.07 inches wide and 0.43 inches long with a leading edge wedge angle of 30 degrees. Using the naming convention developed in this study the medium pylon would be LWH-7x1.2x4. This figure shows much better correlation in fuel concentration between the experimental and CFD results. However, the CFD results depict much greater penetration into the freestream as well as a much smaller plume area. Both the experimental and CFD results depict a fuel plume with two sets of counter-rotating vortices, one each at the top and bottom of the fuel plume. Also, the lower set of vortices has spread further in the z direction for both the experimental and CFD results. Comparing the CFD results against Montes experimental results yields a closer correlation in penetration and floor-gap but again the experimental results have a generally 'fatter' plume and therefore greater fuel plume area. Once again it appears that the k-ω turbulence model has under predicted the magnitude of turbulence in the wake of the pylon and in the fuel plume structure

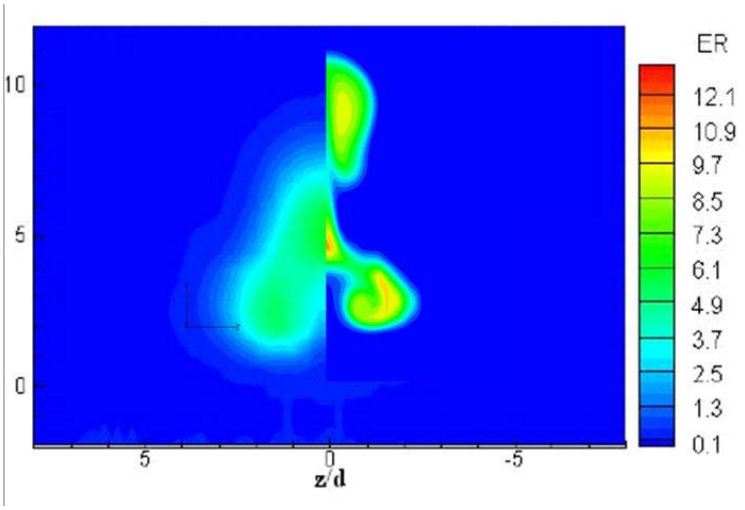

Figure 86. Comparison of species contour plot between Haubelt's experimental[1] work and computational results from this study for pylon-aided normal fuel injection at x/d = 12.

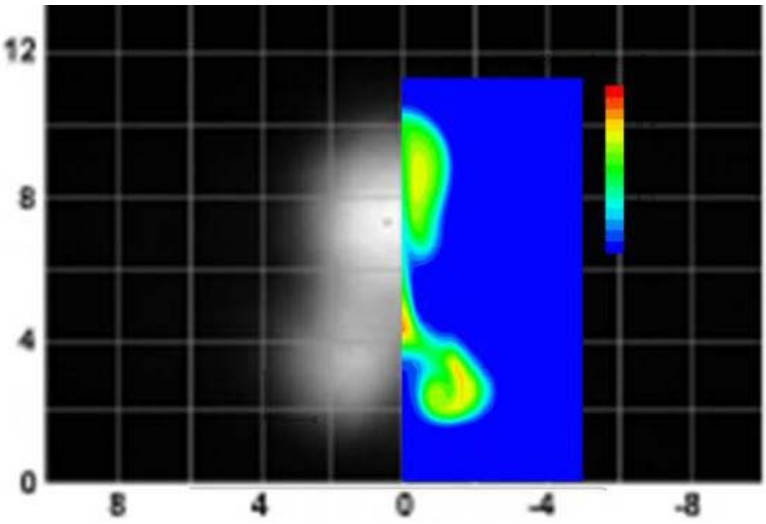

Figure 87. Comparison of species contour plot between Montes' experimental[3] work and computational results from this study for pylon-aided normal fuel injection at x/d = 12.

Further investigation of the baseline-normal fuel injection case shows strong correlation with past experimental results. Figure 88 presents a detailed schematic of flow structures seen in normal fuel injection[32]. In Figure 89 a shadowgraph from

Haubelt's experimental work is presented next to CFD results from this study that depict Mach contours in grayscale. These figures show that the CFD simulation has properly captured the flow structures including the bow shock Mach disc and separation shock that are typically seen in normal fuel injection. Good correlation with the experimental[1] is seen as well.

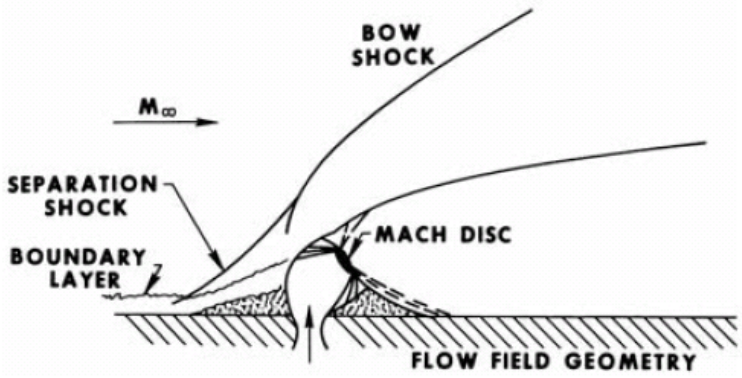

Figure 88. Schematic of normal fuel injection[32].

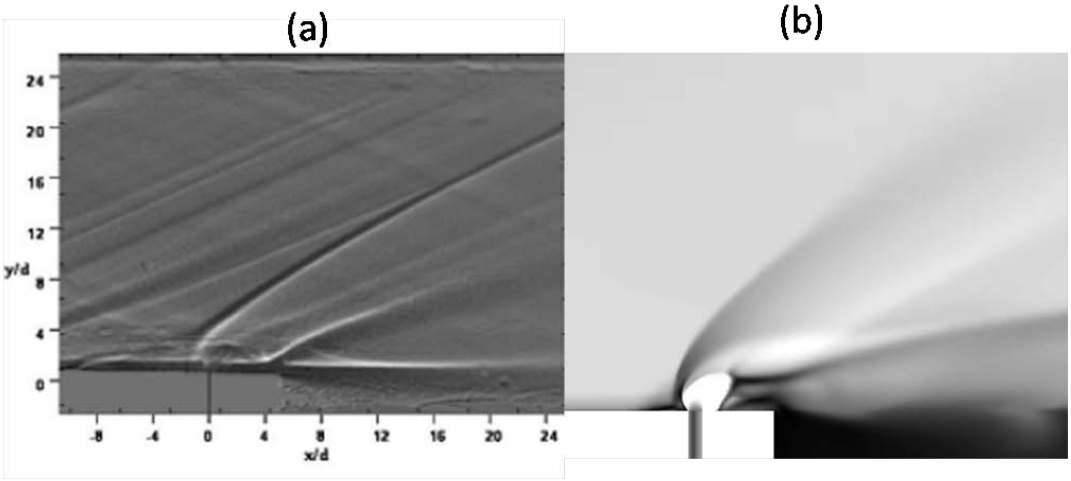

Figure 89. Shadowgraph (a) of the baseline test case in Haulbelt's[1] experimental work and CFD Mach contours (b) of normal fuel injection upstream of a flame-holding cavity.

The qualitative assessments above clearly indicated disparities in fuel plume areas between experimental and CFD results along with differences in plume penetration. Quantitative analysis of fuel plume areas, total fuel plume penetration, and maximum equivalence ratio show the CFD results from this study under predict plume areas and over predict core penetration and maximum equivalence ratio. Quantitative comparisons against Haubelt's experimental work for the 'medium' pylon at the x/d = 12 location can be seen below in Table 3. For the baseline test case the CFD results indicate a far smaller fuel plume area, and even greater error in the flammable fuel plume area. Since the fuel injection properties are the same for both the experimental[1] and computational work; the higher fuel concentration (Φ_{max}) in the CFD results can be directly contributed to the smaller fuel plume area caused by the under predicted turbulence. The great disparity in total fuel plume penetration and floor-gap between Haubelt's experimental work[1] and these CFD results may call into question the accuracy of these numerical simulations. However, the very close correlation in fuel plume structure, penetration, and floor-gap between Montes experimental work[3] and these CFD results provide reassurance that the results of this numerical study are in fact applicable. Comparison against Montes data yields error of only 9 % for total fuel plume penetration. Generally, correlation to experimental data less than 10-15 % error indicates positive and plausible CFD results.

Table 3. Fuel-air mixing metric comparison between experimental and CFD results for medium pylon at x/d = 12 location.

	Experimental(1)	CFD	Error (%)
A_p/A_i	65	38.6	-68
A_f/A_i	47	21.9	-114
h_p (y/d)	8.96	11.50	22
Φ_{max}	6.17	9.74	36

Comparison to experimental data has shown that similar fuel plume structures are formed in the CFD environment as are seen in experimental data. This similar fuel plume structure was evident in both the normal fuel injection test case where the fuel plume is dominated by one large set of counter-rotating vortices and in pylon-aided normal fuel injection where the fuel plume contains two sets of counter rotating vortices.

5. Conclusions

The goal of this research was to perform a parametric study on the physical geometry of the pylons used in pylon-aided normal fuel injection in the hopes of identifying trends in the fuel-air mixing metrics associated with varying individual aspects of the pylon's geometry. Twenty different pylon geometries were examined in this study representing a very large range of pylon widths, heights and lengths. Pylons are judged on several key fuel-air mixing metrics; penetration into the freestream, presence of floor-gap, size of flammable fuel plume area, and pressure losses.

The parametric study was divided into four test matrices that sought to identify the effects of independently varying one of the three key pylon geometries (height, width, and length) while keeping all other parameters fixed. The first test matrix varied the pylon width. Where past efforts have limited pylon width to 1-2 diameters wide, in this study pylon width was varied from 1/2 to 6 diameters wide. In this first set of simulations two general fuel plume structures were identified. Pylons with a width of less than 3 diameters produced fuel plume structures dominated by two sets of counter-rotating vortices. Pylons of widths greater than 3 diameters produced larger fuel plume dominated by a single set of counter-rotating vortices. The narrow pylons achieved very high levels of penetration into the freestream and viable levels of floor-gap. The wide pylons did not appreciably penetrate into the freestream though floor-gap was present in all but the 6 diameter wide pylon. These wide pylons produced flammable fuel plumes much larger than those found in the narrow pylons or baseline test case. All pylons were tested against a baseline test case of pure normal fuel injection without a pylon. In the

upstream data reduction planes, before the distorting effects of the flame-holding cavity affected the fuel plumes, all pylon-aided test cases produced flammable fuel plume larger than the baseline. Likewise all pylons tested suffered lower losses than the baseline test case. This effect may seem counter intuitive since the baseline case has no physical obstruction in the flow. However, the normal bow shock wave that is created by the baseline test case is much stronger than the oblique bow shock waves created by the presence of the pylons. The pylons test cases do not produce a strong normal shock upstream of the fuel injector, as seen in the baseline test case. These pylons do produce oblique shock waves. In oblique shock waves as the ramp angle is decreased the strength of the shock wave produced is correspondingly reduced.

The second and third test cases sought to identify the impact of scaling up in size two of the pylons investigated in the first test matrix. Here the height to width ratio and leading edge wedge angle of the two pylons were kept constant as the pylons were scaled in four equal iterations until the total height was doubled. Increasing the absolute height of the pylons increased the total penetration, flammable fuel plume area, fuel core penetration and floor-gap. The increased height and overall scale of the pylons did not lead to an appreciable increase in total pressure loss.

In the final portion of this parametric study the leading edge wedge angle was varied while keeping the width and height of the pylon constant. These pylons of differing lengths had very little variation in the key fuel–air mixing metrics. Therefore, the pylon rear face area has the largest impact on the mixing performance.

The greatest amount of penetration was found when using the narrowest pylons. The 1/2 and 1 diameter wide pylons penetrated approximately 14 diameters, or 3.5 pylon

heights, into the freestream. This enhanced penetration represents over a 60% increase over the baseline test case. The 1 diameter wide pylon that was doubled in height (LWH-7x1x4-8h) produced a fuel plume that penetrated 18 diameters (2.25 pylon heights) into the freestream, 110% greater than the baseline.

The largest flammable fuel plume areas were created with the two widest pylons tested. The LWH-7x6x4 pylon created a flammable fuel plume area 51% greater than the baseline test case and 77% larger than the poorest performing pylon.

The use of pylon-aided normal fuel injection has been proven to be an effective fuel-air mixing strategy in scramjet engines. The large number and wide variation in pylon geometry created fuel plume and corresponding fuel-air mixing metrics that are highly dependent on pylon geometry. This work has identified how key metrics such as flammable fuel plume area, floor-gap, and penetration area affected by changes in the length, width, and height of the pylon. This information is critical for the design trade-offs that occur when determining the fuel injection strategy to be used in a scramjet engine

5.1 Desired Impact of this Research

The information provided in this paper will provide a foundation for future research and experimentation into the use of pylon-aided normal fuel injection in scramjet engines. The consensus of thought in pylon-aided fuel injection held that these pylons must be constrained to a width of approximately 1-2 diameters. This paper has offered the possibility that there may be beneficial impacts on fuel-air mixing when using

pylons of up to 6 diameters wide. Additionally this paper has identified trends in mixing performance due to the variation of different geometry parameters. In practice a scramjet engine would not depend on fuel injected from one pylon or source. Multiple and different shaped pylons may be staggered in the spanwise direction to produce a total fuel plume that incorporates both high degrees of penetration with one particular pylon, and the large flammable fuel plume area of another.

5.2 Recommendations for Future Experimentation

Several small anomalies were encountered in these simulations. The complex nature of this problem coupled with the sheer size of the computational grids and the large number of pylons tested placed a very real limit on computational resources. Allowing the solutions to run longer and let residuals decrease at least another order of magnitude may eliminate some of the peculiarities seen in test cases two, three, and four. Additionally, it may be beneficial to perform a similar study either without the flame-holding cavity or with the pylons placed much further upstream of the cavity to allow the far downstream plume structures to fully develop without interference from the flow structures associated with the flame-holding cavity. Further wind tunnel testing utilizing some of the larger and more radical pylons, including the 'wide' and 'sharp' pylons, tested in this study may provide greater insight into the absolute range of pylons sizes and shapes to be used in pylon-aid normal fuel injection.

Appendix A:

Figures 90 and 91 depict the equivalence ratio contour/ velocity vector plots for the LWH-7x1x4-5h and -7h pylons form test matrix 2. These two intermediate pylon sizes illustrate the same trends that were identified for the -4h, -6h, and -8h pylons. As the absolute pylon height is increased the penetration and floor gap continues to increase, while the same basic fuel plume structure is displayed. The bow shock waves are clearly evident at the x/d = 5 planes as the arc of velocity vectors above the top portion of the fuel plume. Also evident is the strength of the lower set of vortices at this same x/d = 5 location. The long arrows indicate that large amounts of air are being entrained into the fuel plume from the clean freestream air.

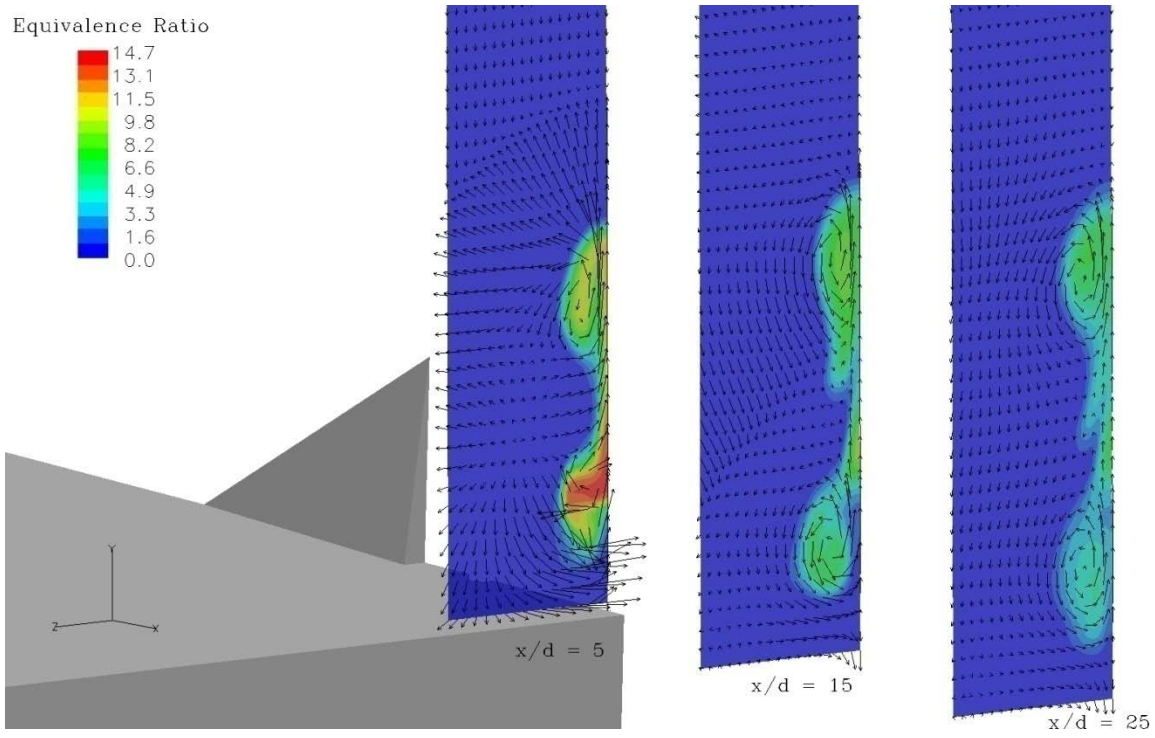

Figure 90. Equivalence ratio contour/velocity vector plot for the LWH-7x1x4-5h pylon**.**

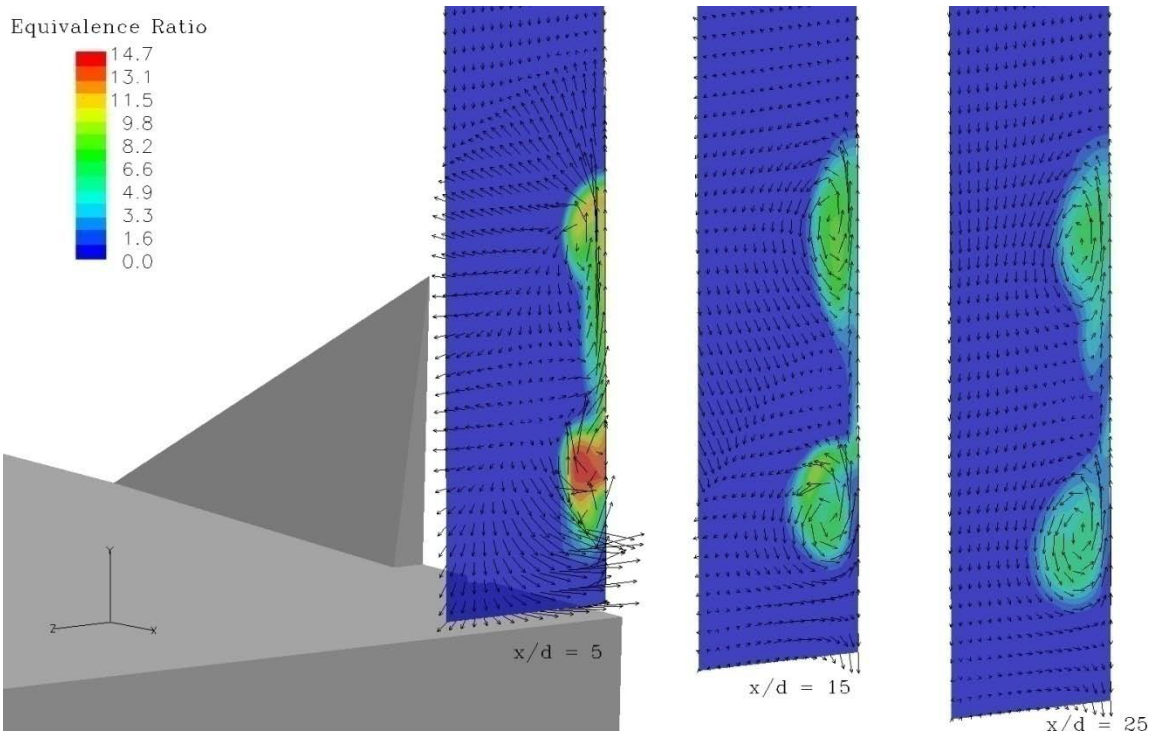

Figure 91. Equivalence ratio contour/velocity vector plot for the LWH-7x1x4-7h pylon.

Figures 92 through 95 provide some of the secondary fuel air mixing metrics that were omitted from Chapter 4. Figure 92 provides the variation in core fuel plume penetration as the LWH-7x1x4 pylon is scaled up to larger total heights in the second test matrix. Here the maximum concentration of fuel is seen to vary between the upper and lower set of vortices as downstream distance is varied. There is no clear correlation between absolute pylon height and location of core penetration. Figure 93 depicts the decay of maximum equivalence ratio over the test section. The flammable fuel plume percentages of the pylons investigated in test matrix two are seen in Figure 94. The mixing efficiency of the pylons examined in the second test matrix can be seen below in Figure 95. The decay of maximum equivalence ratio, flammable fuel plume percentage, and mixing efficiency seen in this test matrix was consistent with general trends and behaviors seen in other test matrices.

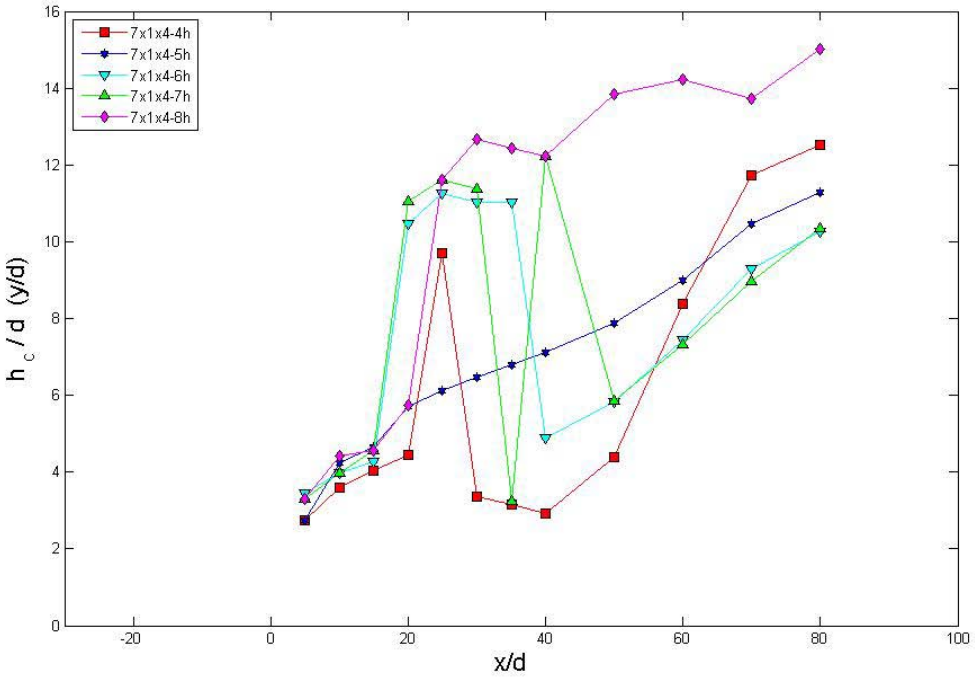

Figure 92. Fuel core penetration for the second test matrix, representing variation in absolute pylon height for the LWH-7x1x4 pylon.

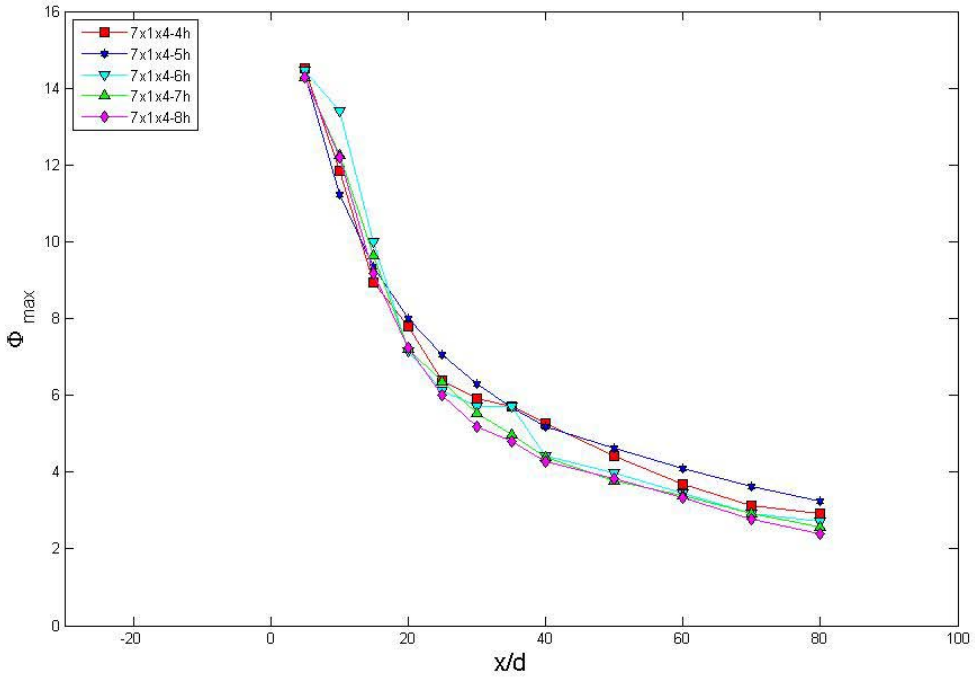

Figure 93. Decay of maximum equivalence ratio for the second test matrix, representing variation in absolute pylon height for the LWH-7x1x4 pylon.

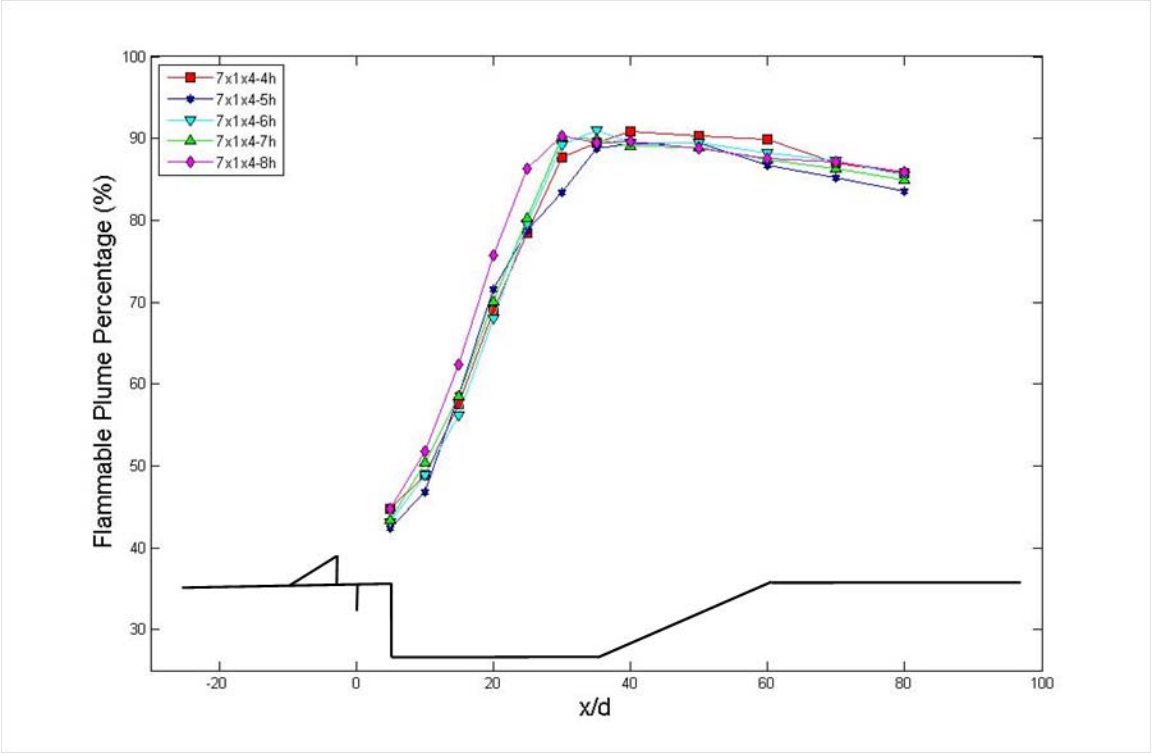

Figure 94. Flammable fuel plume percentage for the second test matrix, representing variation in absolute pylon height for the LWH-7x1x4 pylon.

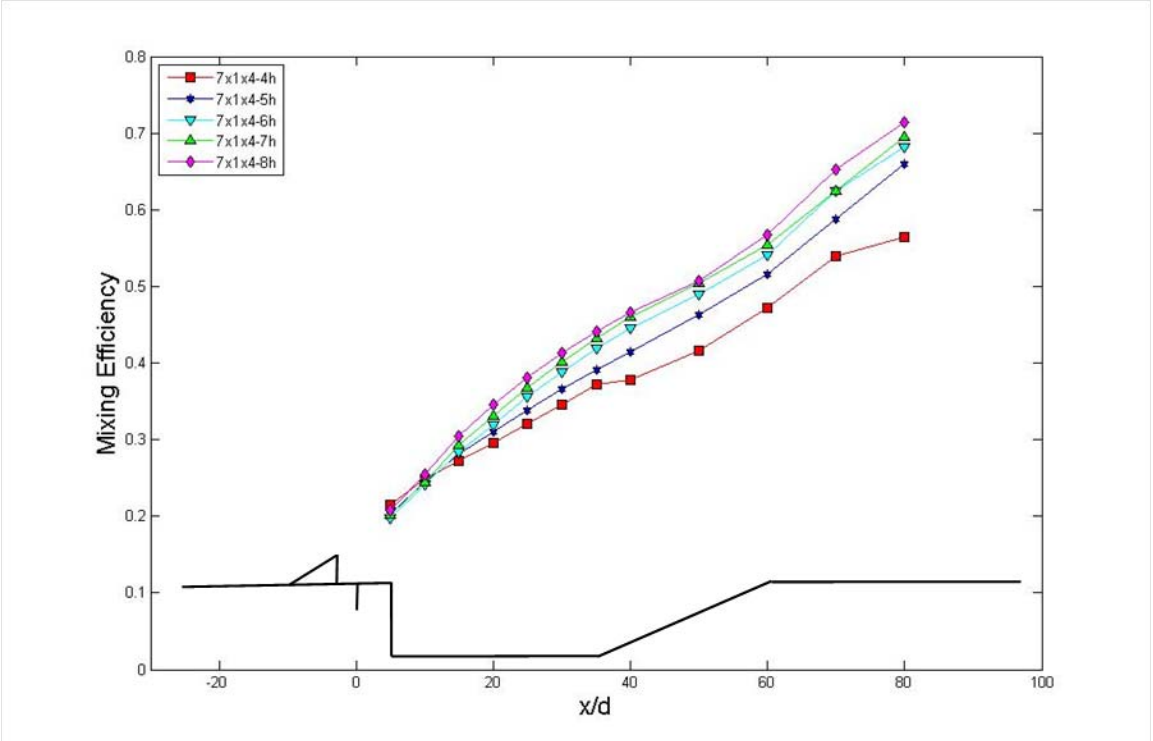

Figure 95. Mixing efficiency for the second test matrix, representing variation in absolute pylon height for the LWH-7x1x4 pylon.

Figures 96 through 99 depict the equivalence ratio contour/ velocity vector plots for the pylons investigated in the third test matrix. These pylons illustrate the same flow structures as seen in the second test matrix for a similarly scaled up pylon. As the absolute pylon height is increased the penetration continues to increase. Once again the bow shock waves are clearly evident at the x/d = 5 planes as the arc of velocity vectors above the top portion of the fuel plume.

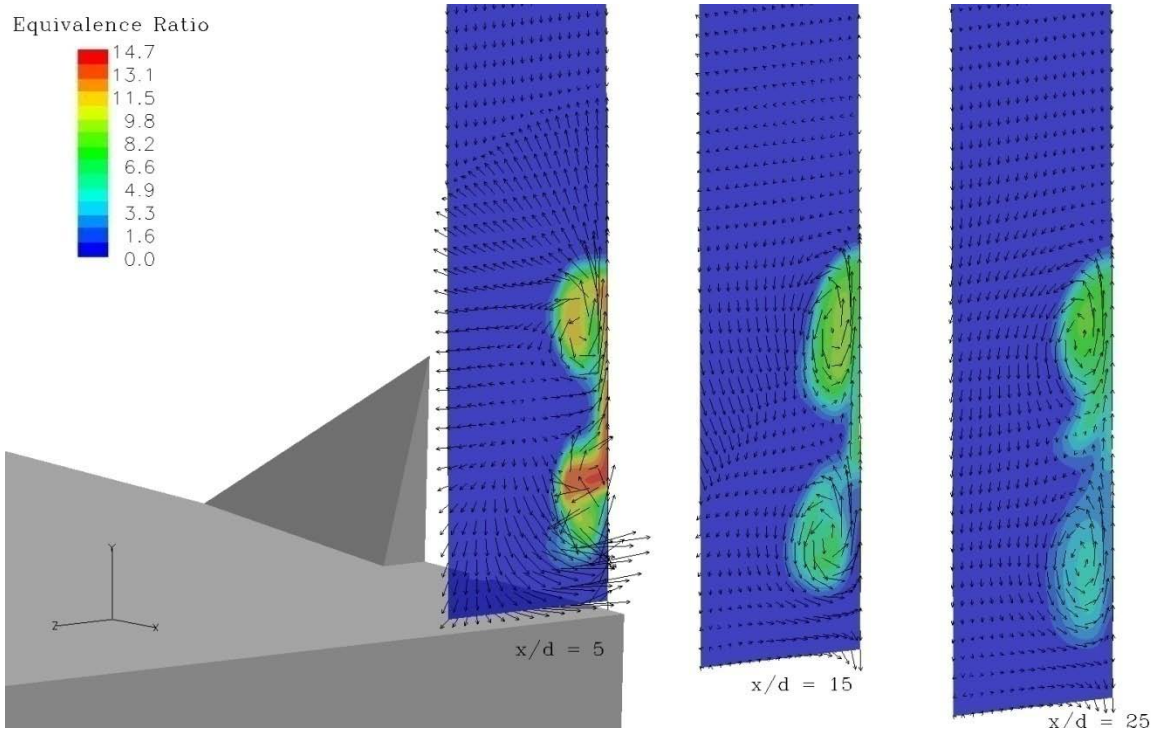

Figure 96. Equivalence ratio contour/velocity vector plot for the LWH-7x2x4-5h **p**ylon.

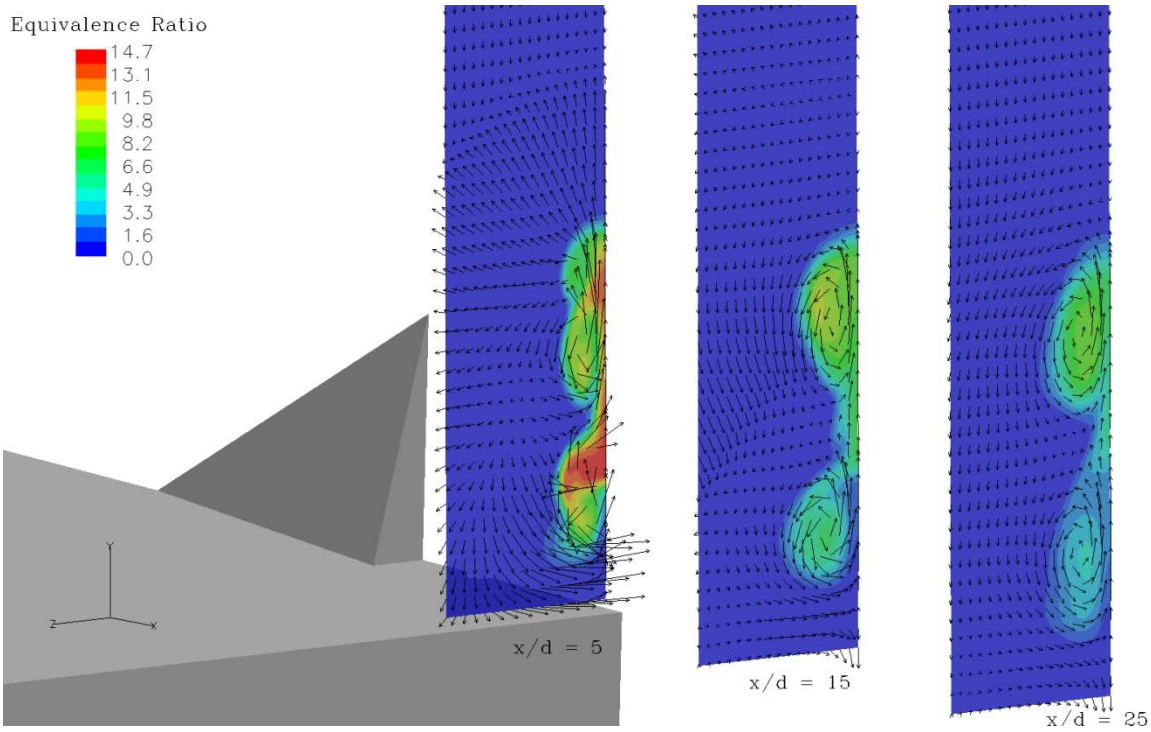

Figure 97 Equivalence ratio contour/velocity vector plot for the LWH-7x2x4-6h pylon.

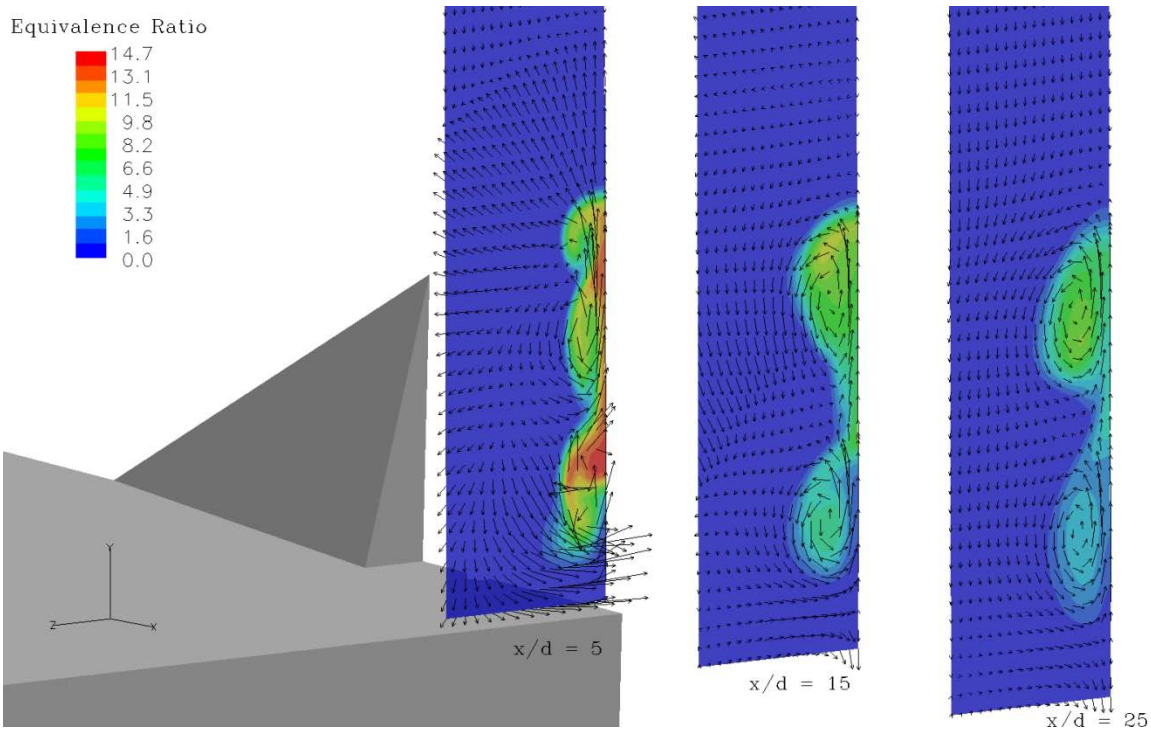

Figure 98. Equivalence ratio contour/velocity vector plot for the LWH-7x2x4-7h pylon.

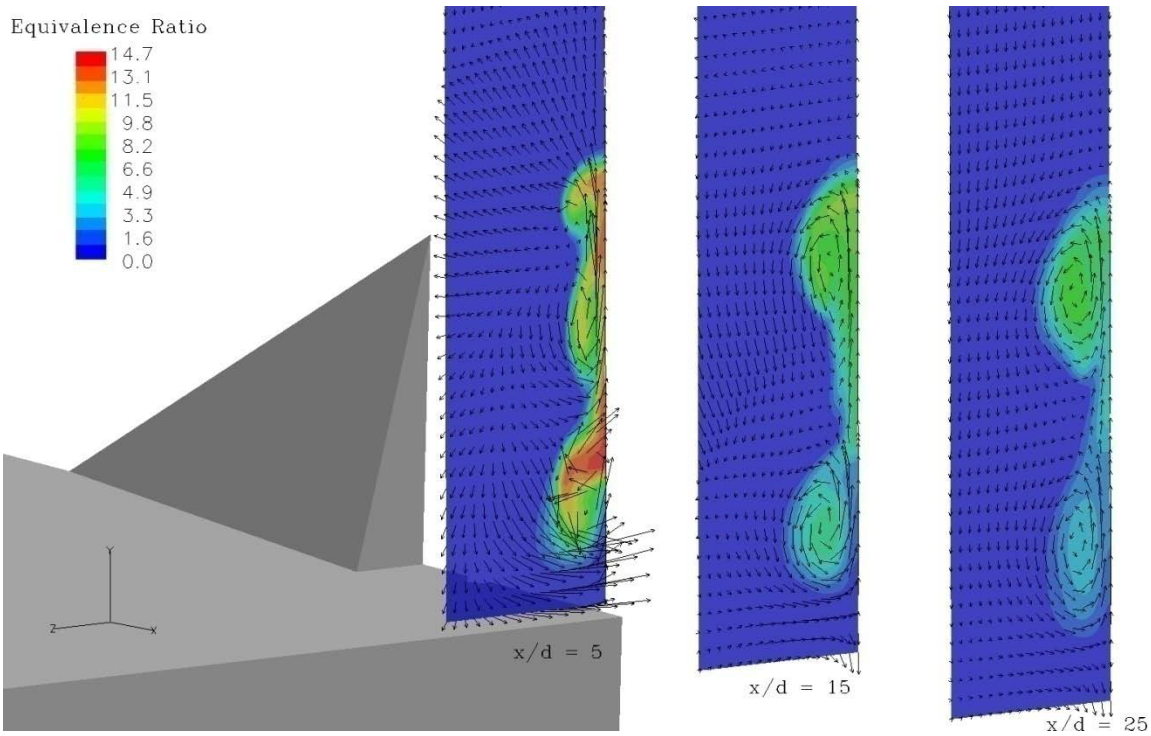

Figure 99. Equivalence ratio contour/velocity vector plot for the LWH-7x2x4-8h pylon

Figures 100 through 103 provide the secondary fuel air mixing metrics that were omitted from Chapter 4. Figure 100 provides the decay in maximum equivalence ratio for test matrix 3. Figure 101 depicts the flammable fuel plume percentage of the pylons depicted in test matrix 3. The variation in total fuel plume area as the LWH-7x2x4 pylon's absolute height is increased is seen in Figure 102. The mixing efficiency of the pylons in test matrix three can be seen below in Figure 103. The decay of maximum equivalence ratio, flammable fuel plume percentage, total fuel plume area, and mixing efficiency seen in the third test matrix are consistent to results seen in other test matrices.

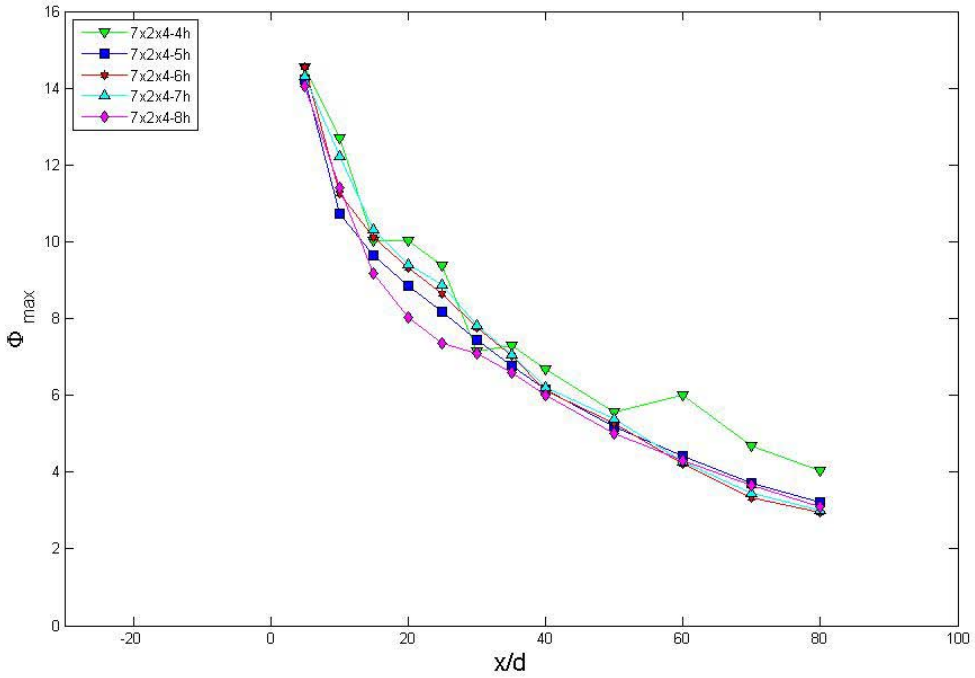

Figure 100. Decay of maximum equivalence ratio for the third test matrix, representing variation in absolute pylon height for the LWH-7x2x4 pylon.

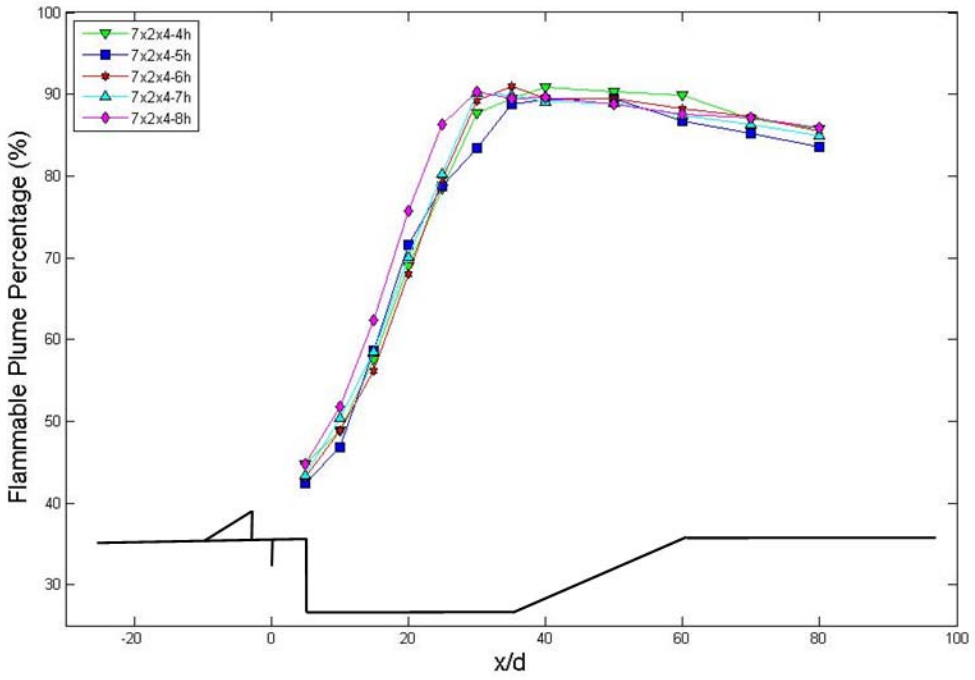

Figure 101. Flammable fuel plume percentage for the third test matrix, representing variation in absolute pylon height for the LWH-7x2x4 pylon.

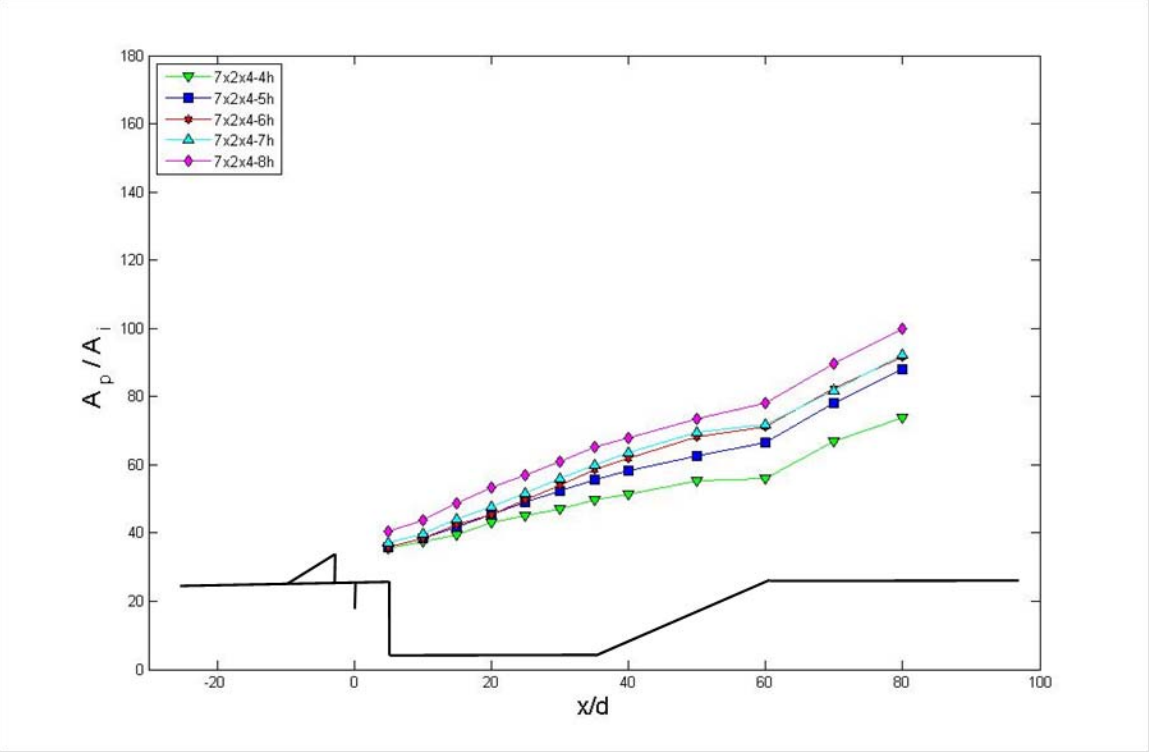

Figure 102. Total fuel plume area for the third test matrix, representing variation in absolute pylon height for the LWH-7x2x4 pylon.

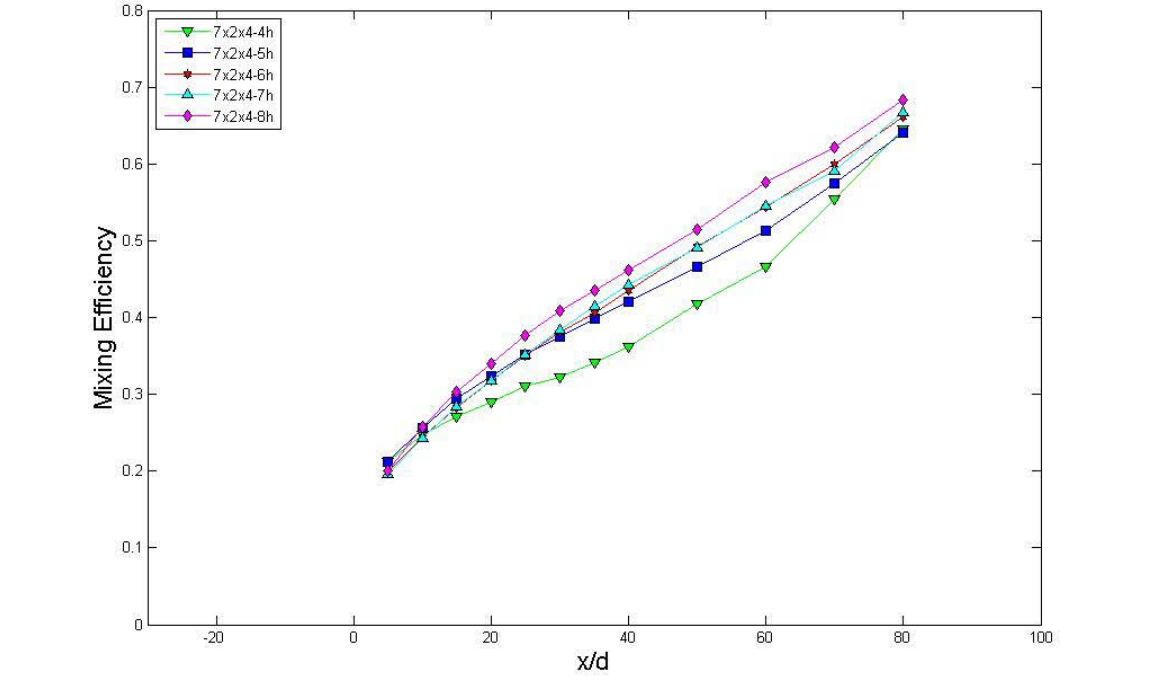

Figure 103. Mixing efficiency for the third test matrix, representing variation in absolute pylon height for the LWH-7x2x4 pylon.

Figures 104 through 109 provide the equivalence ratio contour/ velocity vector plots for pylons of differing leading edge wedge angles that were investigated in the fourth test matrix. Here it can be seen that the general fuel plume structure and strength and location of its flow field are not drastically impacted by the leading edge wedge angle.

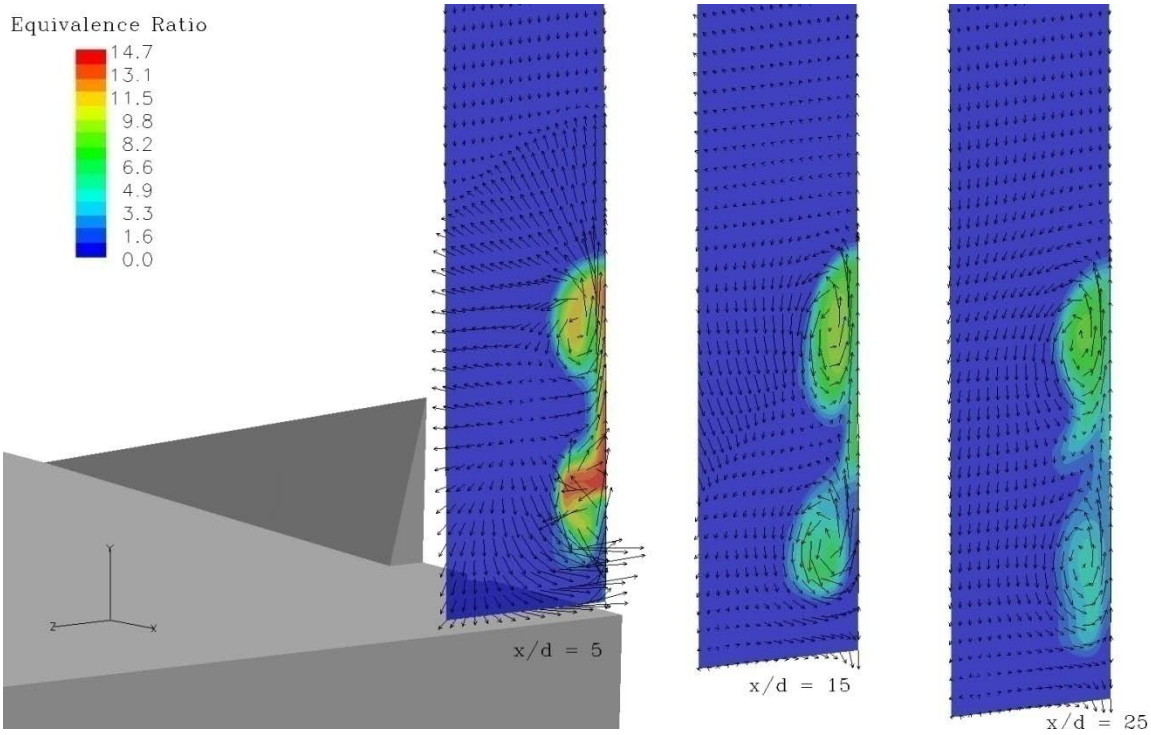

Figure 104. Equivalence ratio contour/velocity vector plot for the LWH-7x2x4-15˚pylon.

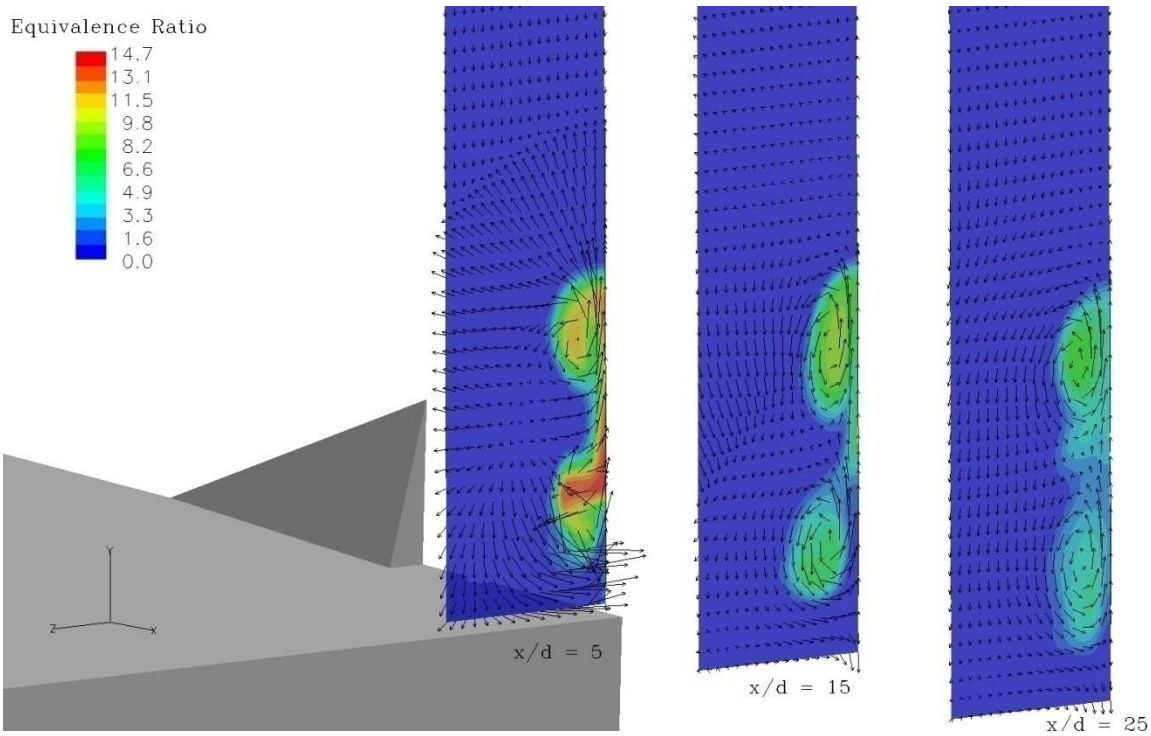

Figure 105. Equivalence ratio contour/velocity vector plot for the LWH-7x2x4-22˚pylon.

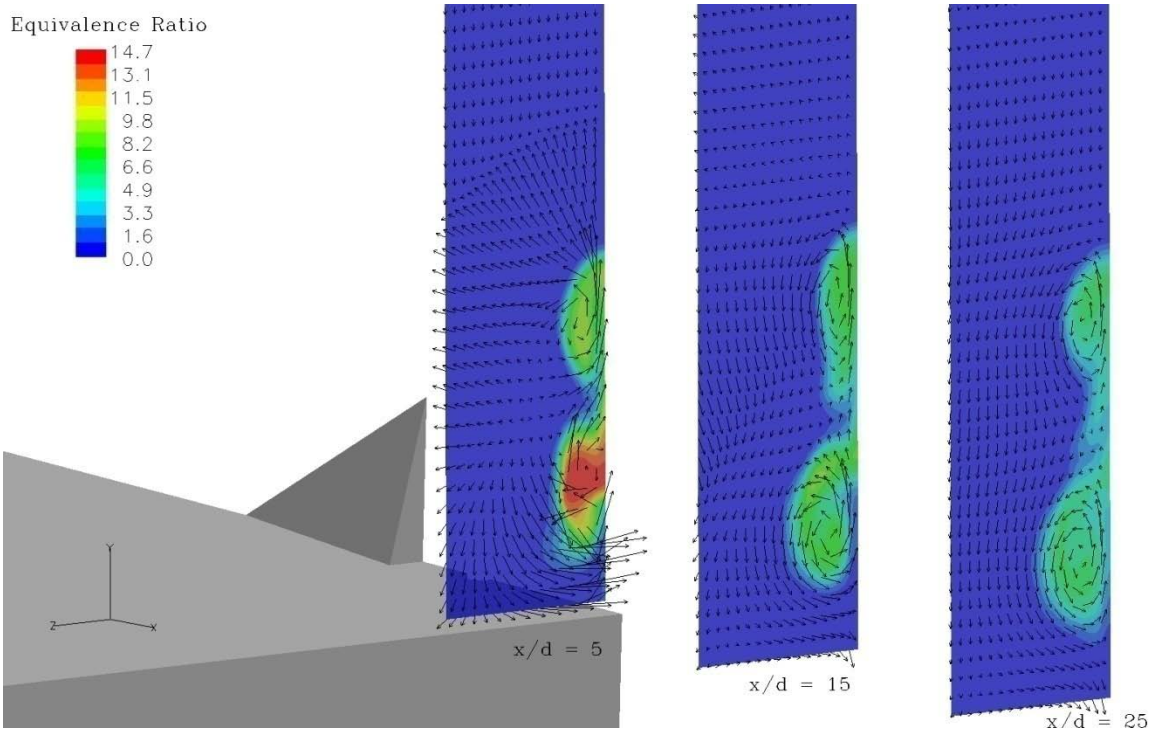

Figure 106. Equivalence ratio contour/velocity vector plot for the LWH-7x2x4-30˚pylon.

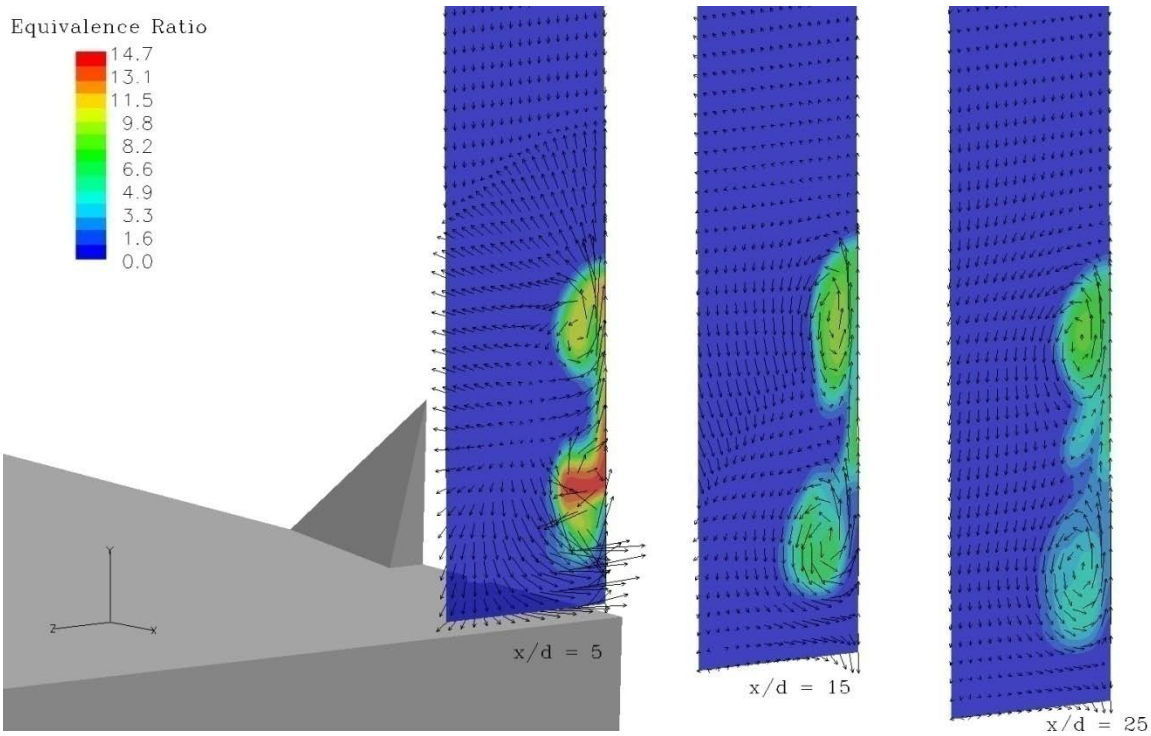

Figure 107. Equivalence ratio contour/velocity vector plot for the LWH-7x2x4-37˚pylon.

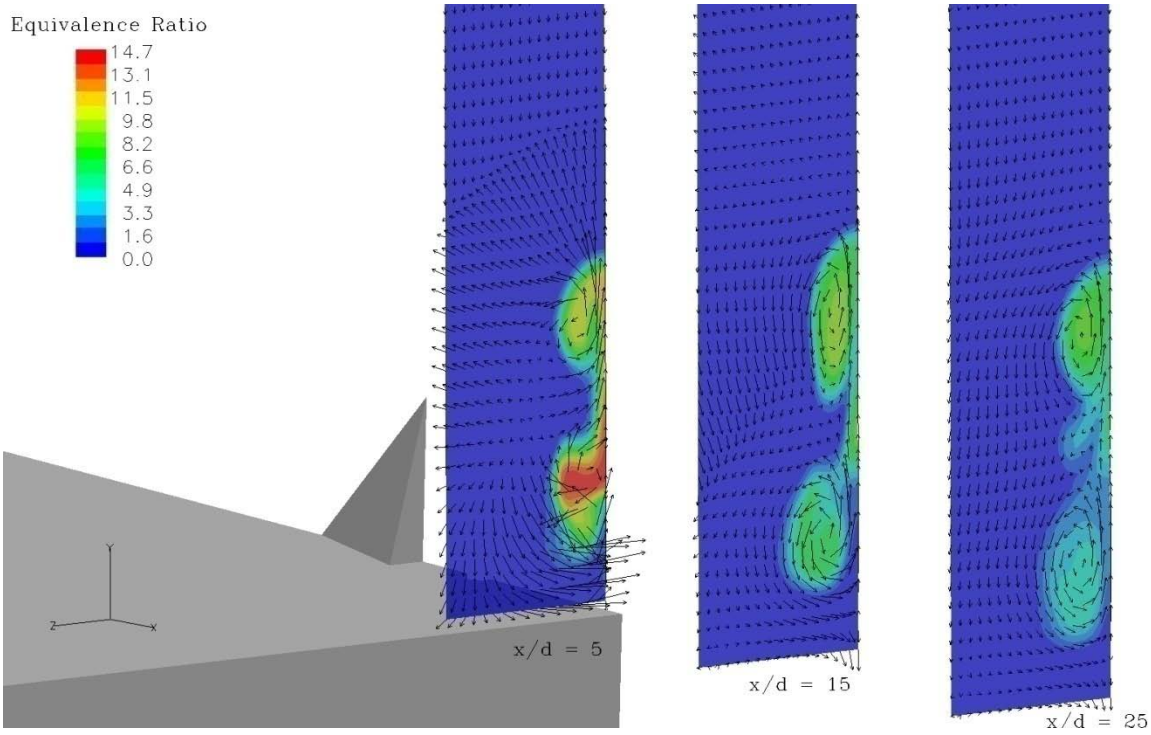

Figure 108. Equivalence ratio contour/velocity vector plot for the LWH-7x2x4-45˚pylon.

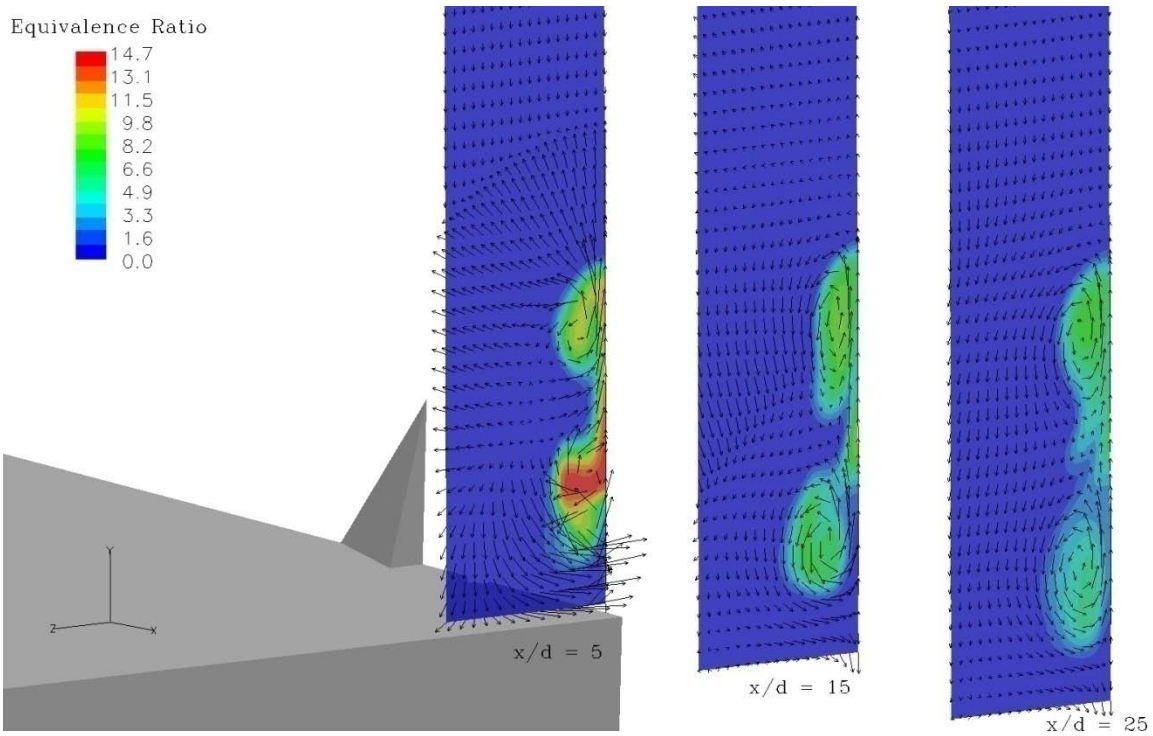

Figure 109. Equivalence ratio contour/velocity vector plot for the LWH-7x2x4-50˚pylon.

The secondary fuel-air mixing metrics associated with the fourth test matrix are provided below in Figures 110 through 112. Figure 110 illustrates the decay of maximum equivalence ratio as a function of downstream distance for pylons of various lengths. The flammable fuel plume percentage of the pylons in the fourth test matrix are seen in Figure 111. And lastly the difference in mixing efficiency of the six pylons tested in this final test matrix are shown in Figure 112. These three figures indicate that pylon length, or leading edge wedge angle, have minimal impact on the secondary fuel-air mixing metrics.

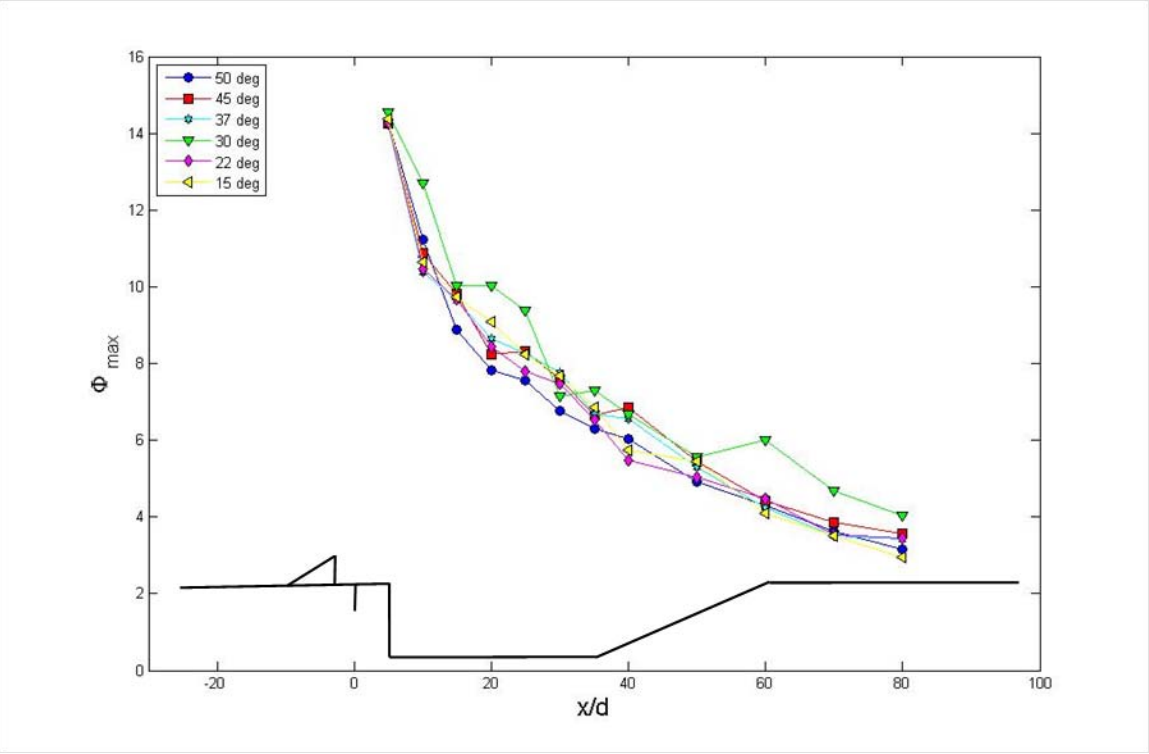

Figure 110. Decay of maximum equivalence ratio for the fourth test matrix, representing variation in leading edge wedge angle for the LWH-7x2x4 pylon.

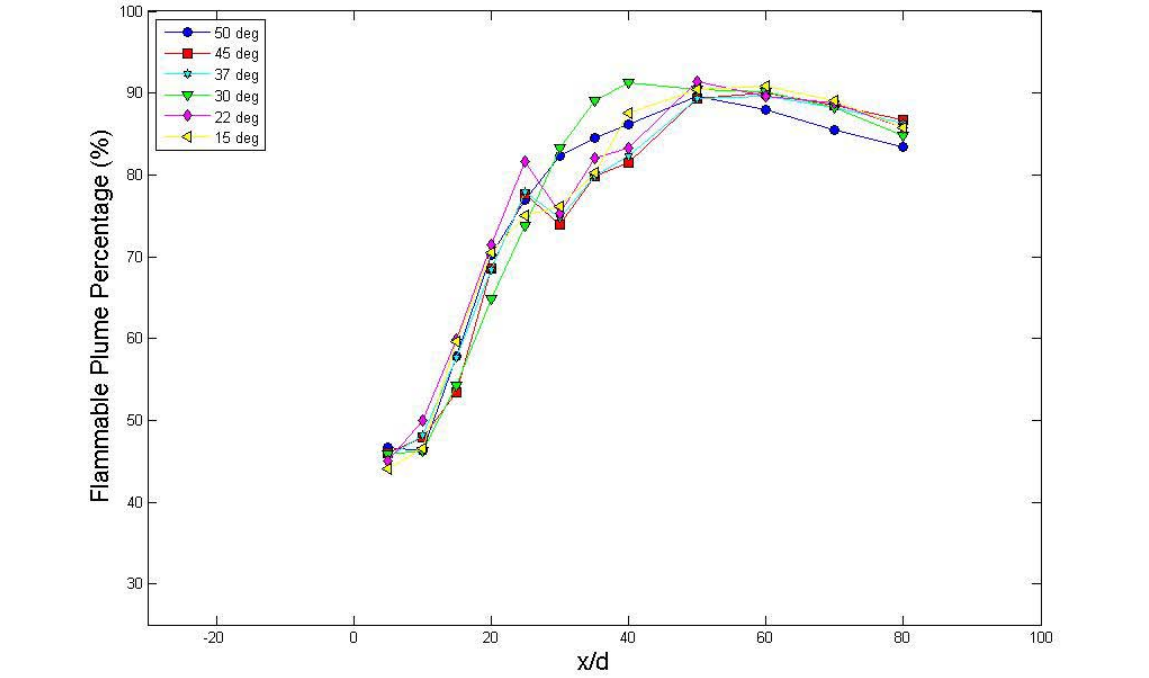

Figure 111. Flammable fuel plume percentage for the fourth test matrix, representing variation in leading edge wedge angle for the LWH-7x2x4 pylon.

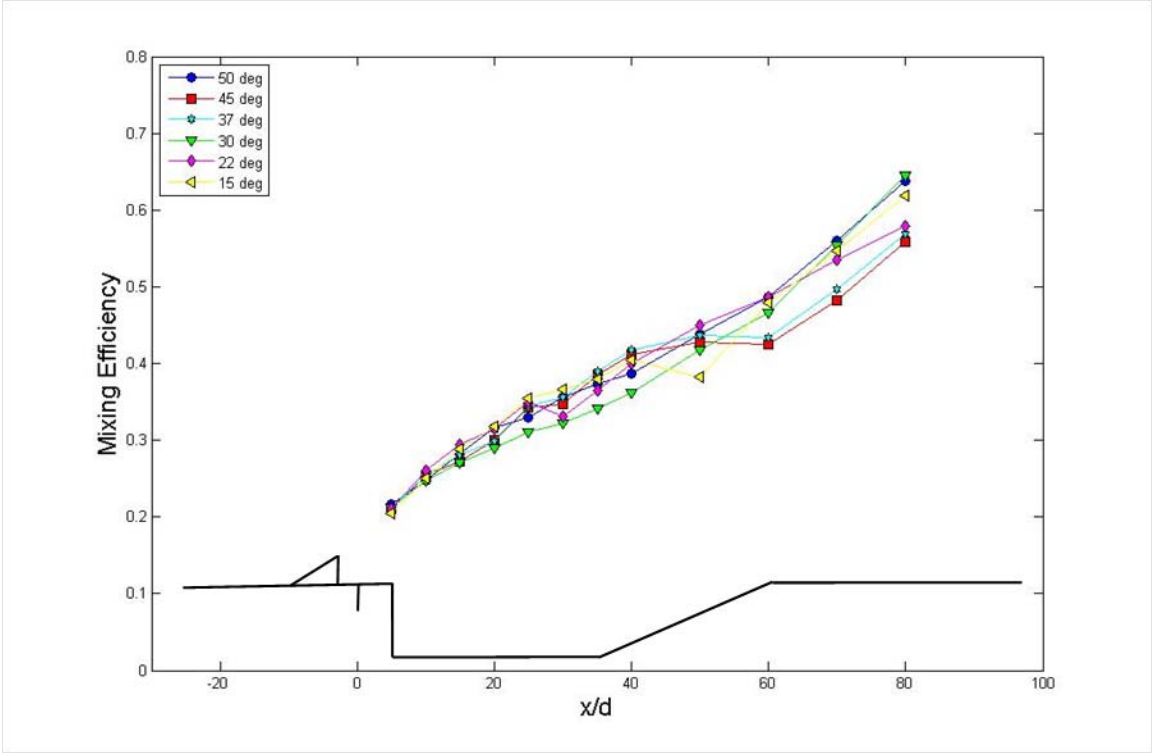

Figure 112. Mixing efficiency for the fourth test matrix, representing variation in leading edge wedge angle for the LWH-7x2x4 pylon.

Bibliography

[1] Haulbelt, Lane C. *Aerodynamic Loss and Mixing Over A Cavity Flame Holder Located Downstream of Pylon-Aided Fuel Injection*, MS thesis, AFIT /GAE/ENY/06-M13. Graduate School of Engineering and Management, Air Force Institute of Technology (AU), Wright Patterson AFB OH, March 2006

[2] Gouskov, O., Kopchenov, V., and Vinogradov, V., "Numerical Researches of Gaseous Fuel Pre-Injection in Hypersonic 3-D Inlet," AIAA Paper 2000-3599, July 2000

[3] Montes, D. R., King, P. I., Gruber, M. R., and Carter, C. D., "Mixing Effects of Pylon-Aided Fuel Injection Located Upstream of a Flameholding Cavity in Supersonic Flow," AIAA Paper 2005-3913, July 2005

[4] Livingston, T., Segal, C., Schindler, M., and Vinogradov, V., "Penetration and Spreading of Liquid Jets in an External-Internal Compression Inlet," AIAA Journal, Vol. 38, No. 6, June 2000, pp 989-994

[5] Balar, R., Gupta, K., and Yu, K., "Pylon-Aided Fuel Injection into Supersonic Flow," AIAA Paper 2007-834, January 2007.

[6] Heiser, William H. *Hypersonic Airbreathing Propulsion*. Washington D. C., AIAA Education Series, 1994.

[7] NASA Fact Sheet. http://www.nasa.gov/centers/langley/news/factsheets/X43A_2006_5.html. Accessed 8 February 2009.

[8] Powell, O., Edwards, J., Norris, R., and Numbers, K., "Development of Hydrocarbon-Fueled Scramjet Engines: The Hypersonic Technology (HyTech) Program," AIAA Journal of Propulsion and Power, Vol. 17, No. 6, December 2001, pp 1170-1176

[9] Curran, E.,T., and Murthy, S. N. B.,. *Scramjet Propulsion*, Reston VA. American Institute of Aeronautics and Astronautics, 2001.

[10] Quick, A., and King, P., "Upstream Mixing Cavity Coupled with a Downstream Flameholding Cavity Behavior in Supersonic Flow," AIAA Paper 2005-3709, July 2005.

[11] Schetz, J. A., Thomas, R. H., and Billings, F. S., "Mixing of Transverse Jets and Wall Jets in Supersonic Flow," Separated Flows and Jets, edited by V.V. Kozlov and A. V. Dovgal, Springer-Verlag, Berlin, 1991

[12] Newman, R. W., "Oxidation Resistant High Temperature Materials," Johns Hopkins APL Technical Digest, Vol. 14, No. 1, 1993, pp 24-28.

[13] Portz, R., and Segal, C., "Penetration of Gaseous Jets In Supersonic Flows," AIAA Paper 2006-1229, January 2006.

[14] VanLerberghe, W. M., Santiago, J. G., Dutton, J. C., and Lucht, R. P., "Mixing of a Sonic Transverse Jet Injected into a Supersonic Flow," AIAA Journal Vol. 38, No. 3, 2000, pp 470-479

[15] Orth, R.C., and Schetz, J. A., and Billings, F.S., "The Interaction and Penetration of Gaseous Jets in Supersonic Flow," NASA CR-1386, July 1969

[16] Walker, D.A., Cambel, R.L., and Shetz, J.A., "Turbulence Measurements for Slot Injection in Supersonic Flow," AIAA Paper 1988-123, January 1988

[17] Yu, K., Wilson, K.J., Smith, R.A., Schadow, K.C., "Experimental Investigations on Dual-Purpose Cavity in Supersonic Flows," AIAA Paper 1998-0723, January 1998

[18] Owens, M., Mullagiri, S., and Segal, C., "Effects of Fuel Preinjection on Mixing in Mach 1.6 Air Flow," AIAA Journal of Propulsion and Power Vol. 17, No. 3, 2001, pp 605-610.

[19] Naughton, J., Cattafesta, L., and Settles, G., "An Experimental Study of the Effect of Streamwise Vorticity on Supersonic Mixing Enhancements," AIAA Paper 89-2456, July 1989

[20] Fuller, R.P., Wu, P.-K., Nejad, A.S., and Schetz, J.A., "Fuel-vortex Interactions for Enhanced Mixing in Supersonic Flow," AIAA Paper 96-2661, July 1996

[21] Bonanos, Aristides, M., *Scramjet Operational Range Studies of an Integrated Aerodynamic-Ramp-Injector/ Plasma-Torch Igniter with Hydrogen and Hydrocarbon Fuels*, PhD dissertation, Virginia Polytechnic Institute and State University, Blacksburg, Va, August 2005.

[22] Cox, S.K., Fuller, R.P., Schetz, J.A., and Walters, R.W., "Vortical Interactions Generated by an Injector Array to Enhance Mixing in Supersonic Flow," AIAA Paper 94-0708, January 1994

[23] Vinogradov, V., and Shikhman, Y., "Review of Fuel Pre-Injection Studies in a High Speed Airflow," AIAA Paper 2006-1030, January 2006.

[24] Vinogradov, V., Prudnikov, A.G., "Injection of Liquid into the Strut Shadow at Supersonic Velocities," SAE Paper 931455, April 1993.

[25] National Air and Space Administration, *Vulcan Users Input Manual*, Version 6.0.1., 2007

[26] C.-J. John Tam, Sr. Research Scientist AFRL/RZAS/Taitech, Wright-Patterson AFB. Oh, Personal Interview, 10 October 2008.

[27] Kuo, Kenneth K., *Principles of Combustion*. New York, John Wiley and Sons, 1986.

[28] Anderson, G.Y., "An Examination of Injector/ Combustion Design Effects on Scramjet Performance," Proceedings of the 2nd International Symposium on Air Breathing Engines, 1974.

[29] Sunami, T., and Scheel, F., "Analysis of Mixing Enhancement Using Streamwise Vortices in a Supersonic Combustor by Application of Laser Diagnostics," AIAA Paper 2005-3304, May 2005.

[30] Doster, J., and King, P., "Numerical Simulations of Ethylene Injection from In-stream Fueling Pylons," AIAA Paper 2008-2518, May 2008.

[31] Glassman, Irvin, *Combustion*, 3rd Ed. New York, Academic Press, 1996.

[32] United Aircraft Research Laboratories, "Hydrocarbon-Fueled Scramjet," J910755-25, 1970.

[33] Wilcox, David C., *Turbulence Modeling for CFD*, 3rd Ed. La Canada, Ca., DCW Industries, Inc., 2006

[34] Seiner, J. M., Dash, S., M., Kenzakowski, D., C., "Historical Survey on Enhanced Mixing in Scramjet Engines," AIAA Journal of Propulsion and Power, Vol. 17, No. 6, December 2001, pp 1273-1286

REPORT DOCUMENTATION PAGE

Form Approved
OMB No.0704-0188

1. REPORT DATE *(DD-MM-YYYY)*	**2. REPORT TYPE**	**3. DATES COVERED** *(From – To)*
26-03-2009	Master's Thesis	Oct 2007 – Mar 2009

4. TITLE AND SUBTITLE

Critical Design Parameters For Pylon-Aided Gaseous Fuel Injection Upstream of A Flameholding Cavity.

5a. CONTRACT NUMBER

5b. GRANT NUMBER

5c. PROGRAM ELEMENT NUMBER

6. AUTHOR(S)

Pohlman, Mitchell R., Captain, USAF

5d. PROJECT NUMBER

5e. TASK NUMBER

5f. WORK UNIT NUMBER

7. PERFORMING ORGANIZATION NAMES(S) AND ADDRESS(S)
Air Force Institute of Technology
Graduate School of Engineering and Management (AFIT/EN)
2950 Hobson Street, Building 642
WPAFB OH 45433-7765

8. PERFORMING ORGANIZATION REPORT NUMBER

AFIT/GAE/ENY/09-M15

9. SPONSORING/MONITORING AGENCY NAME(S) AND ADDRESS(ES)
AFRL/RZAT (Propulsion Technology Branch)
Attn: Dr. Dean R. Eklund
2210 Eighth St. Dean.Eklund@WPAFB.AF.MIL
WPAFB, OH 45433 (937) 255-7294

10. SPONSOR/MONITOR'S ACRONYM(S)
AFRL/RZAT

11. SPONSOR/MONITOR'S REPORT NUMBER(S)

12. DISTRIBUTION/AVAILABILITY STATEMENT
APPROVED FOR PUBLIC RELEASE; DISTRIBUTION UNLIMITED.

13. SUPPLEMENTARY NOTES

14. ABSTRACT

The Air Force Institute of Technology and the AFRL are investigating means to increase the efficiency of fuel-air mixing into supersonic flow. Previous work has shown much promise in increasing the penetration and mixing of a fuel-air mixture into the freestream by injecting fuel behind small triangular pylons. Pylon-aided fuel injection has also shown to lift the fuel plume off the combustor floor; this floor-gap prevents the ignition of fuel seeded in the boundary layer. In this paper twenty-one pylons of varying widths, heights, and lengths were examined in four specific test matrices within a CFD environment. Pylons in test matrix 1 maintained a constant height and length while varying the pylon width. Test matrix 2 and 3 varied the absolute height of two different pylons from test matrix 1; scaling the pylons height and maintaining a constant leading edge wedge angle and width to height ratio. The final test matrix varied the length of pylons while keeping the height and width fixed. Pylons with a width less than 3-diameters featured a fuel plume dominated by two sets of counter-rotating vortices. These pylons provided large amounts of penetration and floor gap with minimal impact on flammable fuel plume area (A_f). The 4,5, and 6-diameter wide pylons resulted in flow structures dominated by one large set of vortices with minimal penetration and large A_f values. Variations in pylon length had no discernable impact on the mixing metrics. Aerodynamic loses were minimal for all pylon configurations and did not correlate to the absolute size of the pylons tested.

15. SUBJECT TERMS
Fuel injection, Scramjet propulsion, Pylon, Flame-holding cavity

16. SECURITY CLASSIFICATION OF:			**17. LIMITATION OF ABSTRACT**	**18. NUMBER OF PAGES**	**19a. NAME OF RESPONSIBLE PERSON**
1. REPORT	**2. ABSTRACT**	**c. THIS PAGE**			Dr. Robert B. Greendyke
U	**U**	**U**	**UU**	142	**19b. TELEPHONE NUMBER** *(Include area code)* (937) 255-3636, x4567 e-mail: robert.greendyke@afit.edu

Standard Form 298 (Rev. 8-98)
Prescribed by ANSI Std. Z39-18